Title
Electric Modulation of Conduction and Optical Characteristics in Ca-doped BiFeO3 Films for Memory Device Applications

Author
Kim, Sang-Yong

Publication Date
2011

Peer reviewed|Thesis/dissertation

Electric Modulation of Conduction and Optical Characteristics in Ca-doped $BiFeO_3$ Films for Memory Device Applications

by

Sang-Yong Kim

A dissertation submitted in partial satisfaction of the requirements for the degree of

Doctor of Philosophy

in

Engineering – Materials Science and Engineering

in the

Graduate Division

of the

University of California, Berkeley

Committee in charge:

Professor R. Ramesh, Chair
Professor Ronald Gronsky
Professor Tsu-Jae King Liu

Fall 2011

Electric Modulation of Conduction and Optical Characteristics in Ca-doped $BiFeO_3$ Films for Memory Device Applications

by Sang-Yong Kim

Abstract

Electric Modulation of Conduction and Optical Characteristics in Ca-doped $BiFeO_3$ Films for Memory Device Applications

by

Sang-Yong Kim

Doctor of Philosophy in Engineering – Materials Science and Engineering

University of California, Berkeley

Professor R. Ramesh, Chair

This dissertation details the synthesis and properties of Ca-doped $BiFeO_3$ thin films. The phase diagram was established as a function of the Ca doping concentration and temperature through structural analysis to study the effect of divalent-ion-calcium doping on $BiFeO_3$ films. A ferroelectric-paraelectric boundary exists around at 10% Ca doping ratio. For this doping concentration, the largest transition of conduction states was observed. The mechanisms for the observed effects are discussed on the basis of the interplay of ionic and electronic conduction through the redistribution of oxygen vacancies by application of electric fields. Application of electric fields enables to control and manipulate this electronic transition to the extent that a p-n junction can be created, erased and inverted in this material. Beside this conduction transition, the visible shading effect was observed with application of electric fields. Based on these reversible transitions of the electrical and optical characteristics of Ca-doped $BiFeO_3$, electrical and optical memory devices are proposed in this dissertation. The memory device built with a hetero-junction presented a nonvolatile conduction modulation with a rectified current behavior, which is essential for realizing random access memory devices. The switching mechanism is elucidated by junction property modification ascribed to the change of local oxygen vacancy concentration. In addition, the optical characteristics of Ca-doped $BiFeO_3$ films for potential electro-optic memory devices were measured and evaluated. Detailed discussion about the origin of the shading effect is given based on the change of a polar order parameter and an oxygen vacancy ordered state.

TABLE OF CONTENTS

List of Figures

List of Tables

Acknowledgements

I would like to thank all the people who have made it possible for me to finish my doctoral research. First of all, I want to deeply express my sincere gratitude toward my advisor, Professor R. Ramesh, for his support and guidance throughout the course of my research. I really appreciate him for giving me a chance to continue my academic career in this great school. His enthusiasm and open mind for a research and an academic cooperation are deeply impressive to me and I will keep these in my mind whatever I do and whomever I work with.

I would also like to give a special thanks to Chan-Ho Yang. Without him I would have been wandering through the woods in the dark. I cannot thank you enough for your help. I wish you and your family the best in the future.

I would like to extend a special thanks to Ying-Hao Chu, Jan Seidel, and Seung Yeol Yang-without their help and advice I wouldn't have made it this far. I would also like to give thanks to my present and former group members at Berkeley working under Professor Ramesh.

I would also extend my deepest thanks to my qualifying examination committee Professors Ronald Gronsky (Chair), Oscar Dubon, Junqiao Wu, and Sue-Jae King Liu and to Professors Ronald Gronsky and Sue-Jae King Liu for serving on my dissertation committee. Every comment and question was great help for deepening the understanding of my research.

Additionally, I would like specially acknowledge the friendship of Yongshik Park and his family. I have been lucky to have many wonderful times with him and his family and those memories made me forget homesickness and were great help to study abroad.

Finally, my wife and my family-for their devoted love and sacrifice I will be forever grateful.

Many thanks to Samsung Electronics for supporting the whole years of my studies.

Chapter 1 Introduction to New Memory Devices

This chapter gives an introduction to new memory devices emerging as the alternatives to current memory devices. Detailed discussions of device structures, operation mechanisms, and issues are presented. Especially, I focus on the Resistance-change Random Access Memory (RRAM) as the most promising candidate for a future memory device.

Chapter 1.1 Demands on New Memory Devices

Outstanding progress in information technology (IT) is attributed to the development of memory devices such as Static RAM (SRAM), Dynamic RAM (DRAM), and Flash memory devices. In spite of the advances of current memory devices, IT industry is continuously looking for new schemes of memory technologies. The main reason is that current technologies are continuously faced with difficult issues of scaling [1]. Key challenges to memory scaling originate from lithography and device characteristic [2, 3].

Demands on new memory devices were also born from this idea that current multi-chip solution can be replaced by single-chip solution with the new memory devices, which have the all functionality of the current memory devices. The current individual memory device does not satisfy all IT industry requirements such as high density, high speed and non-volatality. Each device has its own characteristics and functionalities; SRAM is the fastest but the lowest density device, DRAM has moderate speed and density, and Flash memory is the lowest device in read/write but it is nonvolatile and the highest density device (Figure 1.1a). Therefore, two or more memory devices are combined together to satisfy those requirements and to fabricate final products (Figure 1.1b). However, if a new memory device satisfies all these requirements, multiple chips can be replaced with a single chip. This single-chip solution has a lot of advantages such as no booting delay, no data loss and long run usage. These properties are getting to be more important as the IT quickly shifts to the mobile environment.

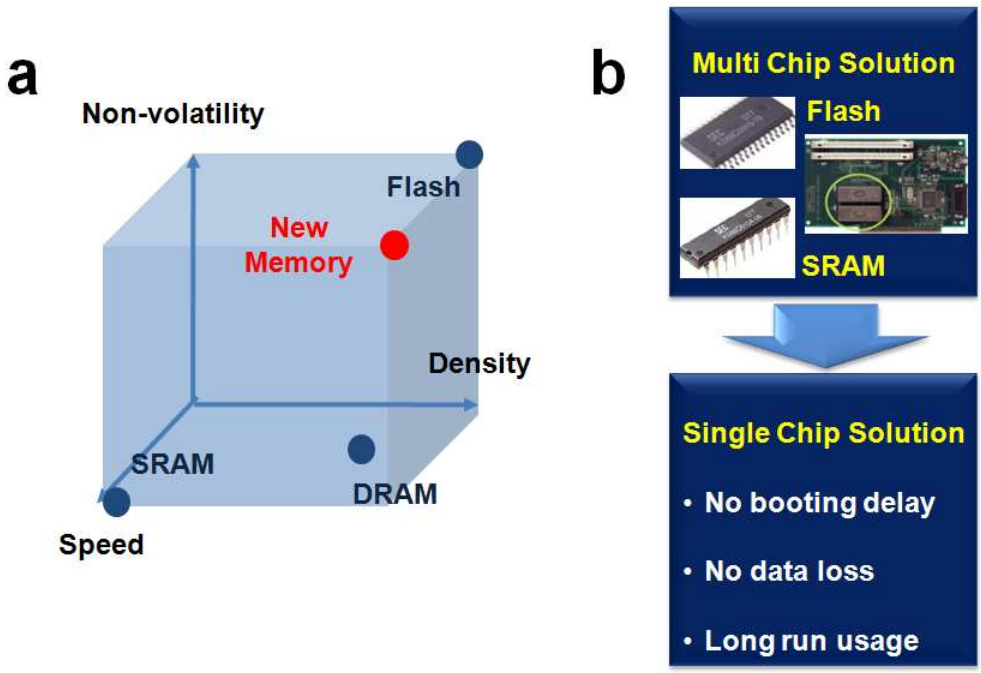

Figure 1.1: a The characteristics of current memory devices. **b** Example of multi chip solution and the advantages of single chip solution.

Chapter 1.2 Emerging New Memory Devices and Issues

Among many new types of memories, Ferroelectric RAM (FRAM), Phase-change RAM (PRAM), and Magnetic RAM appear to be promising candidates for commercialization. Basic cell structures and operation mechanisms are summarized in Table 1.1. However, despite these emerging new memory devices have almost ideal memory characteristics in conceptually and are promising to solve the problems of conventional memory devices, the current technical status is still far from the industry requirements. One of the critical limitations of these devices is scalability.

For example, the ideal cell size of MRAM is 9~12 f^2 (f indicates the minimum half pitch size of a device. For a detail of cell size, see Appendix A) which is much larger than that of current DRAMs (6 f^2). The memory cell structure of MRAM has additional metal lines called digit-line for magnetically writing the memory cells; thus the memory cell inherently has a complicate and large cell structure [4, 5]. In the case of FRAM, it has larger ideal cell size than that of Flash memory but is comparable with DRAM because its cell structure is basically same as DRAM. So for further scaling down the cell area, it is needed to follow the similar way which DRAM capacitor already experienced, i.e. three dimensional capacitor structure is required [6, 7]. A cylinder-like capacitor structure can eventually lead FRAM to the cell size of 6 f^2. For this purpose, it is essential to control nano-scaled thickness and to grow excellent conformal films on the inside wall of a high aspect-ratio capacitor but these are very difficult challenges without any degradation of ferroelectric properties.

Device		Operational Mechanism	Cell Structure	Ideal Cell Size (F^2)
FeRAM	Ferroelectric RAM	Polarization	1Tr1Cap	6~8
MRAM	Magnetic RAM	MR-change	1Tr1MTJ	9~12
PRAM	Phase RAM	Phase change	1Tr1GST	6~8
RRAM	Resistance RAM	Resistance change	1Mem	4

Table 1.1: Summary of new memory devices. Operational mechanism, basic cell structures, and ideal cell sizes are listed. (Tr, Cap, MTJ, and Mem indicate transistor, capacitor, magnetic tunnel junction, and memristor, respectively). GST represents the phase-change module in PRAM consisting of GeSbTe alloys).

PRAM has no physical scaling limitation because the cell states of this device are read through resistance differences between the cell of '1' and '0' unlike DRAM devices. DRAM is a charge-storage-type memory device; so the storage area of each cell is a major factor to determine performances of the device. In addition, unlike the MRAM, PRAM does not need any additional metal lines because it is controlled by an electric field [8]. However, the most important technical barrier to the PRAM scaling comes from large current consumption during reset process of GST in order to change the crystalline state into the amorphous state. Large reset current requires a large size of cell transistor, which makes PRAM cell size larger than ideal size of $6 f^2 \sim 8 f^2$ and makes it hard to achieve high density PRAM [2].

From this point of view, another type of a new memory device, a Resistance-Change RAM (RRAM) might be the most promising alternative because of its simple cell structure ($4 f^2$ as seen in Table 1.1). RRAMs have at least two resistance states, a low resistance (ON) and a high resistance state (OFF), which are reversibly switched by electric pulses. Such a circuit element showing a resistive switching behavior was named memristor (memory resistor) as the fourth passive electric circuit element by Leon Chua [9]. He reasoned from symmetry arguments that there should be a fourth fundamental element. The details of a RRAM are introduced in the following chapter.

Chapter 1.3 Introduction to Resistance-Change RAM (RRAM)

A RRAM memory cell is basically a capacitor-like structure, which is composed of insulating or semiconducting oxides that exhibits reversible resistive switching and two layers of electrodes. The individual cells are addressed in a cross-point array. The memory layer is sandwiched between two layers of electrodes running in perpendicular directions, above and below (Figure 1.2).

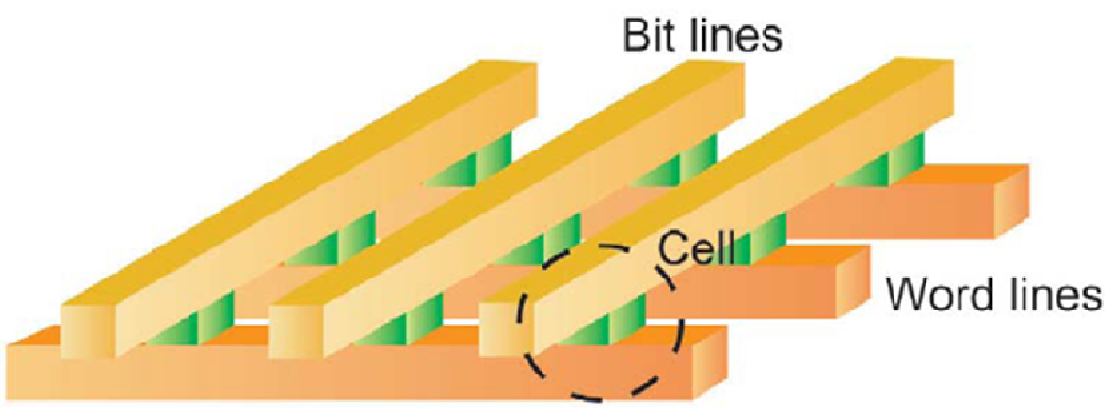

Figure 1.2: Basic memory cell structure of RRAM. Unit cells for resistance-change are represented in green boxes, which are sandwiched by top and bottom electrodes (bit lines and word lines, respectively) [10].

RRAM holds the spotlight due to such a simple cross-point cell structure besides the promising characteristics such as non-volatility, fast switching speed, low power consumption [10-12]. The basic operation is to set at least two different states by applying an appropriate voltage and then read back by measuring current at some lower voltage than set-voltages.

Chapter 1.3.1 Basic Characteristics of RRAM

Based on *I* (current)-*V* (voltage) characteristics, the resistive switching behavior can be classified into two types: a unipolar (non-polar) and a bipolar switching. In a unipolar resistive switching, devices show ON/OFF transitions at the same polarity, which means the switching direction depends on the amplitude of the applied voltage but not the polarity. As shown in Figure 1.3a, the current suddenly jumps up to the highly conductive state at some threshold voltage. Usually, the current is limited by setting an appropriate compliance current to avoid any dielectric breakdown. The ON-state returns to the OFF-state by flowing high current through the cell at the same polarity. On the other hand, bipolar devices show polarity dependence. The switching from OFF-state to ON-state at some threshold voltage and the ON-state only can return to the OFF-state by applying opposite voltage (Figure 1.3b).

Chapter 1.3.2 Characteristics of Materials for RRAM (Roles of Oxygen Vacancies)

Most of RRAM systems use transition metal oxides as the resistive switching layer. The resistive switching phenomenon has been observed in a wide variety of transition metal oxides, such as CuO, TiO, NiO, ZnO, $SrTiO_3$, PCMO, etc [13-19]. These oxides generally have been called as wide bandgap semiconductors mainly for two reasons. First, their bandgaps are larger than those of conventional semiconductors (Si ~1eV and Ge ~0.67eV) (Figure 1.4a). Second, the electrical characteristics of these oxides are tunable through impurity doping as conventional semiconductors [20]. The tunable electrical characteristics of these oxides are critical to elucidate

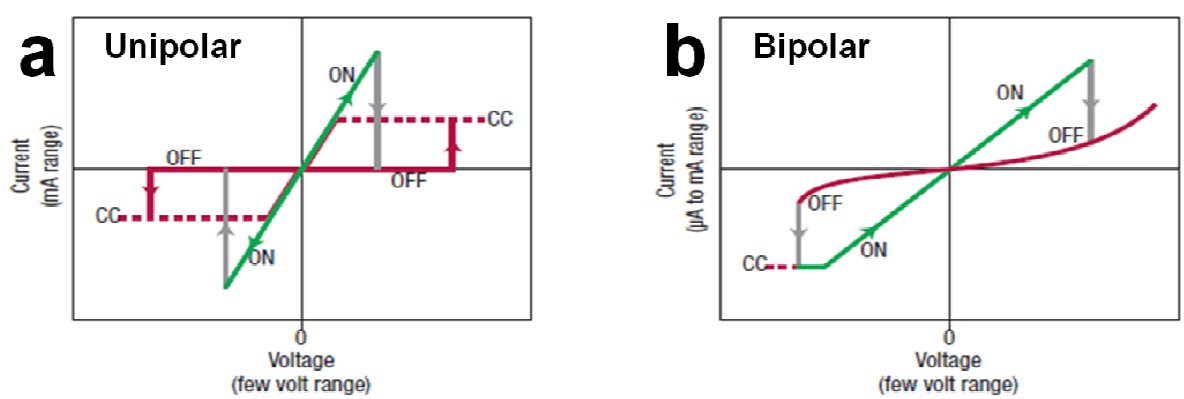

Figure 1.3: a *I-V* characteristics of unipolar resistance switching devices. The transition between ON and OFF-state occurs at a same polarity. **b** *I-V* characteristics of bipolar resistive switching devices. The ON/OFF transitions are achieved by applying opposite voltages.

the resistive switching behavior.

The most popular way to control the electric properties of these oxides is changing the oxygen stoichiometry, i.e., the oxygen vacancy concentration. It is well known that oxygen vacancies are inherent defects in oxides and the electrical characteristics of oxides are very sensitive to the oxygen vacancy concentration [20, 21]. For example, Figure 1.4b shows how the conduction mode of a perovskite oxide electrolyte in a solid oxide fuel cell at elevated temperature changes from n-type to ionic and p-type conduction with respect to the oxygen partial pressure in the atmosphere. Oxygen vacancies act as donor impurities in oxides; thus the deviation from the stoichiometry can result in n-type (electron) conduction for oxygen vacancy rich phase and p-type (hole) conduction for oxygen vacancy deficient phase.

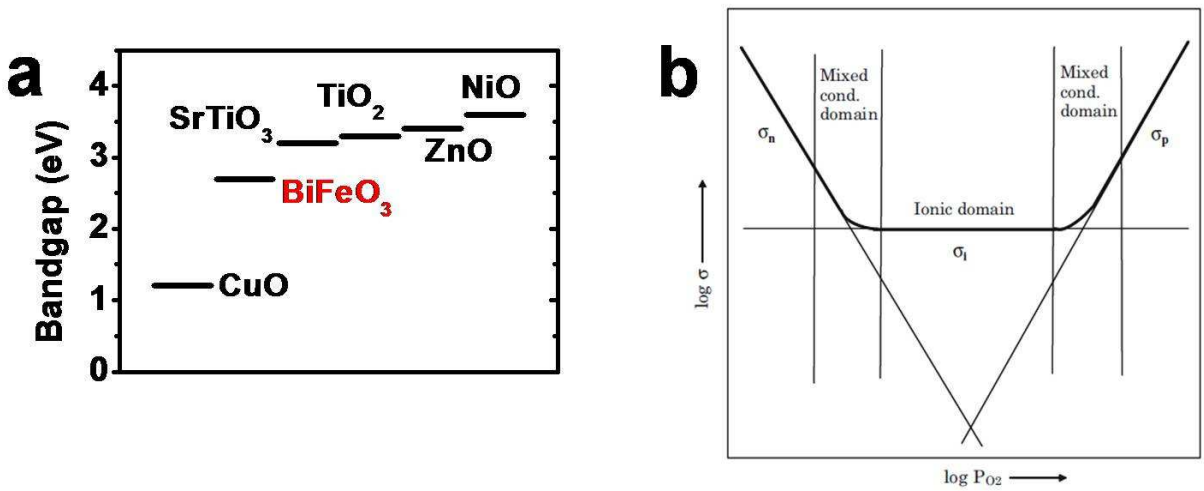

Figure 1.4: a Bandgaps of various transition metal oxides. **b** Conduction mode of perovskite oxide electrolyte in solid oxide fuel cell at elevated temperature. It changes from n-type (electron) and ionic and p-type (hole) conduction with respect to the oxygen partial pressure in the atmosphere [21].

Chapter 1.3.3 Resistive Switching Mechanisms for RRAM

One of the major issues to develop RRAM is that there is no design guide based on a driving mechanism of resistive switching. Several possible driving mechanisms have been proposed, e.g. the conductive filament generation and rupture [22-24], modulation of order parameters (ferroelectricity [25], ferromagnetism [26]), Schottky barrier modulation [27], and space charge trap and detrap in thin films [28, 29].

Basically, these proposed mechanisms can be categorized into the bulk-limited and interface-limited conduction modulations. Bulk-limited resistive switching mechanisms originate from the formation and rupture of conductive filaments in an insulating film (Figure 1.5). These types of devices need ‘electroforming’ (simply forming) process before showing ON/OFF switching. In the forming process, it is believed that the filamentary conducting paths form as a

soft breakdown by a high voltage stress (middle figure in Figure 1.5). Rupture of the filaments (reset process) and reformation of the filaments (set process) are reflected in high and low resistance, respectively. Electrochemical reactions near the interface between the metal electrode and the oxide might be the reason of the open and close of conductive faucets [23]. Direct and clear visualization of the conducting filaments has not been reported but recent studies involving high resolution transmission electron microscopy [30] and conductive atomic force microscopy (c-AFM) [31] suggest that the creation and termination of the filamentary conducting paths.

The other type of switching mechanism is interface-limited conduction modulation, in which the resistive switching takes place at the interface between different oxides or between the metal electrode and the oxide. The contact resistance (or junction resistance) is altered by tuning the junction barrier height and the potential profile in the depletion layer with an applied electric field. For the contact between the metal electrode and the oxide, the contact resistance comes from a Schottky barrier. The contact resistance is determined by the barrier height but the potential profile in the depletion layer determined by the doping concentration is also critical factor. The narrow depletion layer enables the tunneling of the charged carriers through the barrier, which results in forming an Ohmic contact with low contact resistance. As mentioned in chapter 1.3.2, oxygen vacancies act as a donor and a migration of oxygen vacancies in the vicinity of the interface is considered to be the driving mechanism for the change in the depletion width.

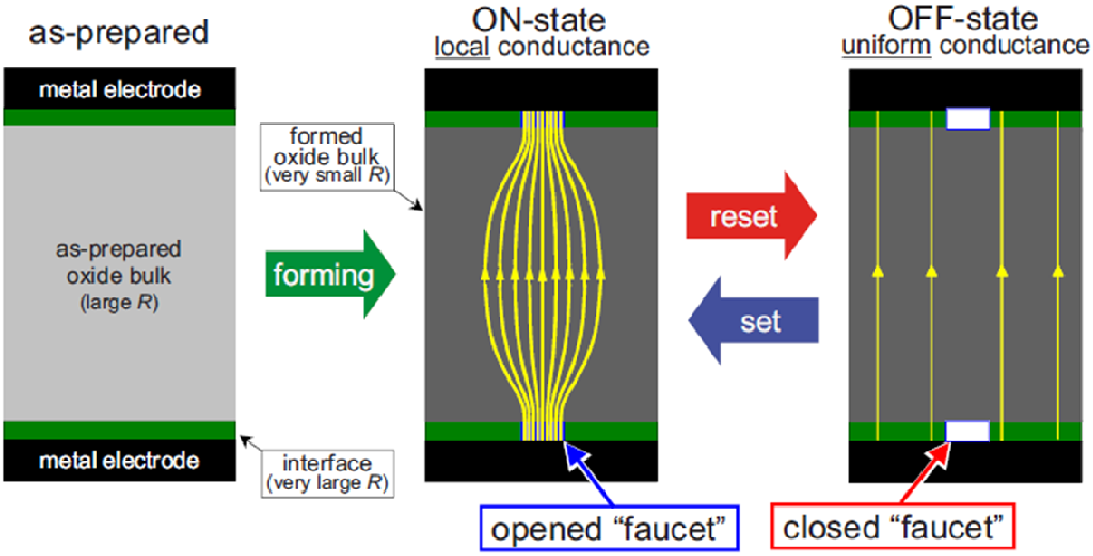

Figure 1.5: Schematic pictures of the forming, set, and reset for a conductive filament model. By applying a large electric field to the initial state, the whole bulk region of the oxide becomes much more conducting with forming conductive filaments (middle picture). Rupture of the filaments (reset process, right-end picture) and reformation of the filaments (set process, middle picture) are reflected in high and low resistance, respectively [23].

Despite the resistive switching mechanisms are diverse, all of these mechanisms are partially or mostly related to the movement and sequential redistribution of oxygen vacancies. When oxygen vacancies act as donor impurities, the increase of local oxygen vacancy concentration by external perturbations (e.g. electric fields) can make this local area highly conductive n-type semiconductor. In most cases, the changes of the electric properties in local area by oxygen vacancy redistribution are responsible for the resistive switching characteristics.

These two different resistive switching types can be verified experimentally by measuring the area dependence of the cell resistance. As shown in Figure 1.6, the resistance of Nb-doped $SrTiO_3$ is inversely proportional to the cell area, whereas that of an insulating NiO is much less dependent on the cell area [23]. These results represent that resistive switching in the former takes place over the whole area of the cell which is defined by the electrode size, whereas NiO can be considered to be controlled by local conduction, i.e. filament type conduction.

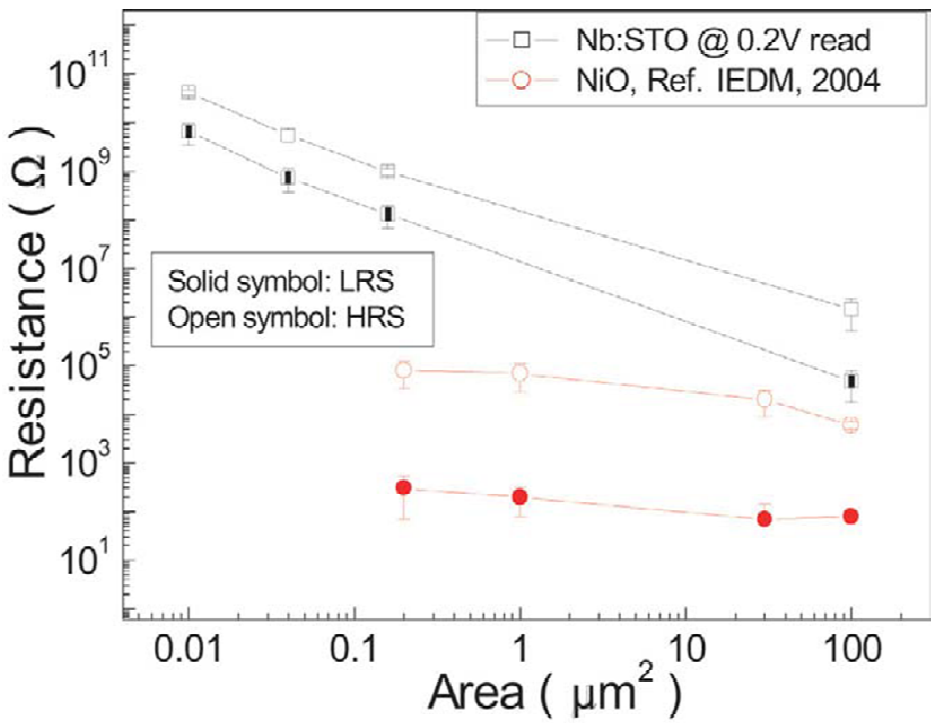

Figure 1.6: Area dependence of ON and OFF-state for Nb doped STO and NiO RRAM systems. The resistance of Nb doped STO cells shows linearly increases with increasing the size of electrodes, suggesting that the resistive switching occurs uniformly over the entire area of the electrode and oxide interface. On the other hand, the resistance of NiO memory cells does not show electrode size dependence, suggesting that resistive switching is a local and bulk-limited phenomenon [23].

1.4 Prospects of RRAM Devices

RRAMs exhibit extremely non-linear *I-V* behaviors and unconventional reversible resistive transient effects, which expect RRAMs can potentially supplement or replace current memory devices in certain applications. However, a deep understanding of the driving mechanism for resistive switching is imperative in order to optimize RRAM device characteristics and develop guidelines for scaling, reliability, and reproducibility. Further research of chemical, electronic, and crystallographic and careful device optimization through device modeling and circuit simulation will likely open a new era of RRAM based memory devices.

1.5 Organization of Dissertation

The remainder of this dissertation consists of three main chapters, a short chapter of conclusion and suggestions for future work (**Chapter 5**), three **Appendices**, and **References**.

Chapter 2 focuses on the growth and structural and electrical characterization of a Ca-doped $BiFeO_3$ thin film. In this chapter I discuss the quasi-nonvolatile and reversible modulation of electric conduction, accompanying the modulation of the ferroelectric state of Ca-doped $BiFeO_3$ (BCFO) films. Detailed X-ray diffraction and micro- and macro-electrical measurements will be shown to investigate and establish the phase diagram, ferroelectric state and conduction state of BCFO.

In **Chapter 3** I introduce the non-volatile memory device based on the characteristics of BCFO discussed in Chapter 2. I will show a reversible resistance transition in BCFO/ La doped $SrTiO_3$ (SLTO) hetero-junction with a rectified current flow behavior. Design concept, detailed electric characteristics, and the switching mechanism of the BCFO/SLTO hetero-junction device are discussed.

Chapter 4 is dedicated to introducing another memory device application of BCFO. In this chapter, the unique optical characteristics of a BCFO for a potential optical memory device application are introduced. The visual shade changes in BCFO with applied electric fields can generate two different bit information states which can be read by optical measurements. Using a combination of optical characterization techniques in conjunction with high resolution transmission electron microscopy and first-principles theory, I will show that BCFO thin films exhibit a prominent shade change effect arising from an intrinsic mechanism due to the melting of oxygen vacancy ordering and the associated redistribution of carriers.

Chapter 5 serves as summary chapter recapping the findings presented in each of the preceding chapters of the dissertation and ends with a brief look at suggested future work.

Appendix A covers the determination of the cell size of memory devices. **Appendix B** introduces pulsed laser deposition (PLD) technique used for the film growth throughout this dissertation. Finally, **Appendix C** focuses on scanning probe microscopy, especially piezoresponse force microscopy (PFM), and how this can be used to probe ferroelectric state in materials.

Chapter 2 Electrical Modulation of Ca-Doped $BiFeO_3$

Transition metal oxides such as TiO_2, NiO and $BiFeO_3$ have been of great importance since they have interesting electrical and optical characteristics and these properties can be potentially utilized for optoelectronics and memory device applications [32]. In this chapter, the quasi-nonvolatile and reversible modulation of electric conduction, accompanying the modulation of the ferroelectric state, are addressed in Ca-doped $BiFeO_3$ (BCFO) films, using an electric field as the control parameter. The mechanism of resistive switching in BCFO is discussed based on the charge balance and the local charge unbalance of oxygen vacancy donor impurities and the calcium acceptors. Detailed X-ray diffraction and micro- and macro-electrical measurements were used to investigate and establish the phase diagram, ferroelectric state and conduction state of BCFO.

Chapter 2.1 Introduction to $BiFeO_3$ (BFO)

In complex oxides, many interesting phenomena such as high temperature superconductivity, colossal magnetoresistance arise out of a doping-driven competition between energetically similar ground states [33-35]. As aforementioned in Chapter 1, proper doing can also drastically change the electronic or ionic conductivity of oxides by generating extra mobile charge carriers or oxygen vacancies. For this purpose, calcium is selected as a dopant because it's well known that the calcium doping creates oxygen vacancies in BFO [36]. In addition, Ca doping allow to control the number of oxygen vacancies in BFO and to ignore the influence of intrinsic defects because these are very small amount compared to the number of oxygen vacancies naturally created by calcium doping.

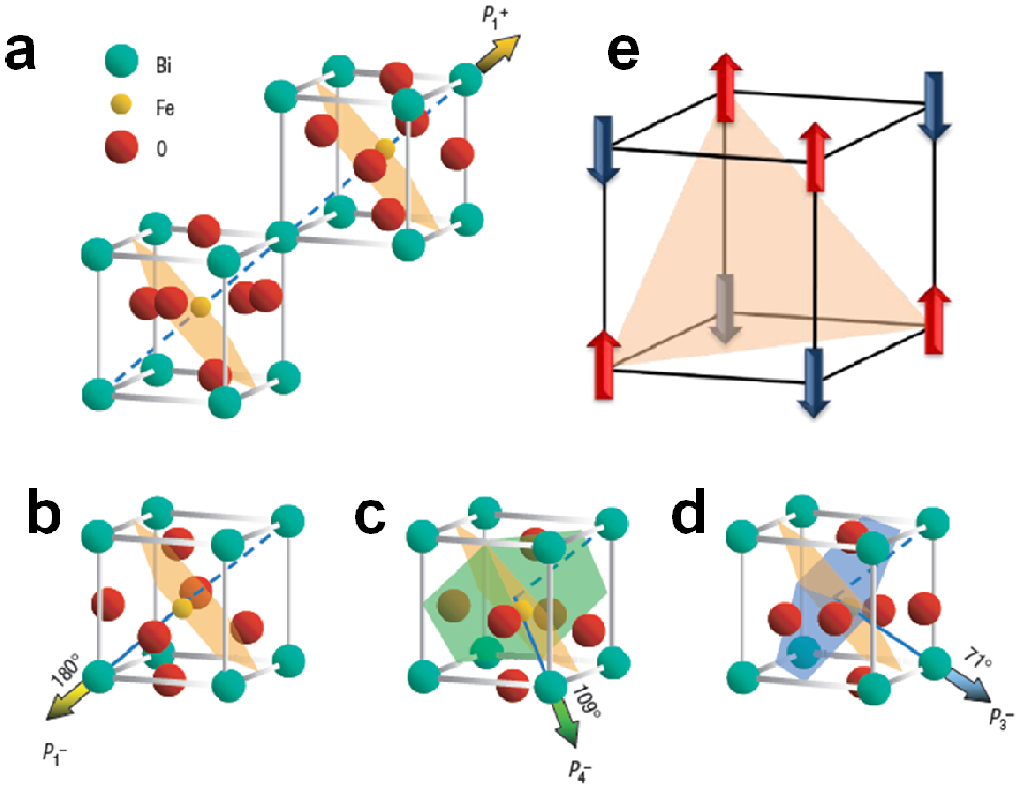

Figure 2.1: Schematic diagram of $BiFeO_3$ crystal structure and the ferroelectric polarization (bold arrows) and antiferromagnetic plane (shaded planes). **a** Polarization with an up out-of-plane component before electric poling. **b**, **c**, **d** 180°, 109° and 71° polarization switching mechanism with the out-of-plane component switched down by an external electric field, respectively. **e** The magnetic structure of $BiFeO_3$; G-type antiferromagnetic ordering.

The parent compound $BiFeO_3$ is one of the most widely studied multiferroic materials in which ferroelectricity and antiferromagnetism coexist at room temperature [37]. Its ferroelectric transition temperature (T_C) is 1103 K [38] and antiferromagnetic Néel temperature (T_N) is 640 K [39]. The bulk crystalline structure can be described as rhombohedral symmetry (space group *R3c*) [40] but in thin films, strain induced by coherent growth lowers the symmetry to monoclinic [37]. The ferroelectric state is realized by a large displacement of the Bi-ions relative to the FeO_6 octahedra (Figure 2.1a). The ferroelectric polarization have eight possible pseudo-cubic <111> orientations, corresponding to positive and negative orientation along the four cube diagonals, and the direction of the polarization can be switched by 180°, 109° and 71° (Figure 2.1b, c, and d, respectively) [41]. The antiferromagnetic ordering is G-type; that is nearest neighbor Fe moments are aligned antiparallel to each other in all three Cartesian directions (Figure 2.1e) [42].

Chapter 2.2 Structural Characterization of Ca-doped BFO

Chapter 2.2.1 Growing of BCFO Thin Films

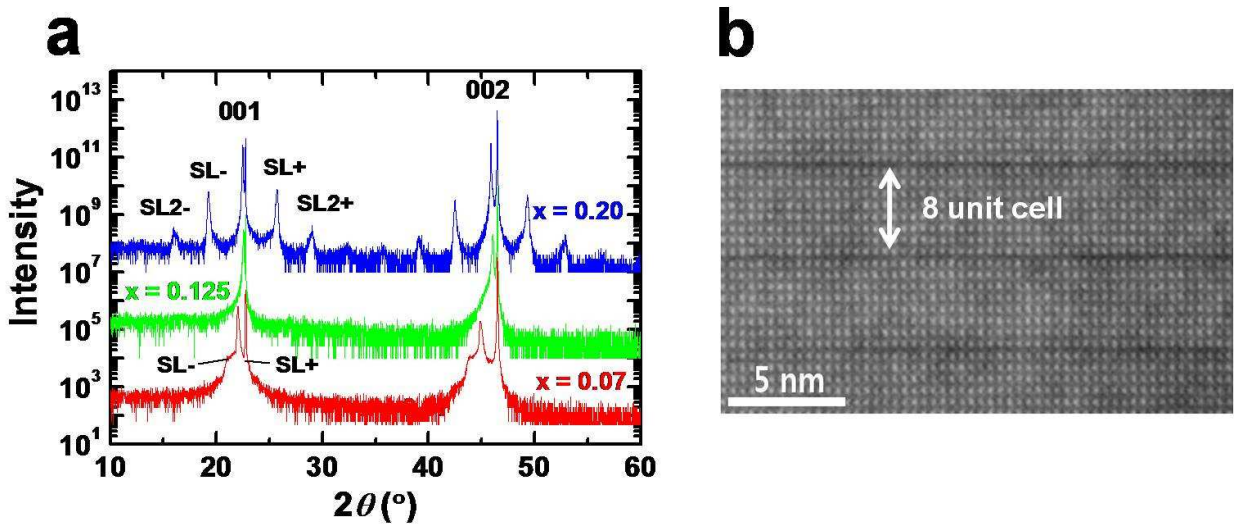

Figure 2.2: a X-ray *θ-2θ* scans of $BiFeO_3$ films with different Ca doping ratio at room temperature. x indicates the calcium doping ratio in $Bi_{1-x}Ca_xFeO_{3-\delta}$ thin films. Films of x-0.2 and 0.07 shows superlattice peaks implying a structural modulation along the out-of plane with a period of 7-8 unit cells and ~24 unit cells, respectively. Films of x=0.125 do not have any superlattice peaks. **b** TEM image of $Bi_{0.8}Ca_{0.2}FeO_{3-\delta}$ thin film. The different contrast lines are seen parallel to the sample surface with a period of 8 unit cells.

Ca-doped BFO films are grown on (001) $SrTiO_3$ (STO) substrates by using pulsed laser deposition method (See Appendix B for detail). The growth temperature is 600-700°C with 100 mTorr oxygen pressure. Typical deposition rates were approximately 2 nm per minute with a laser repetition rate of 10 Hz. The pulsed KrF excimer laser with 248 nm was focused to reach a laser fluence of ~2 J/cm^2 on the target surface.

Chapter 2.2.2 X-ray Diffraction Studies

Figure 2.2a shows the X-ray *θ-2θ* scans of different Ca doping ratio $BiFeO_3$ films. All films are shown to be fully oriented in {001} and highly crystalline (full-width-half-maximum of 001 diffraction peak of $Bi_{0.93}Ca_{0.07}FeO_{3-\delta}$ is 0.345°), which indicate the epitaxial BCFO film growth on STO substrate.

For the x=0.20 and 0.07 of $Bi_{1-x}Ca_xFeO_{3-\delta}$ films, superlattice peaks are observed around the BCFO {001} peaks, which present a structural modulation along the out-of-plane direction with a period of 7-8 unit cells and ~24 unit cells for x=20 and x=7, respectively. This is confirmed by the TEM image of x=0.20 films which shows different contrast lines are periodically repeated along the out-of-plane (Figure 2.2b), which is probably due to an oxygen vacancy ordering as has been reported in ferrites with perovskite structure [43-45]. The superlattice peaks become broader, weaker and closer to the (001) peaks with decreasing doping ratio, which indicates the relatively weak ordering with larger distance between these special planes. Interestingly, films of x=0.125 do not show any superlattice peaks.

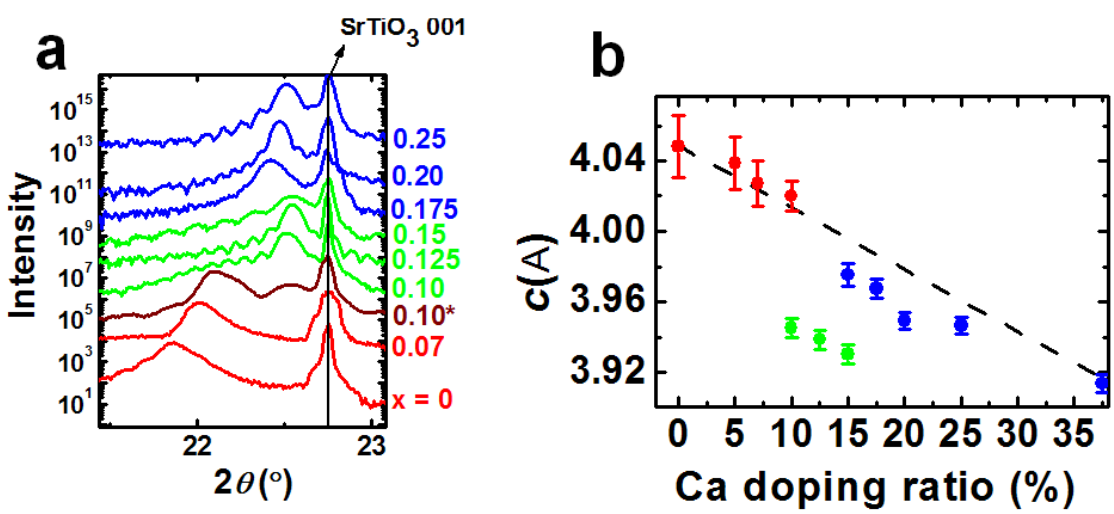

Figure 2.3: The existence of the superstructure is strongly related to the value of the c axis lattice parameter. **a** The X-ray diffraction data around the (001) peak are shown for the films with a thickness below 120nm to reduce the possibility of strain relaxation. **b** The influence of Ca doping on the c axis lattice parameter at room temperature. The black dashed line denotes linear interpolation between the lattice parameter of the films of $BiFeO_3$ and $CaFeO_{3-\delta}$ grown on (001) STO substrate.

The existence of the superstructure is strongly related to the value of the *c* axis lattice parameter. BCFO films of x=0.1~0.15 (represented in green lines in Figure 2.3a) do not have superlattice peaks and show large deviations in c axis lattice parameters from the Vegard's law compared to those of other doping ratios (Figure 2.3b). The black dashed line in Figure 2.3b denotes linear interpolation between the lattice parameters of the films of $BiFeO_3$ and $CaFeO_{3-\delta}$ grown on (001) STO substrate. For most Ca doping ratios the c axis lattice constants well follow the Vegard's law but the films of x=0.1~0.15 shows large deviation from the dashed line.

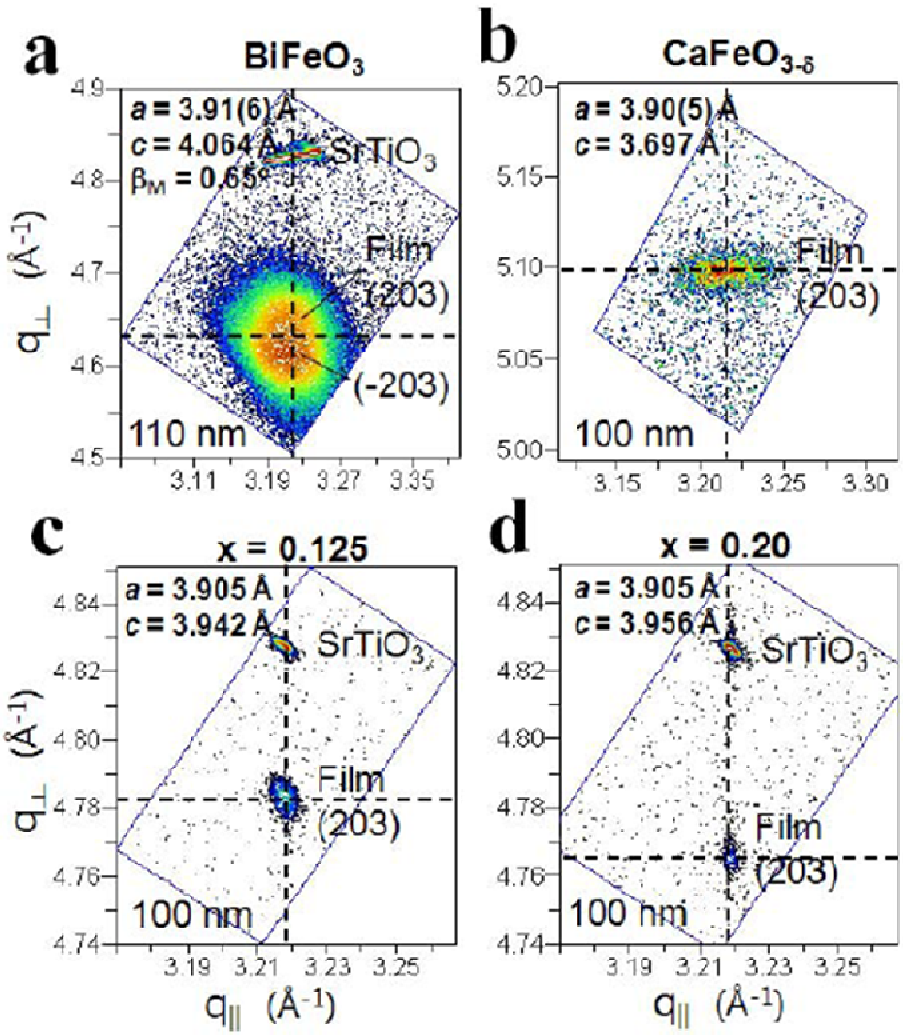

Figure 2.4: The X-ray characterization of the strain state of films. The reciprocal space mapping at room temperature of (203) peaks for the $Bi_{1-x}Ca_xFeO_{3-\delta}$ films: **a** x=0, **b** x=1.0, **c** x=0.125, and **d** x=0.2. The horizontal and vertical dashed lines represent the fully-strained pseudo-tetragonal position. The reciprocal space units are defined to be $2\pi/d$.

In order to investigate the dependence of c axis lattice constants on the stress relaxation of BCFO films, the 3-dimensional strain state was studied by X-ray reciprocal space mapping (RSM). The RSM for the 203 diffraction peaks were measured to determine in-plane lattice parameter and monoclinic angle (if any) for the films (Figure 2.4). The horizontal and vertical dashed lines indicate the fully-strained pseudo-tetragonal position expected from the in-plane lattice parameter of the substrate. As shown in Figure 2.4, films of $CaFeO_{3-\delta}$ (Figure 2.4b) and $Bi_{1-x}Ca_xFeO_{3-\delta}$ with x=0.125 (Figure 2.4c) and x=0.20 (Figure 2.4d), exhibit the 203 diffraction peak at the expected position; thus, they can be described through a fully-strained pseudo-tetragonal cell for a film thickness of ~100nm. This reveals that the in-plane lattice is fully strained to the substrate and the smaller c axis is not due to the stress relaxation. In addition, the possibility of volume reduction due to extrinsic effects such as bismuth evaporation can be excluded because the c axis lattice constant changes reversibly with phase transformation with respect to the temperature changes (Figure 2.5).

This correlation between the c axis lattice parameter and the existence of the superstructure can also be identified in the high-temperature transition observed in the film with x=0.15. The increase of the c axis lattice parameter measured above ~650 K (for x=0.15) is mainly due to this appearance of the superstructure. This experimental observation suggests that an oxygen vacancy ordering could be another degree of freedom that is inter-coupled in this system.

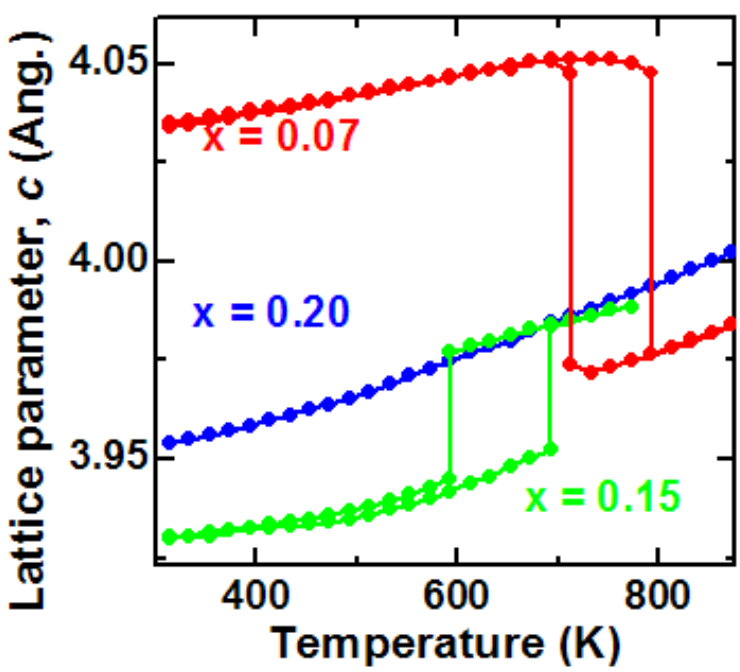

Figure 2.5: The temperature dependence of the c axis lattice parameter for films of x=20 (blue), x=0.15 (green), and x=0.07 (red).

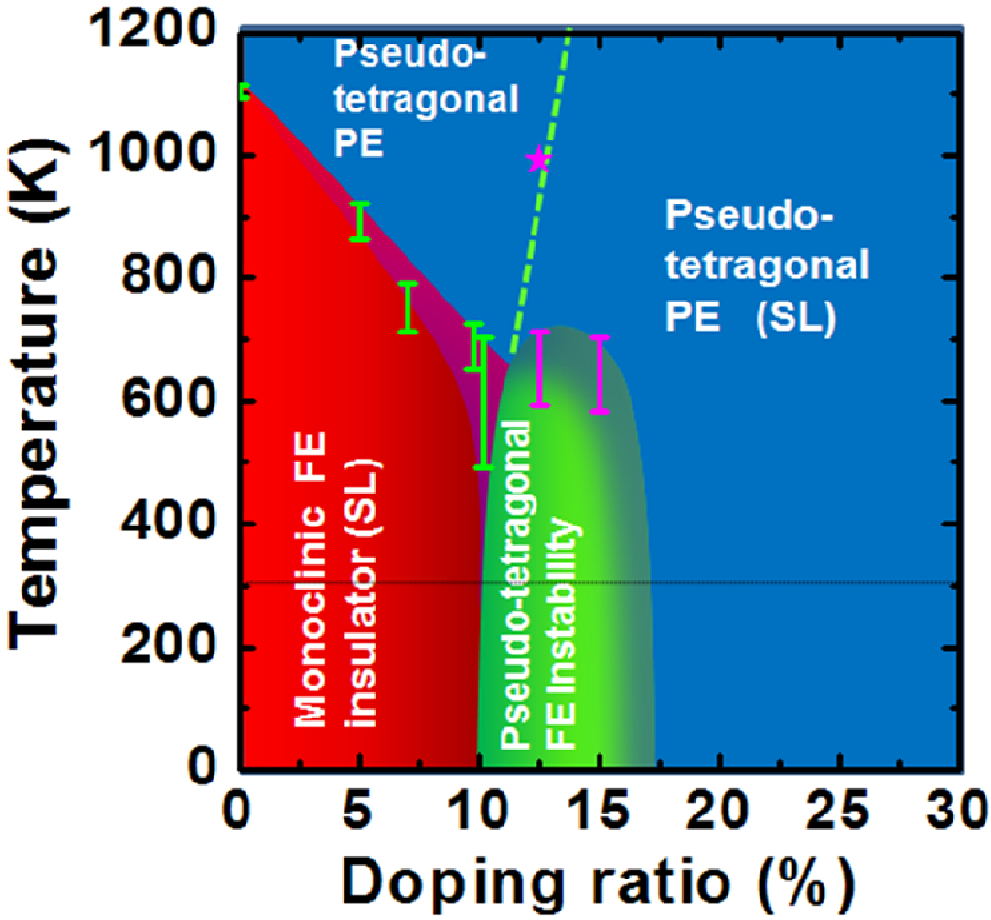

Figure 2.6: The proposed phase diagram of $Bi_{1-x}Ca_xFeO_{3-\delta}$ films grown on (001) STO substrates.

Chapter 2.2.3 Phase Diagram of BCFO

Based on the structural analyses, the phase diagram of the $Bi_{1-x}Ca_xFeO_{3-\delta}$ films is established as a function of the Ca doping concentration (x) and temperature (Figure 2.6). For the low Ca doping regime (x<0.1), the films with a monoclinic structure undergo a first-order transition to a pseudo-tetragonal phase at higher temperatures with a thermal hysteresis (Figure 2.5). On the other hand, the pseudo-tetragonal film with Ca doping ratio x=0.20 shows no such structural transition over the whole temperature range. This phase has clear superlattice peaks representing a long-range structural modulation along the out-of-plane direction. This modulation is robust even at high temperatures. The films with x=0.15, which possess the smaller volume phase, undergo a temperature dependent structural transition into the pseudo-tetragonal phase with the

appearance of the characteristic superlattice peaks as the temperature increases (Figure 2.5). The observation of volume increase at the transition is likely to be mainly due to the manifestation of the superstructure. In Figure 2.6, the extrapolation of the transition temperature results in the well-known ferroelectric Curie temperature (T_C) of BiFeO3 at ~1,100 K. With increasing Ca doping, the ferroelectric Tc rapidly decreases, and a *Tc* of ~600 K with a thermal hysteresis of 240 K is recorded at x=0.1. The samples in this region (x ≤ 0.1) show clear ferroelectric domain structure indicating ferroelectric long-range order, according to piezoresponse force microscopy (PFM) studies. For x > 0.15, the crystal structure exhibits a pseudo-tetragonal unit cell, piezoelectricity is not detected, and no anomalous change of the c-axis lattice parameter is observed from room temperature to 1100 K. For intermediate doping concentrations around x ~ 1/8, the ferroelectric monoclinic structure and the paraelectric pseudo-tetragonal structure are no longer present but a new pseudo-tetragonal phase is stabilized for the area described by green color in the phase diagram (Figure 2.6). Like the paraelectric phase above Tc, this phase has a smaller volume compared to the two neighboring phases.

Chapter 2.3 Electrical Characteristics of Ca-doped BFO

In this chapter, detailed electrical characteristics and ferroelectricity of BCFO are given by using a conductive atomic force microscopy (c-AFM) and a piezoresponse force microscopy (PFM, see Appendix C for detail), respectively. Based on the structural characterization, the pseudo-tetragonal ferroelectric phase, green region in the phase diagram (Figure 2.6), at x=0.10 was selected to investigate the electric characteristics of BCFO in expectation of the electric modulation of conduction and ferroelectric states. This phase is located near the phase boundary, which may make it susceptible to external electric fields in terms of both ferroelectricity and electric conduction, whereas for x<0.1 the electric conduction is not high enough and for x>0.15 the ferroelectric state is not stabilized.

	Bi	Fe	Ca
Ionic Radius (pm)	103	73.8	100
Valence State in BFO	3+	3+	2+

Table 2.1: The ionic radius and the valence state of Bi, Fe, and Ca ions.

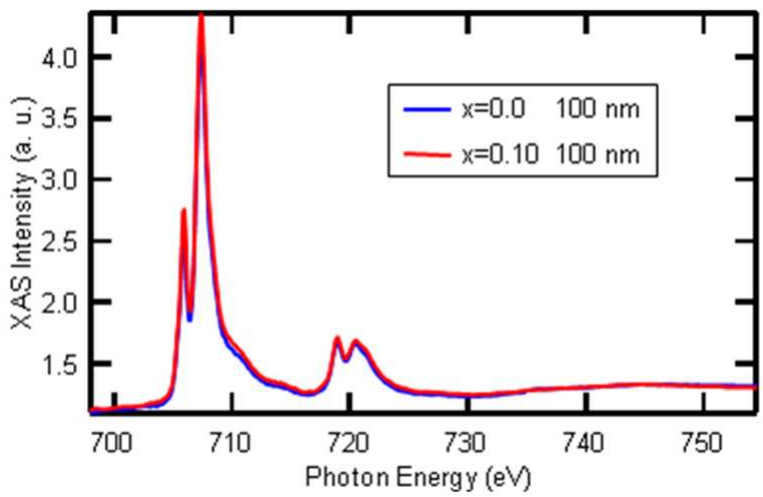

Figure 2.7: Fe *L*-edge X-ray absorption spectra (XAS) of $Bi_{1-x}Ca_xFeO_{3-\delta}$ thin films for x=0 and x=0.1.

Chapter 2.3.1 Electronic Properties of BCFO

In order to understand the electrical characteristics of BCFO, a detailed analysis of the electronic properties has been studied. In BCFO, divalent calcium ions substitute bismuth sites because their ionic radius is compatible to Bi^{3+} ion (Table 2.1). It's much larger than that of Fe^{3+} ion. As a result, the doping system has to produce holes by changing the valence state of Fe ions from 3+ to 4+ or oxygen vacancies to satisfy charge neutrality. For BCFO thin films, it is shown that oxygen vacancies are spontaneously generated to compensate calcium acceptors [46, 47]. This is proved by the X-ray absorption spectroscopy (XAS) measurements. The XAS spectra were obtained at room temperature by using linearly polarized light with parallel incidence with respect to the film normal. All spectra were obtained in total electron yield mode and the mesh current was simultaneously recorded for normalization. The divalent ion substitution (Ca^{2+}) does not change the 3+ valence state of Fe for the as-grown BCFO film as probed by XAS shown in Figure 2.7. No chemical shift of the Fe *L*-edge due to a mixed valence state has been detected in BCFO. The spectrum is comparable with that of un-doped BFO film indicating a Fe^{3+} valence state regardless of the Ca-substitution.

As in many other divalent-ion-substituted ferrite compounds, ionization of oxygen vacancies in Ca-doped BFO yields electrons to compensate hole carriers introduced by Ca ions to maintain the highly stable 3+ valence state of the iron ions in equilibrium state. According to the charge neutrality equation of Ca doped $BiFeO_3$, changes of local oxygen vacancy concentration from equilibrium value can alter electric properties of BCFO. The oxygen vacancy rich area turns into an n-type semiconductor and the oxygen vacancy deficient area turns to a p-type semiconductor by generating extra electrons and holes, respectively. This can be described by

$$2[V_O^{\bullet\bullet}] - [Ca_{Bi}'] + [h^{\bullet}] - [e'] = 0 \qquad (2.1)$$

where $[V_O^{\bullet\bullet}]$, $[Ca_{Bi}']$, $[h^{\bullet}]$, and $[e']$ indicate the concentration of oxygen vacancies, calcium ions, holes and electrons, respectively.

Chapter 2.3.2 Electric Modulation of Conduction States

The local electrical conductivity of BCFO was probed by conducting atomic force microscopy (Figure 2.8a). Using a conducting tip, micrometer-sized regions of the film were electrically switched with a set of positive and negative voltage (Figure 2.8b). A 3μm^2 region was poled by applying -12V (red square) and inside which a smaller 1 μm^2 region was subsequently poled downward with a voltage of +12V (blue square). For these regions, local currents were measured by the c-AFM technique with a voltage of -2.5 V.

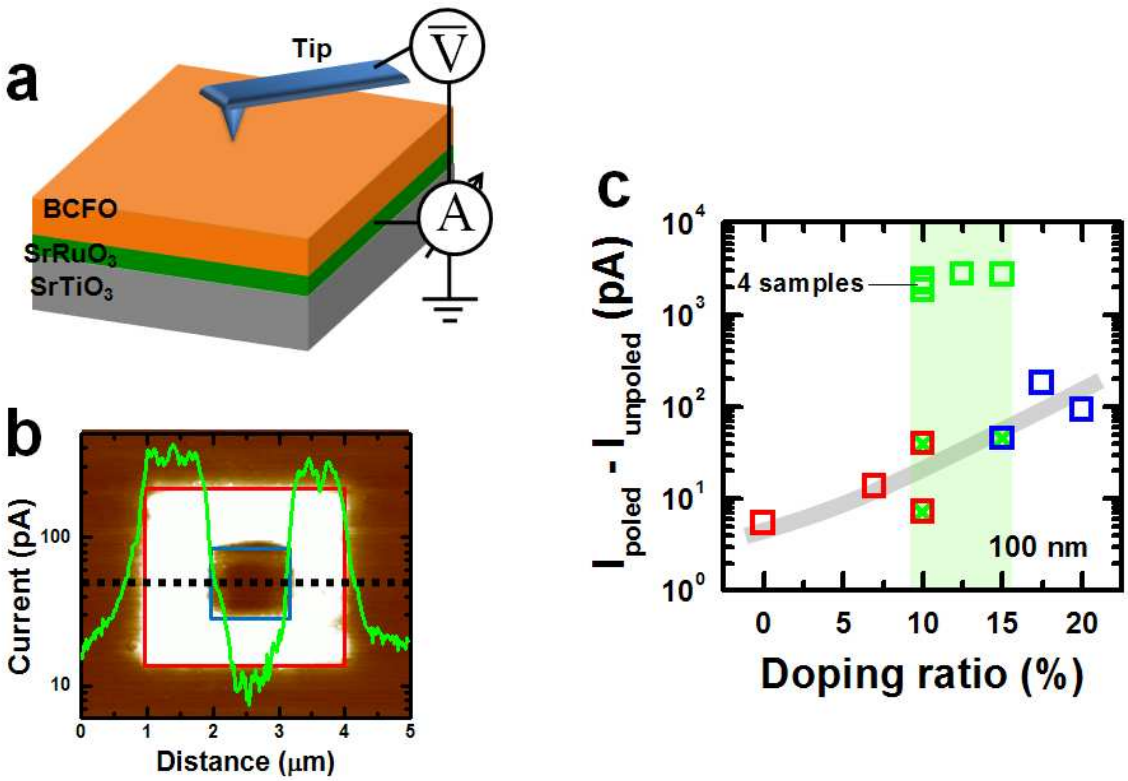

Figure 2.8: a Schematic diagram of the experimental set-up for local conductivity measurements for $Bi_{1-x}Ca_xFeO_{3-\delta}$ films by using c-AFM. **b** Electric-field-driven phase transition between an insulating state and a conducting state. The local current at the voltage of -2.5V to the tip was measured for a $Bi_{1-x}Ca_xFeO_{3-\delta}$ film (x=0.1) with a thickness of 300nm over a 5×5 μm^2 area after applying -12V on a 3×3 μm^2 area (red square) and sequentially poling with +12V on a 1×1 μm^2 area (blue square). The bright region exhibits high current. Inset: the current profile along the black dashed line. **c** The current enhancement by a negative poling is shown as a function of the Ca concentration. BCFO films with a thickness of 100nm were grown on 50nm-thick $SrRuO_3$ layers.

The region poled with -12 V shows a large increase of conductivity that can be switched back to the insulating state by applying a downward field of +12 V. The line profile of the c-AFM image plotted (on a log scale in green) reveals that the conducting state leads to a few hundred picoamperes of current that is modulated by at least two orders of magnitude. This observed contrast is repeatable over the same region as well as other regions of the sample. Figure 2.8c summarizes the current changes by poling (plotted as the difference between measured current in the poled and unpoled area) as a function of doping concentration. Interestingly, the largest conductive modulations are also observed in the concentration regime (shaded green in Figure 2.6) that shows the large deviations in lattice parameters from the conventional Vegard's law.

Chapter 2.3.3 Electric Modulation of Ferroelectric States

In order to study involvement of the ferroelectric sate corresponding conductive sate changes of BCFO thin films, PFM measurements for the same sample were carried out over the region poled using the same method described above (Figure 2.8a). The region outside the poling area shows clear ferroelectric domains, indicating that this Ca-doped (10%) sample is ferroelectric (Figure 2.9a). The three shades of image contrast, namely white, black and brown, found in this region of the PFM image indicate different directions of the polarization projected in-the-plane of the film, which are typical for BFO films grown on (001) STO substrates[48]. On the contrary, in the highly conducting region, no domain structure is observed and the brown tone in the PFM image is indicative of weak or no piezoresponse. Similarly as the conductivity change, transition between the ferroelectric and the non-ferroelectric state is reversible. In the region poled with +12V (blue square), strong piezoresponse (black color) and a black/brown contrast was detected, implying that the ferroelectric state has been recovered.

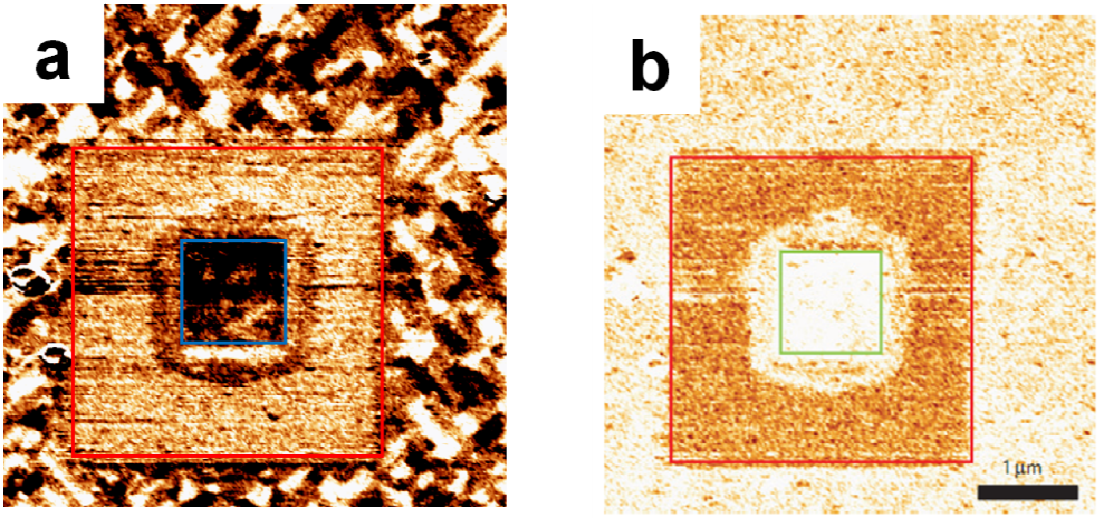

Figure 2.9: a In-plane PFM image over the poling area in which an electric field is applied as described in Figure 2.8. **b** Out-of-plane PFM image over the poling area.

The out-of-plane PFM (Figure 2.9b) also shows weak piezoresponse (brown colour) in the conducting area but the as-grown region and the region poled with +12 V exhibit white color, which implies the out-of-plane polarization direction is downward directed. These observations can be understood by the fact that the enhanced conductivity frustrates ferroelectric order by screening long-range Coulomb interaction, which has a key role in stabilizing the cooperative alignment of dipole moments [49].

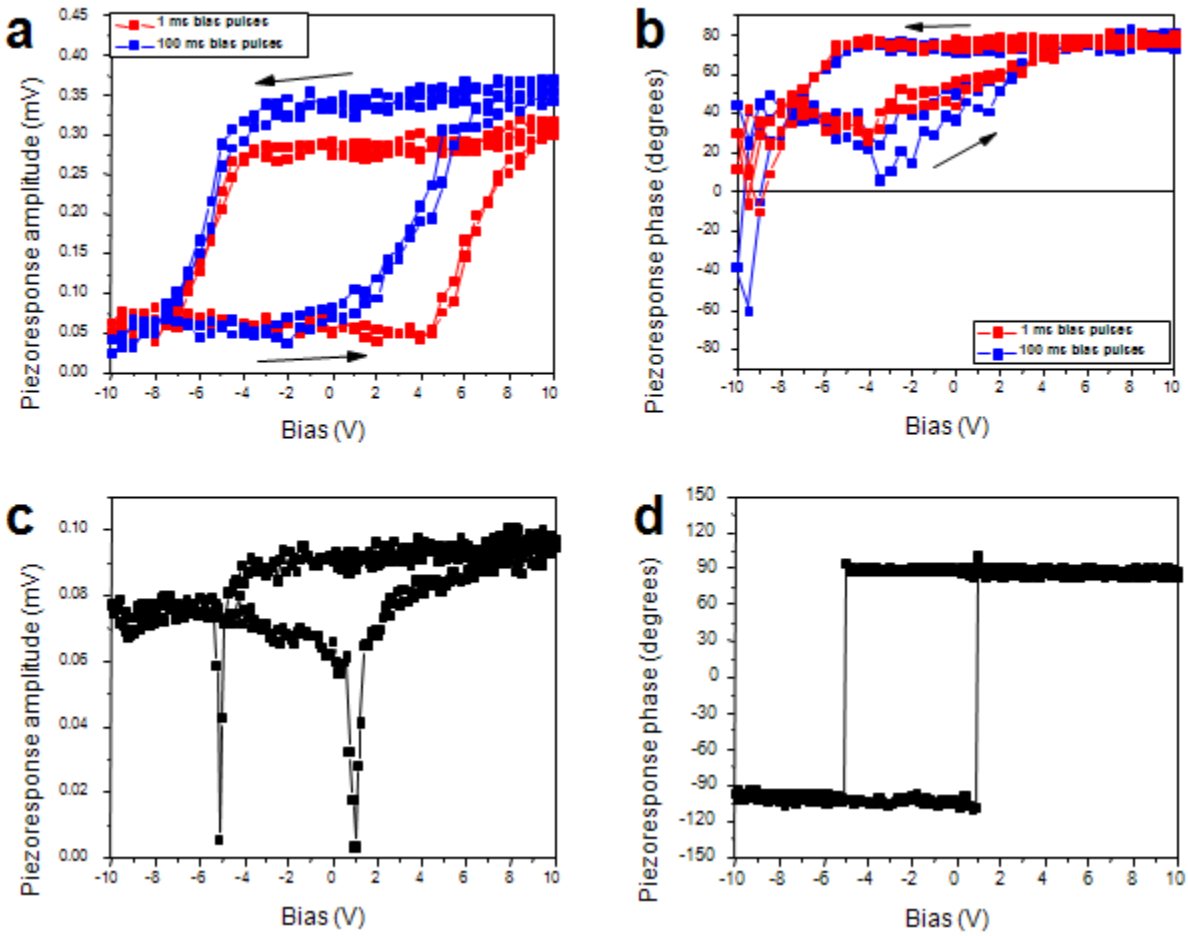

Figure 2.10: a, b Changes in piezoelectric response for $Bi_{0.9}Ca_{0.1}FeO_{3-\delta}$ film as a function of dc bias voltage following pulsed setting of the resistive state for 1ms and 100ms pulses. **a, b** Piezoresponse amplitude and phase signal, respectively. The bias is swept from 0V to -10V to +10V to 0V. **c, d** Piezoresponse amplitude and phase signal of undoped BFO thin film, respectively. The bias is swept from 0V to -10V, from -10V to +10V, and from +10V to 0V.

Chapter 2.3.4 Effect of Ca doping on Piezoresponse

In order to characterize the associated piezoelectric properties further, local piezoresponse measurements have been performed by using an c-AFM based setup. The piezoresponse curves consist of amplitude and phase information which gives insight into relative strength and direction of the local piezoelectric effect, respectively. In the measurements, for each curve a pulse with a certain monotonously increasing and decreasing bias was applied and the piezoresponse signal was acquired subsequently after each bias step at zero dc voltage. Figure 2.10a, b show piezoresponse curves obtained on a Ca-doped BFO film of thickness 100 nm. Two distinct types of dynamics are observed, depending on the polarity of the applied bias voltage. For positive bias a stable phase and high piezoresponse amplitude is observed indicating the ferroelectric state being present in the film. Upon application of increasing negative bias voltages the phase and amplitude decrease. The phase becomes increasingly noisy as the amplitude decreases close to zero value indicating a state of low or suppressed piezoresponse. Interestingly, the state of switching the ferroelectric is not or only incompletely reached.

The commonly observed "butterfly" shape of the amplitude in regular ferroelectric materials, e.g. undoped BFO (Figure 2.10c, d), is not present due to the electric field induced low resistive state. Together with the phase going close to zero this indicates a nonresponsive piezoresponsive state in the material due to screening of the applied bias by the induced conducting state. A clear dependence of the piezoresponse switching with applied effective field, i.e. voltage and pulse time can be seen in Figure 2.10a. For 100 ms pulses a state with higher piezoresponse is reached at +10V as compared to 1 ms pulses. In addition, the onset of switching back to the insulating, piezoresponsive state is reached earlier for 100 ms pulses, at about +4V as compared to about +7V for 1 ms pulses.

Chapter 2.3.5 Current (I)-Voltage (V) Characteristics of BCFO

In order to investigate this conduction modulation in more detail, *I-V* characteristics of the Ca-doped (10%) BCFO were evaluated (Figure 2.11). Same experimental set-up was used as Figure 2.8a. Numbers in Figure 2.11 indicate the sequence of the voltage sweep. Clear *I-V* hysteresis and transition from high resistance (OFF) state to the low resistance (ON) state are observed. On application of a high negative bias to the c-AFM tip with respect to the bottom electrode, the current is significantly increased with a nonlinear feature around a threshold voltage of ~-6 V and reaches ~350 nA at a voltage of -12V. Similar features are observed in positive voltage even though the shape is asymmetric. It's due to different voltage drops across the junctions of two different metal contacts. For the switching from the ON-state to the OFF-state, a high positive voltage has to be applied; otherwise, the current still exhibits a ON-state value at a voltage of -2 V (Figure 2.11b). This hysteric *I-V* shape can potentially be used for a resistive memory device; for instance, two different current states at -2V could represent ON/OFF states, respectively. Figure 2.11c presents that the ON/OFF switching is repeatable and reversible. This modulation also depends on the Ca concentration. The threshold voltage decreases with increasing Ca doping ratio and the current at a voltage of -12V is increased as the Ca concentration increases. The modulation becomes smaller for the BCFO with x=0.07 and eventually no large effect is observed in pure $BiFeO_3$ films (Figure 2.11d).

Interestingly, the *I-V* curve shape is changed to a diode-like behavior after applying high electric fields. This is the unique characteristic of BCFO compared to other conductive transition

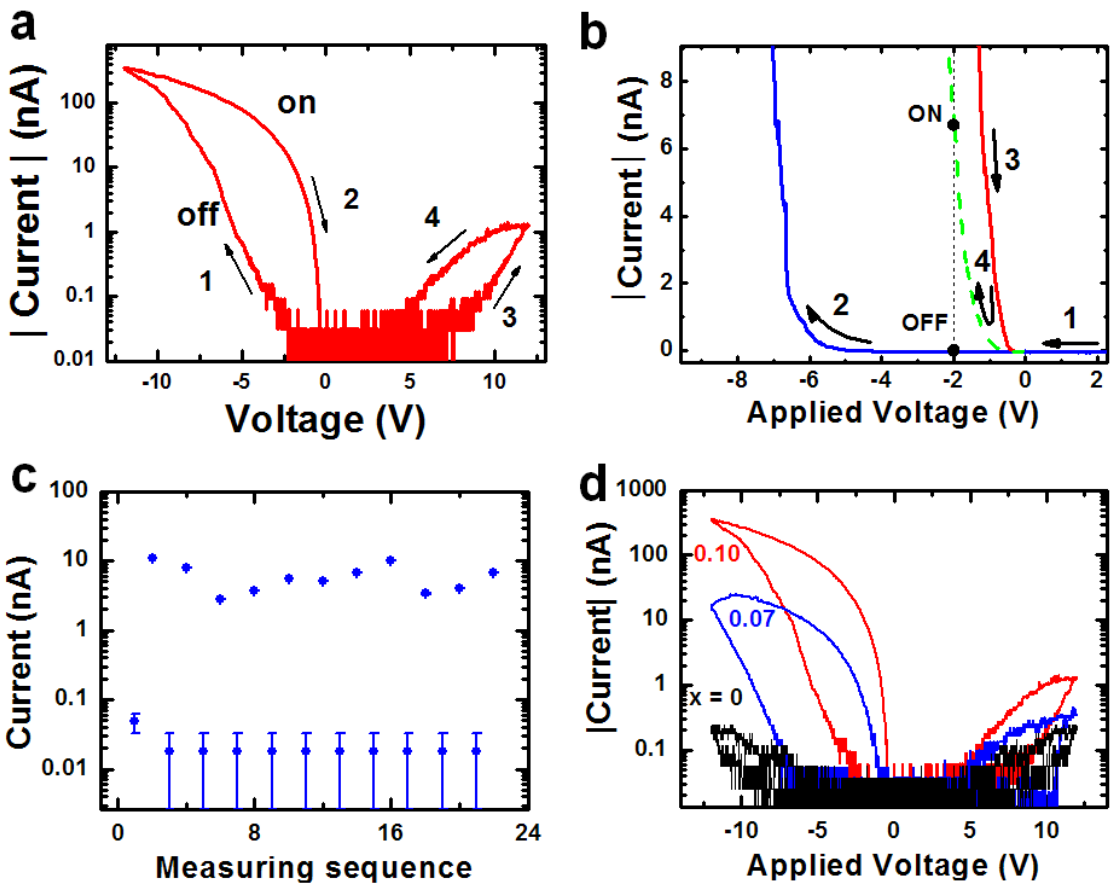

Figure 2.11: Local current (*I*)-voltage (*V*) characteristics. **a** The hysteric *I-V* curve of $Bi_{0.9}Ca_{0.1}FeO_{3-\delta}$ with 100 nm thick film measured by c-AFM. The voltage relatively applied to the tip is swept sequentially. The numbers denote the sequence of voltage sweeps. **b** The ON and OFF-state is nonvolatile and maintains until a large positive or negative voltage is applied. ON and OFF states at the reading voltage of -2V only can be set by applying 12V and -12V, respectively. **c** The repeatability of the hysteresis behavior. The current levels at the voltage of -2V while cycling the sweep are repeatable. **d** The Ca doping dependence of *I–V* hysteresis. Larger ON/OFF switching ratios are obtained with increasing doping ratios.

materials. Most of the oxide materials with a resistive transition have uni-polar current flow characteristics. That is the highly conductive ON-state is maintained without polarity dependence of applied voltage and mostly shows Ohmic behavior until switching to the less conductive OFF-state [50].

In order to eliminate possible effects of Schottky contact resistance at the interface between the tip and ferroelectric films [51], a conventional capacitor structure was fabricated using an epitaxially grown tri-layer of $SrRuO_3$ (50 nm)/$Bi_{0.9}Ca_{0.1}FeO_{3-\delta}$/ $SrRuO_3$ (50 nm). The resistance switching behavior has been reproduced in this structure as well and the *I-V* curves also shows

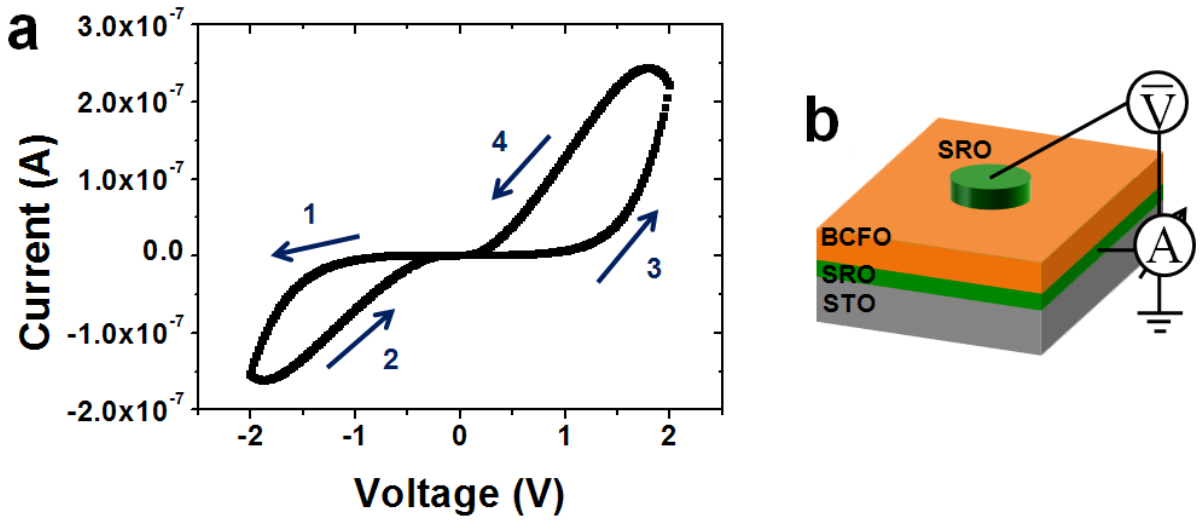

Figure 2.12: Symmetric *I-V* curve of BCFO with identical top and bottom electrodes. a The hysteric *I-V* curve in the conventional capacitor geometry. **b** Schematic diagram of the experimental set-up for *I-V* measurements. $SrRuO_3$ (50nm)/$Bi_{0.9}Ca_{0.1}FeO_{3-\delta}$ (100nm)/ $SrRuO_3$ (50nm) are in-situ epitaxially grown on STO (001).

diode-like characteristics (Figure 2.12a). The direction of the diode is also switched as the resistance states changed. In other words, the current in the ON-state is the forward current and the OFF-state current is the reverse current of the diode which has the opposite direction. This system shows bipolar and non-volatile memory characteristics and the ON/OFF ratio is over 2 orders of magnitude.

Chapter 2.4 Behavior of Oxygen Vacancies in BCFO

Chapter 2.4.1 Relaxation of the Conductive State

Oxygen vacancies created by calcium doping to maintain charge neutrality are critical to understand the conduction characteristics; so it is very important to understand the behavior of oxygen vacancies. To validate the oxygen vacancy movement we investigate the time and temperature dependent relaxation of the highly conductive ON-state. For this study local micron sized areas of the sample are poled using the c-AFM with a voltage of -10V to switch these areas to ON-state. These areas are then imaged by c-AFM and mean current values were extracted from the data as a function of time and temperature. Figure 2.13a shows a change of c-AFM images of a poled area as a function of time. The samples were kept at 100°C in atmosphere after poling. Clearly, a decay of the conductive state can be seen over time. Figure 2.13b shows more

detailed data for various temperatures from room temperature up to 125°C. An accelerated decay of the conducting state with increasing temperature is observed. The relaxation shows a nonlinear step-like transition upon relaxing to the insulating state for all temperatures.

Assumed that the relaxation of the conductive state is mainly attributed to the diffusion of oxygen vacancies the diffusivity of the oxygen vacancy in BCFO can be extracted. On the basis of Fick's second law and the assumption that the inter-diffusion length for one week is of the order of the film thickness (~100 nm), the diffusivity (*D*) of oxygen vacancies can be estimated to be ~10^{-17} cm^2s^{-1}. This is a reasonable value for the oxygen vacancy movement in non-stoichiometric perovskite oxides and related compounds [52-54].

Chapter 2.4.2 Behavior of Oxygen Vacancies in Electric Field

Generally oxygen ions and also oxygen vacancies are known as immobile at RT. The aforementioned diffusivity of oxygen vacancies in BCFO is very low (~10^{-17} cm^2s^{-1}) and the mobility calculated from this diffusivity is ~10^{-15} $cm^2V^{-1}s^{-1}$. So if the drift velocity of oxygenvacancies increases linearly with an applied electric field it's really hard to explain the switching mechanism with the oxygen vacancy movement.

However, it has been reported that a very high electric field can significantly reduce the activation energy for ion migration (Figure 2.14a), which result in the exponential increase of ion drift velocity in high electric field region (Figure 2.14b) [55]. This relationship can be described by

$$\upsilon = \begin{cases} \mu E & E \ll E_0, \\ \mu E_0 e^{E/E_o} & E \sim E_0, \end{cases} \tag{2.2}$$

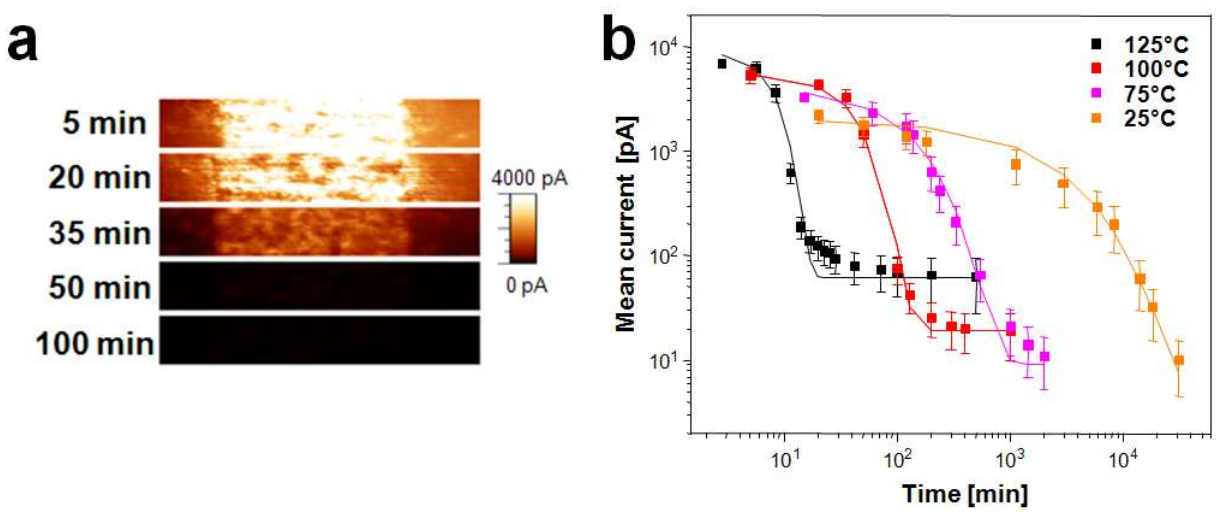

Figure 2.13: Time and temperature dependence of the conductive state. a c-AFM images of the decay of current in a poled box (-10 V) over time at 100°C. **b** Mean current of a poled box as a function of elapsed time for various temperatures.

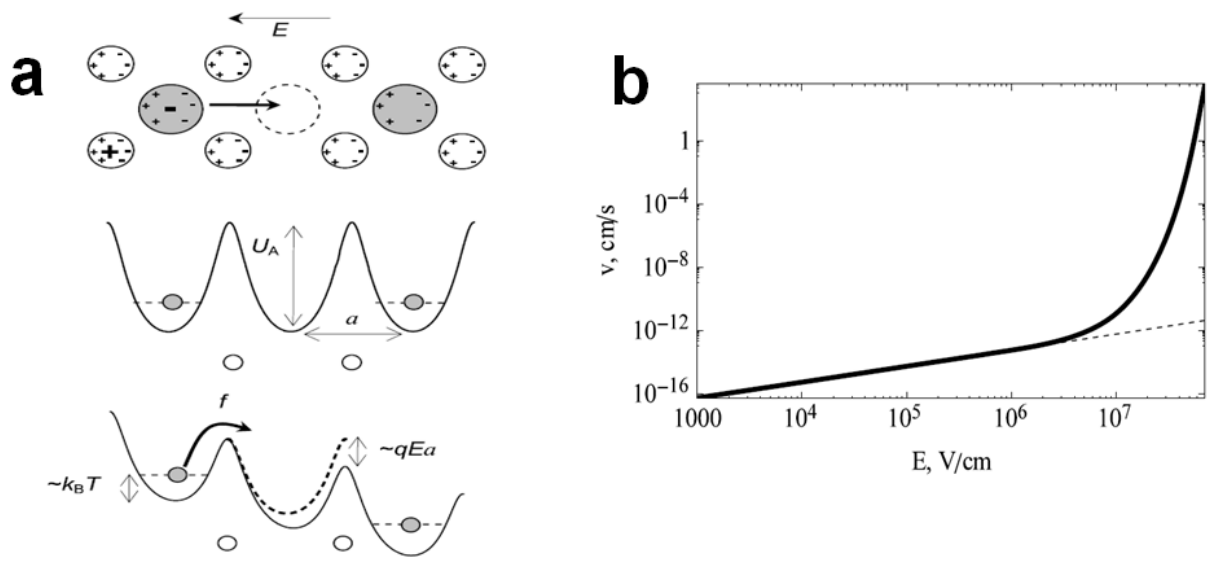

Figure 2.14: a Schematic diagram of an oxygen vacancy diffusion (top picture) and corresponding potential energy profile without (middle picture) and with (bottom picture) a high electric field. The activation energy is reduced by ~*qEa*. **b** Nonlinear (solid) and linear (dashed) drift velocity of oxygen vacancies along the [110] direction in rutile at room temperature [51].

where, υ, μ and E are the drift velocity, the mobility of oxygen vacancies and the electric field, respectively. $E_0 = 2k_BT/(qa)$ (Here, k_B, T, q, and a are the Boltzmann constant, temperature, charge of electron and hoping distance, respectively) is the characteristic field for a particular mobile atom in the crystal, which is typically about 1 MV/cm for T = 300 K [55]. Significant increases over the linear drift law have been experimentally proved [56-58].

Based on this non-linear drift velocity equation we can calculate the drift velocity of oxygen vacancies in BCFO as a function of the applied electric field. As shown in Figure 2.15a, the drift velocity exponentially increases beyond the characteristic field (1MV/cm). The characteristic field (~1 MV/cm) seems to be a huge value but if we consider the thickness of the BCFO used for our experiment is 50~100nm the actual applied voltages for that electric filed are in 5~10V which are within our experimental range.

In spite of exponential increase of the drift velocity, physical breakdown of films in such a high electric field is a potential problem. The breakdown field of BFO varies depending on a film quality. The film of epitaxial growth showed higher breakdown field (> 1MV/cm) but poly-crystalline films were undergoing dielectric breakdown at much lower electric field (~600kV/cm) [59]. However, it is noted that such a high electric field required for exponential ion transport may still be much lower than the critical field for dielectric breakdown of the oxide. The electric field used in (2.2) is the local electric field, which is much higher than the average electric field. The average electric field, E_A, is determined by the applied voltage, V ($V = \int E_A(x)\mathrm{d}x$, where, x is a distance) and the dielectric breakdown field represents this average electric filed. The local electric field is the actual field experienced by an individual ion in a dielectric [60]. The local

field depends not only on the applied field but also on the arrangement of polarized ions. The local electric field is represented by

$$E_{\text{local}} = E_{\text{A}} + (f/\varepsilon_0)P = (1 + f\chi)E_{\text{A}} \tag{2.3}$$

where, E_{A}, P, f; and χ are the average electric field, the polarization density, the Lorentz factor and the permittivity of crystal, respectively. The Lorentz factor and the permittivity are always positive values; so the local field is always larger than the average applied field. The Lorentz factor in dielectric materials arises from the fact that a polarizable atom sees an electric field which is different from the simple space average of the electric field. The polarizable atom under consideration sees this different local field because it is not at an average position but guaranteed to be at a position outside that of the other polarizable atoms [61, 62]. It strongly depends on a crystal structure and for cubic it is 1/3 [60]. Figure 2.15b shows that the onset electric field for exponential increase of the drift velocity shifts as a function of the Lorentz factor. Therefore, it is possible to observe strongly nonlinear oxygen vacancy transport with electric fields well below the breakdown field of BFO.

Chapter 2.5 Mechanism of the Electronic Conduction Switching

Chapter 2.5.1 Resistive Switching Model: Interaction of Ionic and Electronic Conduction

Based on the nonlinear relationship between the mobility of oxygen vacancies and the

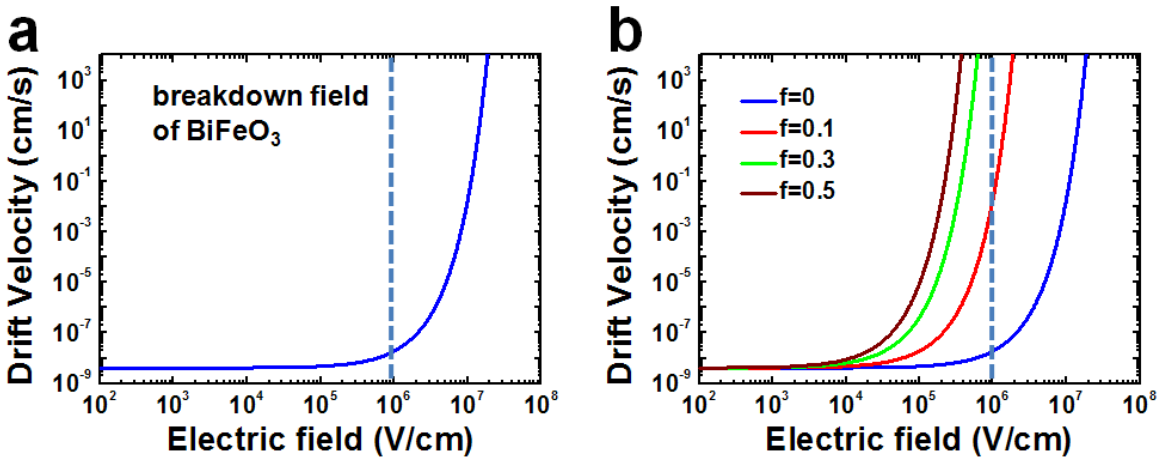

Figure 2.15: Drift velocity of oxygen vacancies. a Calculated drift velocity of oxygen vacancies based on the nonlinear equation. **b** The change of drift velocity as a function of Lorentz factor. 'f' represents Loentz factor. The blue dashed lines indicate the dielectric breakdown field of BFO.

applied electric field and the charge neutrality condition, the resistive switching mechanism can be established by the model of the interplay of the ionic conduction by oxygen vacancy movement in a high electric field and the electronic conduction by subsequent mobile charge carrier generation.

As shown in Figure 2.16a, the oxygen vacancies are uniformly distributed throughout the BCFO thin film in the as-grown state. Assuming that the charge neutrality is satisfied by fully ionized calcium ions and oxygen vacancies to maintain the 3+ valence state of the iron ions, holes generated by calcium ions are mostly compensated by electrons generated by ionized oxygen vacancies; so it is in the highly insulating state (region A). Provided that the oxygen vacancies are mobile positive charges, they can move through the BCFO film under electric fields to find a new thermodynamic equilibrium [63, 64]. As discussed previously, applying large

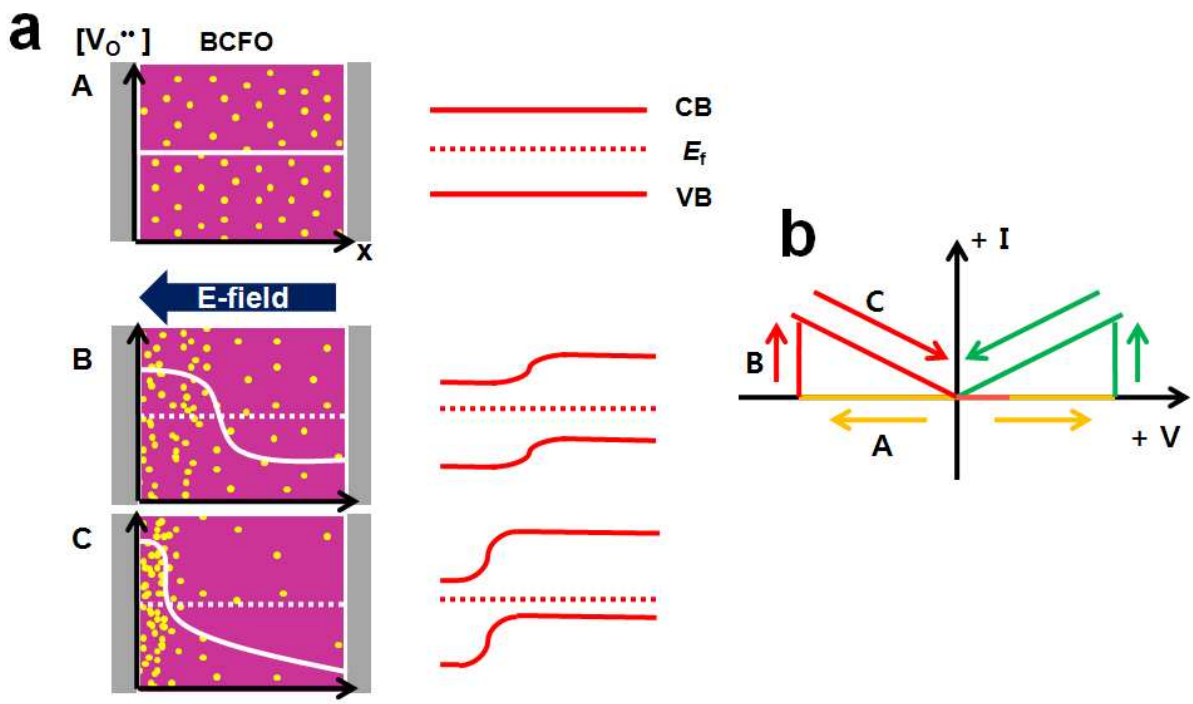

Figure 2.16: Schematic diagram of the resistive switching mechanism. a Oxygen vacancies are uniformly distributed through BCFO in the as-grown state (region A). By applying an electric field oxygen vacancies are moving to the cathode and accumulating near this electrode (region B). The local concentration of an oxygen vacancy is increased with increasing applied voltage and reach to the saturation value (region C). Yellow solid dots indicate oxygen vacancies. The white solid and the white dashed lines represent a concentration profile of the oxygen vacancy and an equilibrium concentration of the oxygen vacancy, respectively. The corresponding band diagrams for each state are drawn on the right side. The oxygen vacancy rich area turns into a n-type and deficient area becomes a p-type semiconductor. **b** Schematic *I-V* curve of BCFO. Capital letters corresponds to the state in Figure 2.16a.

electric field over the threshold voltage nonlinearly increases the drift velocity of oxygen vacancies and forces oxygen vacancies to move fast to the cathode and to pile up near this electrode. As a result, the donor oxygen vacancies and the acceptor calcium ions are locally unbalanced; thus, the region near the cathode (oxygen vacancy rich area) acquires n-type carriers, whereas the region near the anode (oxygen vacancy deficient area) becomes p-type. This electric field-driven n-p junction explains the aforementioned diode-like *I-V* shape. Therefore, in Figure 2.16b, the initial steep increase of the current (region B) is due to the combination of ionic conduction by oxygen vacancies and electronic conduction by electrons and holes generated by the local unbalance of acceptor and donor ions. As the applied electric field increases, the concentration of oxygen vacancies near the cathode increases; thus, this region gets more n-type carriers and the region near the anode acquires more p-type carriers. After forming n-p junction, the conduction is mainly controlled by electrons and holes, which results in highly conductive ON-state (region C) compared to the initial highly insulating OFF-state (A). Applying the opposite electric field moves oxygen vacancies to find the original evenly distributed state, thus forming an electronic insulator. As seen in Figure 2.12a, this diode is switchable. The *I-V* curve follows the same hysteric loop with applying opposite bias voltage (The green lines in Figure 2.16b).

Chapter 2.5.2 Temperature Dependence of I-V Characteristics

In order to probe this electronic conduction mechanism, *I-V* measurements were performed in various temperature by using a coplanar device structure (Figure 2.17a). As seen in Figure

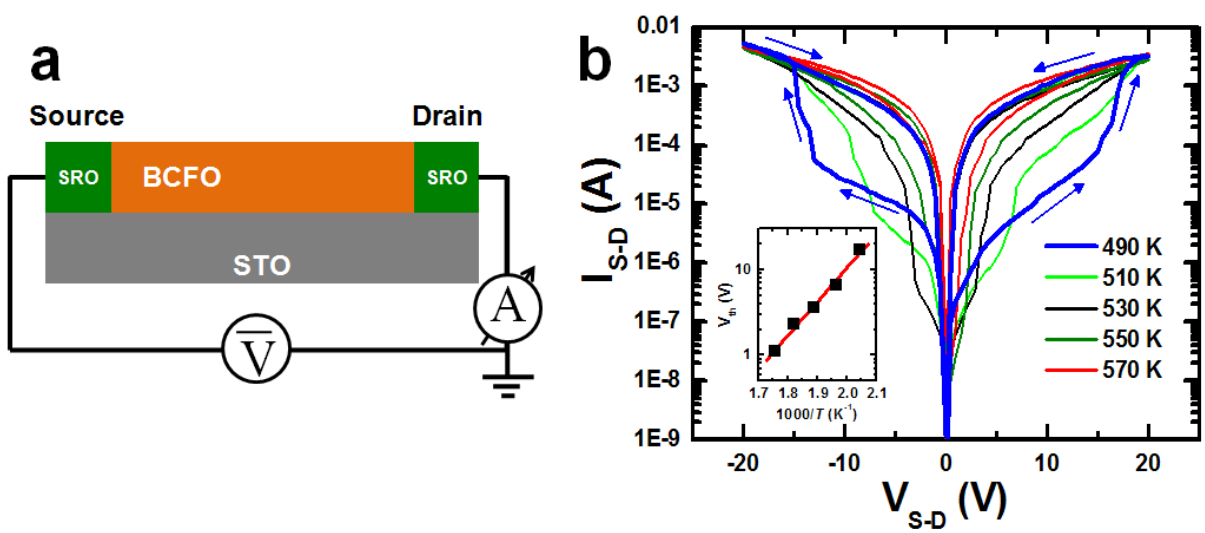

Figure 2.17: Temperature dependence of *I-V* curves. a Schematic diagram of coplanar device structure and electric measurement set-up. The distance between the source and the drain is 6μm. **b** *I-V* curves of BCFO as a function of temperature. Inset: Arrhenius plot of the threshold voltage.

2.17b, the threshold voltage for the resistive switching decreases and the hysteresis effect is emaciated with increasing temperature. These temperature dependences can be well understood by the enhancement of the mobility of oxygen vacancies at higher temperature and can be strong evidence that the oxygen vacancy movements are responsible for the conductivity changes.

Figure 2.17b clearly show the most interesting and peculiar characteristics of BCFO. The peculiar p-n/n-p junction switching characteristics and the threshold behavior are reproduced in the *I-V* measurement for this planar electrode structure.

Chapter 2.5.3 Local Conductivity Measurement of BCFO

In order to probe this electronic conduction mechanism, the local conductivity was measured by using a same electrode structure in previous chapter. Films were poled under elevated temperatures to facilitate the insulator-conductor transition across the two electrodes separated by 6 μm within reasonable voltage ranges. The distribution of the oxygen vacancy concentration was controlled gradually between the two electrodes by applying +20 V to the source electrode for one minute at 473 K (Figure 2.18a) and sequentially by quenching to room temperature so that the distribution is frozen (Figure 2.18b). The local conductivity was measured by using c-AFM with scanning a conductive tip at -1.5V as shown in Figure 2.18c.

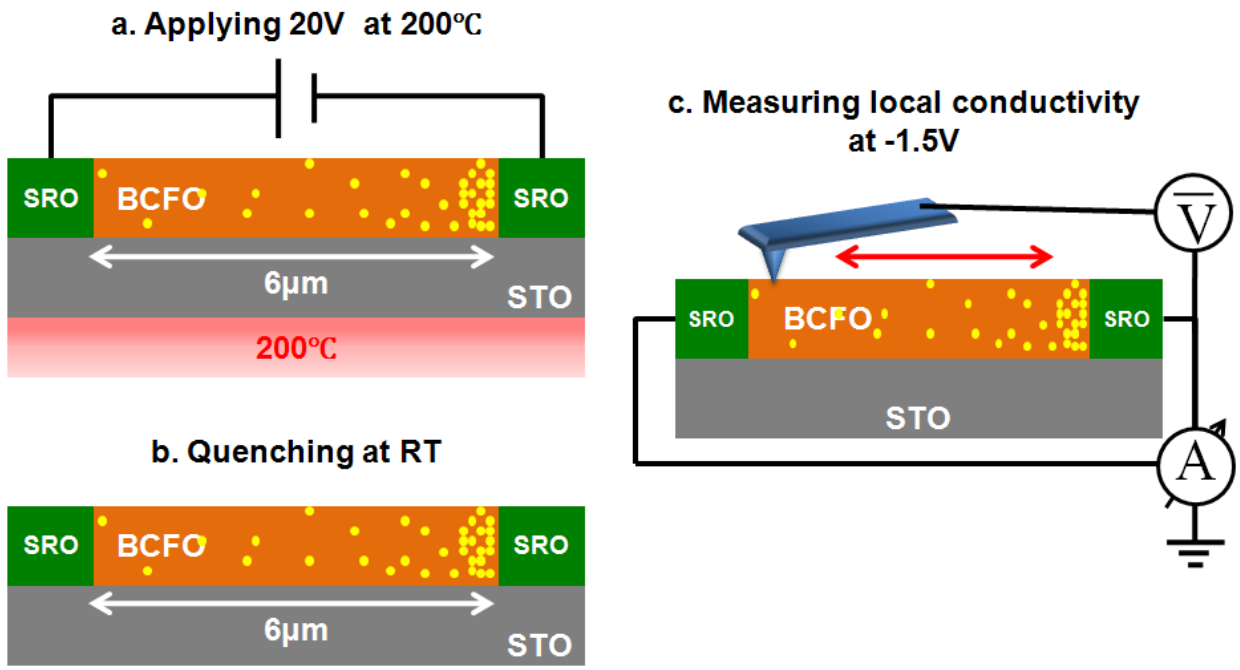

Figure 2.18: Illustrations of the poling sequence for the local conductivity measurement. Yellow solid dots represent oxygen vacancies.

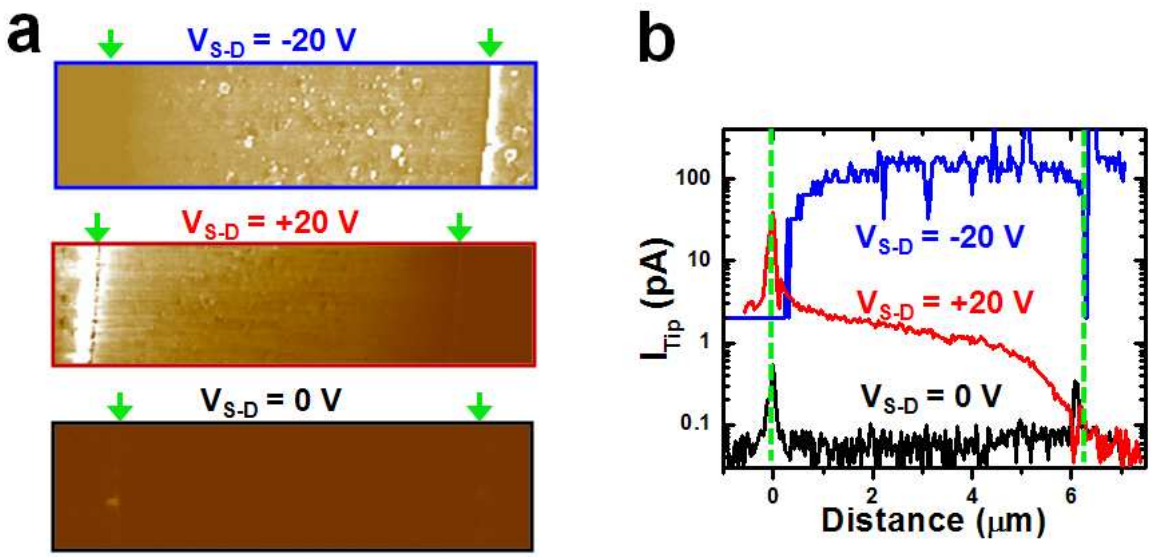

Figure 2.19: a c-AFM images with a tip voltage of -1.5V. The top and the middle panels represent the c-AFM images of which are poled with a voltage of -20V and +20V, respectively. For a reference, the c-AFM image of which are heated without poling is shown in the bottom panel. **b** The horizontal profiles for the c-AFM results. The green arrows indicate the source and the drain and are corresponding to the dashed lines.

As expected, c-AFM measurements (Figure 2.19a, b) show a gradually varying current profile. The region near the source electrode is conducting owing to a high hole carrier density, whereas the opposite narrow region near the drain electrode reveals an insulating state. It might be due to the low electron mobility in this n-type region because of the increased defect density in this area. On the other hand, the application of -20 V to the source electrode makes the gradient profile reverse. The exclusion of side effects arising from the heating can be ascertained by the observation of no conductivity enhancement for an unpoled reference pattern fabricated on the same film.

Chapter 2.6 Conclusions

The effect of calcium doping on multiferroic $BiFeO_3$ films was investigated and a phase diagram was built by varying the doping concentration and temperature. A ferroelectric paraelectric boundary exists at doping levels of x=~1/8, stabilizing a pseudo-tetragonal phase that has a relatively smaller volume than that expected from conventional Vegard's law. Reversible resistive switching was observed by applying electric field along both the normal and in-plane directions. In both cases, electronic conduction can be modulated in a similar way. The mechanism can be well established based on the interplay of ionic and electronic conduction.

Chapter 3 Memory Device Application I: Ca Doped $BiFeO_3$ Hetero-junction Diode

In this chapter, the nonvolatile memory device by using BCFO thin films is introduced. Based on the characteristics of BCFO discussed in Chapter 2, I have combined BCFO with an n-type semiconductor, La doped $SrTiO_3$ (SLTO), to build up a hetero-junction diode with the expectation of a resistance transition with a rectified current flow behavior. Design concept, detailed electric characteristics, and the switching mechanism of the BCFO/SLTO hetero-junction device are discussed.

Chapter 3.1 Design of New Memory Device with BCFO

As information technology progresses toward mobile environments and current technologies are continuously faced with the difficult issue of scaling, efforts to find new memory devices have been accelerated [65, 66]. As I already described in Chapter 1, many kinds of new device schemes have been proposed to replace current memory devices [67, 68]. Among those memory devices, resistance-change random access memory (RRAM) holds one of the spotlights due to aforementioned promising characteristics [69-71].

However, a difficulty in realizing a random accessibility is one of critical issues confronted during integrating such memristors into memory devices. In this chapter, I introduce the design concept for creating new RRAM device with BCFO to solve this problem. The design concept focuses on maintaining the simple cross-point cell structure and fabrication simplicity.

Chapter 3.1.1 Issues for Random Access Ability of Current RRAM Device

From a practical point of view, the simple cross-point cell structure of RRAM (Figure 3.1) might be the most attractive point. As I have mentioned in chapter 1, this structure has the physically minimum cell size, $4f^2$, (f indicates the smallest half pitch size of devices) and it is simple to fabricate; requiring no patterning of the active layer (resistance change layer) and no strict alignment [72].

However, the unipolar current flow characteristic of the device can lead to errors during reading via low resistance paths through unselected neighboring cells. Figure 3.2a shows a typical reading error of the simple 2×2 cross-point cell array. The high resistance cell (HRS) is selected to read but the reading current flows through the surrounding low resistance cell (LRS) and thus the wrong information of the selected cell is transmitted.

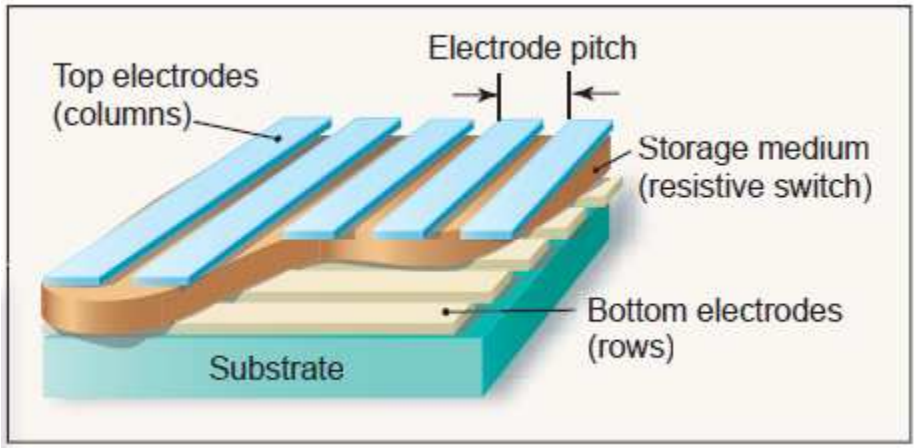

Figure 3.1: Schematic diagram of cross-point cell structure [72]. The cell size is determined by the electrode pitch size (width of an electrode + width between electrodes) in an ideal case.

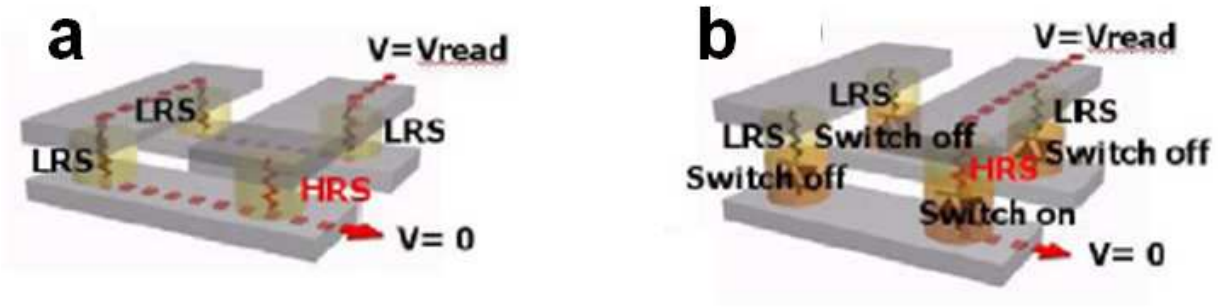

Figure 3.2: Schematic diagram of simple 2×2 cross-point cell structure without and with diodes. a Illustration of a error during reading bit information of the HRS (High Resistive State) cell. The current flowing through unselected LRS (Low Resistive State) cells delivers an wrong bit information. **b** Rectified reading operation effectively prevents a reading error in the cross-point cell structure [73].

Conventional pathways to prevent this are to combine a transistor or a diode with every memory cell but the former one inevitably enlarges the cell size and complicates the cell structure. The latter holds promise for improvement because it can maintain the ideal cell size [73]. As shown in Figure 3.2b, the rectifying characteristic of the attached diode prevents the reading current flow through unselected LRS cells. However, the diodes should be patterned in stand-alone shape for complete isolation from other cells for this device structure. Therefore, the best way to deal with these issues is to design memory cells that are endowed with rectifying characteristics at their low resistance (ON) state, to avoid any fabrication difficulties and to keep their simple configuration.

Chapter 3.1.2 Design Concept of BCFO/SLTO Hetero-Junction Memory Device

The design concept of the BCFO/SLTO hetero-junction memory device is based on the following requirements; (1) reversible resistive changes, (2) one-directional rectified current flow to avoid misreading, and (3) no strict alignment of top and bottom electrodes for device processing.

As mentioned in the previous chapter, in order to avoid read errors in such a cross-point cell structure, a diode can be used to cut the path through low resistive (ON-state) unselected cells. However, the demerit of this device scheme is the necessity of the strict alignment of the array of top and bottom electrodes. The diode layer can be a bypass of the current flow (Figure 3.3a); so the diodes should be patterned in stand-alone shape for complete isolation from other cells (Figure 3.3b). As a result, a strict alignment is required for top and bottom electrodes with the patterned diodes of each cell. However, if rectifying behavior comes from the junction between an active layer and a bottom (or top) electrode, random accesses are possible without any active layer patterning and strict alignment (Figure 3.3c).

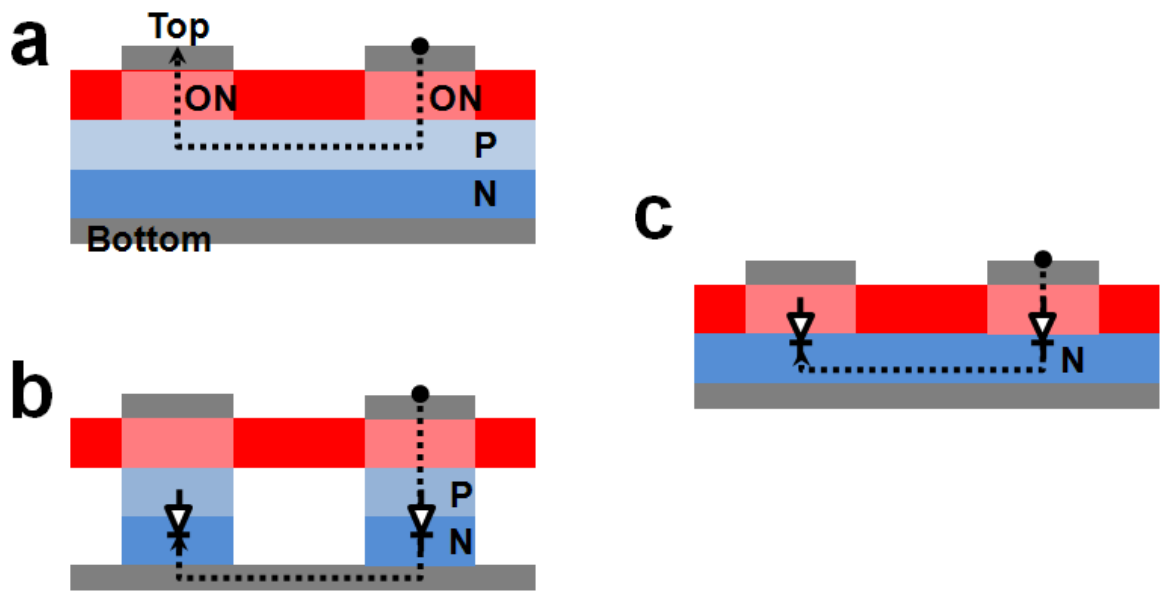

Figure 3.3: Schematic diagram describing the current path. a Currents can flow through conductive semiconductor layers and unselected, ON-state cells. **b, c** Currents are blocked by diodes and hetero-junctions, respectively. Red layers indicate active layers and ON state cells are represented in pink. P and N indicate p-type and n-type semiconductors, respectively.

Chapter 3.1.3 Resistive Switching of BCFO/SLTO Hetero-Junction

In order to demonstrate this concept, BCFO (active layer) and SLTO (bottom electrode) are combined to make an oxide hetero-junction diode with a metal top electrode. According to the proposed band diagram of the hetero-junction, BCFO/SLTO junction is expected to form a staggered gap type p-n junction (Figure 3.4a).

In the as-grown state, oxygen vacancies are uniformly distributed through the whole BCFO thin film (Figure 3.4b). Although I have not obtained any reliable results about the charge carrier type of BCFO, it is reasonable to consider BCFO as a slightly hole doped system in the as-grown state [74]. In addition, the recent experimental results showed that the band gap for Ca doped $BiFeO_3$ ($Bi_{0.9}Ca_{0.1}FeO_{3-\delta}$) is similar to that of pure $BiFeO_3$ (~2.7eV [75]). Therefore, based on the work function difference of BCFO and SLTO, J2 forms a staggered gap type p-n junction (Figure. 3.4b), which is expected to enable rectified current flow [76]. It is believed that Pt makes Schottky contact with BFO [77, 78]. Therefore, in the case of a metal (Pt) and a semiconductor (BCFO) contact (MS contact), i.e. J1, a Schottky contact is expected. As a consequence, Pt/BCFO/SLTO junctions consist of the Schottky contact (J1) and the p-n junction (J2), which have opposite diode directions (Figure 3.4b). Thus, the current flow will be blocked by one of the junctions and a very high resistance is expected in its initial state.

When a positive voltage pulse is applied on the top electrode (Pt), oxygen vacancies, which have been uniformly distributed throughout the BCFO layer, start to move toward J2 and accumulate near this junction (Figure 3.4c). Now, BCFO near J2 changes to an n-type semiconductor due to the increased oxygen vacancy concentration, which can lower the barrier height of J2 (Band diagram in Figure 3.4c). By removing the oxygen vacancies near J1, J1 is expected to become an Ohmic contact because BCFO turns into highly doped p-type semiconductor near J1, which enables tunneling through a narrow depletion layer (Figure 3.4c) [79]. As a result, the device switches to the ON-state and behaves like a p-n diode.

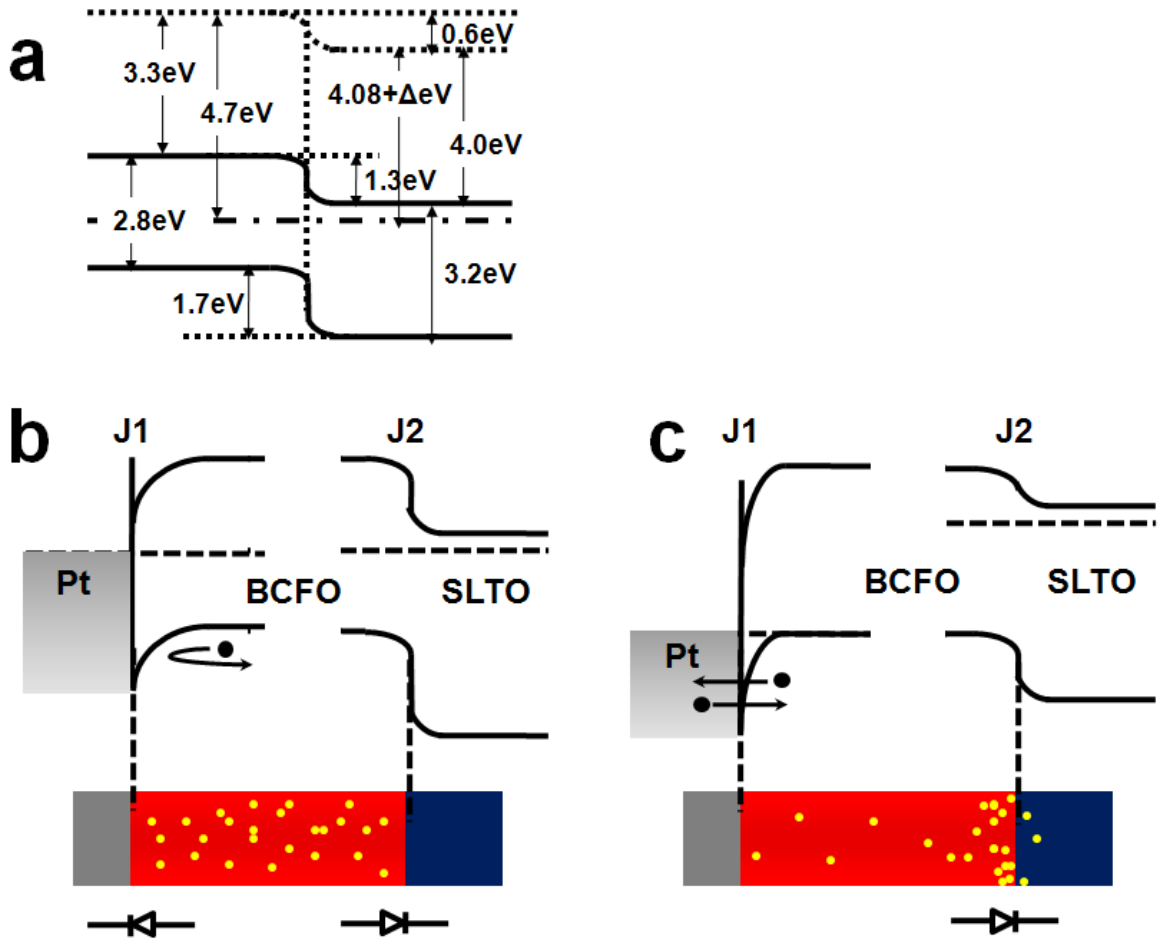

Figure 3.4: a Band diagram of BCFO/SLTO hetero-junction. **b**, **c** Schematic diagrams of the hetero-junction with the oxygen vacancy distribution and corresponding band diagrams. **b** Initial and OFF-state. **c** ON-state. The black and the yellow solid dots represent holes and oxygen vacancies, respectively. The junction properties are represented by a diode symbol with directions as shown.

On the contrary, a negative voltage pulse forces oxygen vacancies to move toward J1, however, the effect of the oxygen vacancy movement is different from the positive pulse case because the voltage drop across the device is different depending on the bias polarity on the top electrode (Pt) due to the asymmetric structure of this device. In previous chapter, it has been already observed that *I-V* hysteresis curves are different between the Pt/BCFO/SRO and SRO/BCFO/SRO structures. The former shows asymmetric *I-V* curves, whereas the latter shows symmetric ones. When a positive voltage applies on the top electrode the top electrode/BCFO junction is in reverse bias, BCFO layer is in high resistance state and BCFO/SLTO junction is in forward bias. So the voltage drop mostly occurs through top electrode/BCFO and BCFO layer. In detail, the top electrode/BCFO junction turns into an Ohmic contact after removing oxygen vacancies from this junction and then the most electric field applies to the BCFO layer. This enables oxygen vacancies to be effectively removed from the top electrode/BCFO junction and to move to the BCFO/SLTO junction.

On the other hand, in case of applying negative bias on top electrode the top electrode/BCFO is in an Ohmic contact (or forward bias), BCFO is in low resistance state and BCFO/SLTO junction is in reverse bias. As a result, the most voltage drop is expected to occur across J2 and the electric field felt by oxygen vacancies is less than that of the positive bias case. That means the oxygen vacancy concentration near J1 is increased but not high enough to invert the layer to n-type. Instead, it can turn into a slightly doped p-type semiconductor which enlarges the depletion width and leads to the formation of a Schottky barrier (Figure 3.4b). Similar to the initial state, J1 has the opposite forward bias polarity as J2, which switches the ON to the OFF state. Consequently, reversible resistance switching is expected by altering the J1 energy barrier height while maintaining rectifying behavior by J2 in the hetero-junction diode.

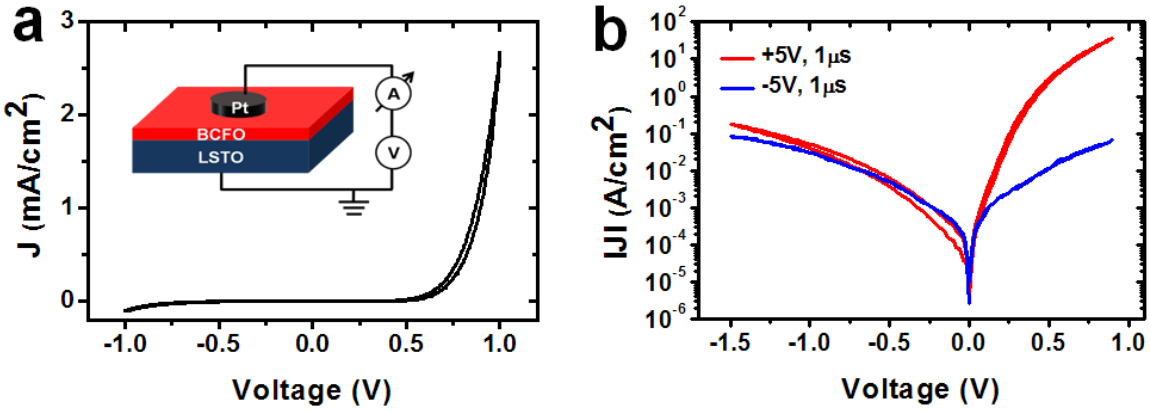

Figure 3.5: Resistance transition of Pt/BCFO/SLTO hetero-junction. a The initial *I-V* curve of the hetero-junction. Inset: The schematic device structure of Pt (20μm in diameter)/$Bi_{0.9}Ca_{0.1}FeO_{3-\delta}$ (20nm thickness)/La doped $SrTiO_3$ hetero-junction. **b** Bipolar, reversible 'ON' (low resistance state) and 'OFF' (high resistance state) switching behavior.

Chapter 3.2 Electrical Characteristics of BCFO/SLTO Hetero-Junction Device

Based on this design concept, Pt/$Bi_{1-x}Ca_xFeO_{3-\delta}$/$SrLaTiO_3$ hetero-structures were fabricated and their electrical characteristics were evaluated. BCFO thin films with x=0.1 were chosen because the films with this Ca concentration showed the largest conduction modulation as shown in Chapter 2.

Chapter 3.2.1 Rectifying Resistive Switching Behavior

The initial *I-V* curve of the device exhibits rectifying characteristics (Figure 3.5a). The inset in Figure 3.5a represents the schematic device structure and *I-V* measurement set-up. By applying positive and negative electric fields, non-volatile and reversible transitions between ON and OFF-states have been observed while maintaining the rectifying behavior for the Pt/BCFO/SLTO hetero-structure (Figure 3.5b). The ON/OFF and the forward and reverse conduction ratios are larger than 10^2 and 10^3, respectively. After applying 5V for 1µs, the device switches to the highly conductive, low resistance ON-state and a consecutive -5V, 1µs pulse makes it less conductive, thus returning to the high resistance OFF-state (Figure 3.5b). The minimum voltage required for switching to the ON-state is very consistent but the switching voltage to the OFF-state shows some variation from electrode to electrode and sample to sample (-3V ~ -7V). Stable resistance switching also depends on the pulse width. A higher switching voltage and a larger pulse width result in early breakdown in endurance testing. Therefore, I use electrodes which show good switching characteristics at a moderate switching voltage of ±5V. The conventional forming process [70] is not necessary for this device and the first switching to the ON or OFF-state from the initial state depends on the first pulse polarity. If a negative pulse is applied first the device switches to the OFF-state and a subsequently applied positive pulse

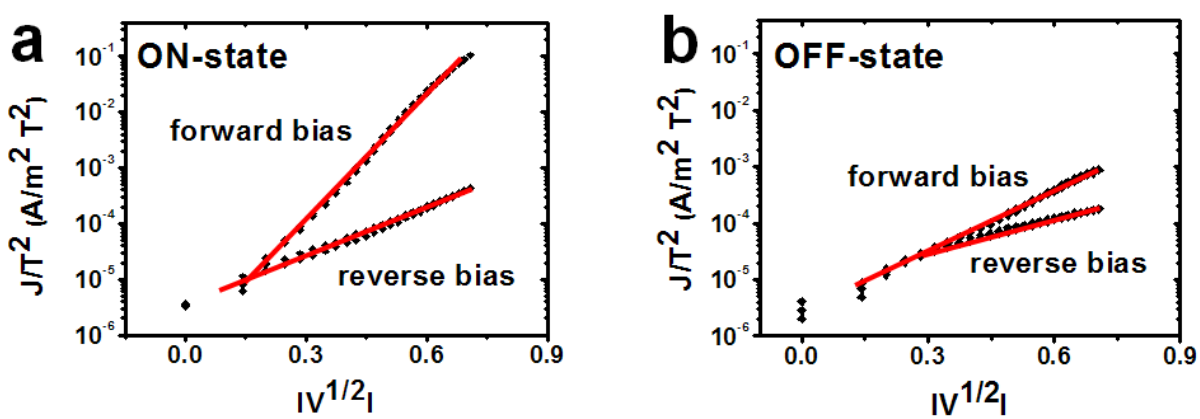

Figure 3.6: Analysis of *I-V* curve. a, b Schottky emission, $J_S/T^2 \alpha\ exp[V^{1/2}]$. **a, b** represent ON-state and OFF-state *I-V* curves, respectively.

sets it ON. After that, the device works between these two states and it never returns to the highly insulating initial state. The polarity dependent switching shows a bipolar characteristic. Furthermore, the resistance switching with rectified behavior and the positive forward bias coincide with the expectations.

Chapter 3.2.2 Transport Models for the Hetero-Junction

In order to investigate the switching mechanism, typical *I-V* curves of ON and OFF states are re-plotted as different functions of the applied voltage. By fitting the *I-V* data to possible transport models commonly found in oxides such as Schottky emission, space charge limited conduction (SCLC) and Poole-Frankel emission (PF emission), insight into the nature of the current flow can be determined to be either interface (Schottky emission) or bulk-limited conduction (SCLC, PF emission) [80].

The interface-limited Schottky emission arises from a difference in Fermi levels between a metal and an insulator or semiconductor contacts. The energy difference creates a potential barrier between the metal and insulator that charges must overcome. The current density across a Schottky barrier is represented by

$$J_S = AT^2 \exp - \left[\frac{\Phi}{k_B T} - \frac{1}{k_B T} \left(\frac{q^3 V}{4\pi\varepsilon_0 K d} \right)^{1/2} \right],$$

where A is the Richardson constant, Φ is the height of the Schottky barrier, K is the dielectric constant of the film, and d is the sample thickness.

The bulk-limited space-charge-limited conduction (SCLC) arises from a current impeding space charge forming as charges are injected into the film from the electrode at a rate faster than they can travel through the film. The current density for SCLC is

$$J_{\mathrm{SCLC}} = \frac{9\mu\varepsilon_0 K}{8} \frac{V^2}{d^3},$$

where μ is carrier mobility.

The last mechanism is bulk-limited Poole-Frenkel emission. This conduction mechanism involves the consecutive hopping of charges between defect trap centers. The ionization of the trap charges can be both thermally and field activated. The conductivity for Poole-Frenkel emission is

$$\sigma_{\mathrm{PF}} = c \exp - \left[\frac{E_1}{k_B T} - \frac{1}{k_B T} \left(\frac{q^3 V}{\pi\varepsilon_0 K d} \right)^{1/2} \right],$$

where c is a constant and E_1 is the trap ionization energy.

For these devices only a Schottky barrier model shows a linear fit to the ON and OFF-state *I-V* curves (Figure 3.6a and 3.6b, respectively) but SCLC and PF emission do not match the straight line fit (Figure 3.7). The results suggest that the conduction is dominantly controlled by interface-limited conduction, not bulk-limited conduction.

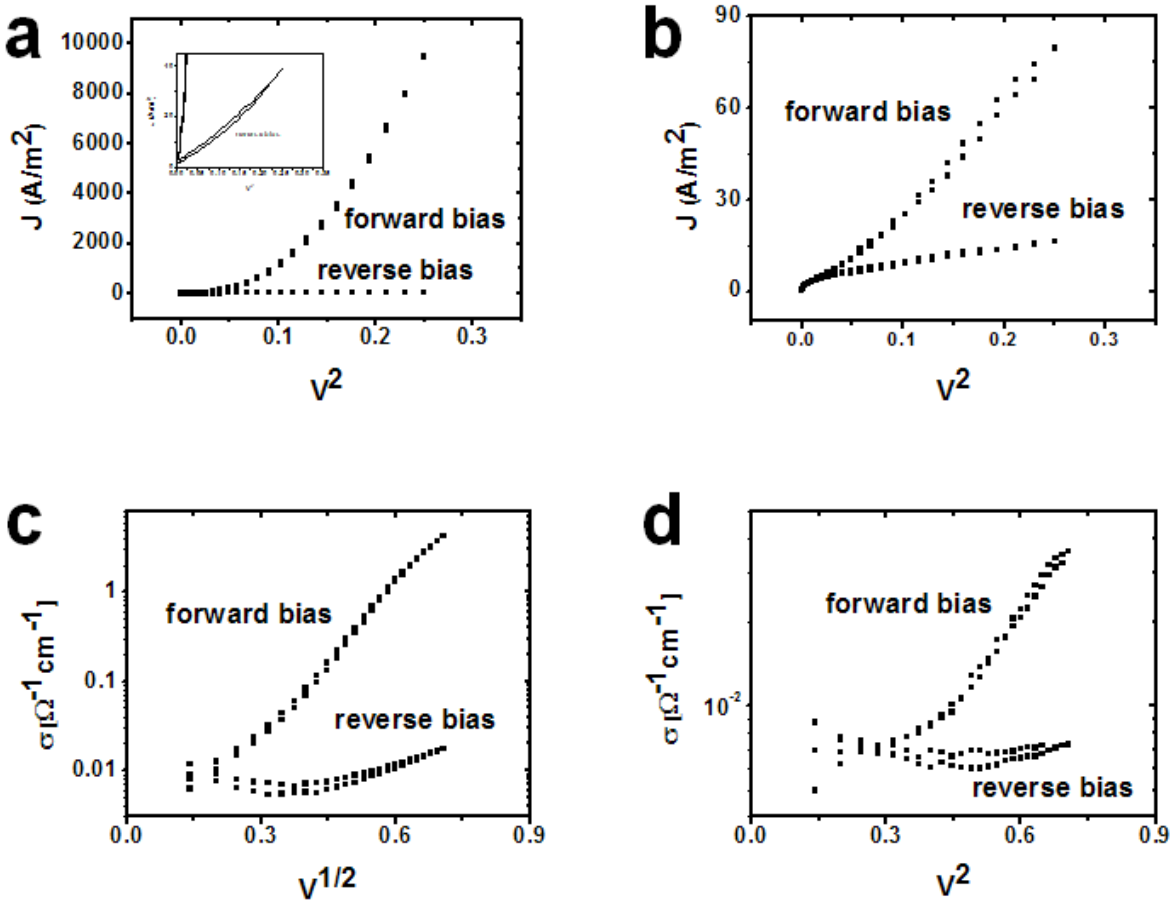

Figure 3.7: Analysis of *I-V* curve. a, b space charge limited conduction for ON and OFF state, respectively. **c, d** Poole-Frankel emission for ON and OFF state, respectively.

Chapter 3.2.3 Dependence of Resistive Switching on Electrode

In order to evaluate which interfaces are responsible for the resistance switching behavior, the Pt top electrodes were changed to a conductive oxide, $SrRuO_3$ (SRO). Interestingly, in this case significant resistance switching has not been observed even with much higher and longer electric pulses than those used for Pt top electrode devices. Figure 3.8a indicates that SRO/BCFO/SLTO hetero-junctions are highly conductive at the initial state and the *I-V* curve is similar to the ON-state of Pt top electrode devices but shows a larger leakage current, which can be explained by trap assisted tunneling [81]. The earlier turn-on for Pt top electrode devices is due to the barrier height reduction as mentioned in the design concept (Figure 3.4c). The highly conductive state of the SRO top electrode device can be understood by looking at the difference of the contact energy barrier. For SRO electrodes, the epitaxial films are grown on BCFO thin films sequentially without breaking vacuum so it is expected that only a small amount of

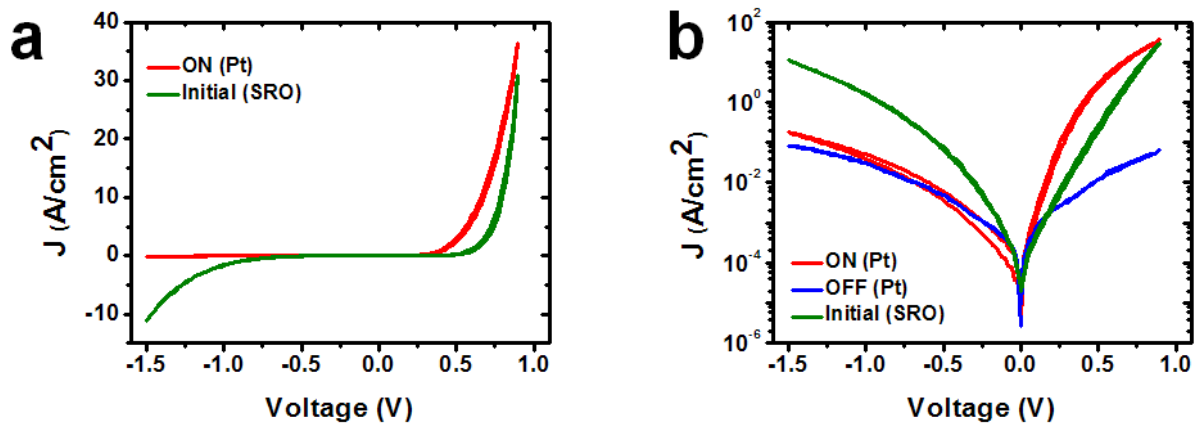

Figure 3.8: a *I-V* curves of hetero-junctions with Pt (red line) and SRO top electrode (green line) in linear scale. **b** Comparison of *I-V* curve characteristics of ON (red line) and OFF (blue line) state of Pt top electrode and initial state (green line) of SRO top electrode.

interfacial states are created in this junction, which results in Ohmic contact for SRO/BCFO junctions based on the work-function difference. Therefore, the current flow is mostly controlled by the BCFO/SLTO (J2) p-n junction, resulting in the diode-like characteristic in its initial state.

In addition, the *I-V* curve of SRO/BCFO/SLTO shows a very linear forward current in a semi-log plot (Figure 3.8b), which suggests that J2 acts like an ideal diode. This reveals that the resistance switching behavior is mainly attributed to the junction between top electrode and BCFO as expected in the device design.

Chapter 3.2.4 Dependence on Voltage Sweep Rate

Now it is considered how the junction properties can be altered by electric fields. As shown in Figure 3.9, the conductivity changes are strongly dependent on the sweep rate of the applied voltage. As the sweep rate decreases, the turn-on voltage, at which the current increases rapidly, shifts to lower values and the conductivity is increased. The same tendencies were observed in BCFO samples of different thickness and are summarized in Figure 3.9d. The sweep frequency dependence of oxide thin films can be well described with the model of memristic behavior and is a strong evidence of ionic movements that are responsible for the conductivity changes [82]. Assuming that oxygen vacancies are the only mobile ions, the local change of the oxygen vacancy concentration from the equilibrium value can generate electrons or holes to satisfy the charge neutrality [83]. The slower sweep rate gives oxygen vacancies more time to move, which results in larger deviations of the local oxygen vacancy concentration from the equilibrium value. According to the charge neutrality equation of Ca doped $BiFeO_3$, the oxygen vacancy rich area turns into an n-type semiconductor and the oxygen vacancy deficient area turns into a p-type semiconductor by generating electrons and holes, respectively. This can be described by

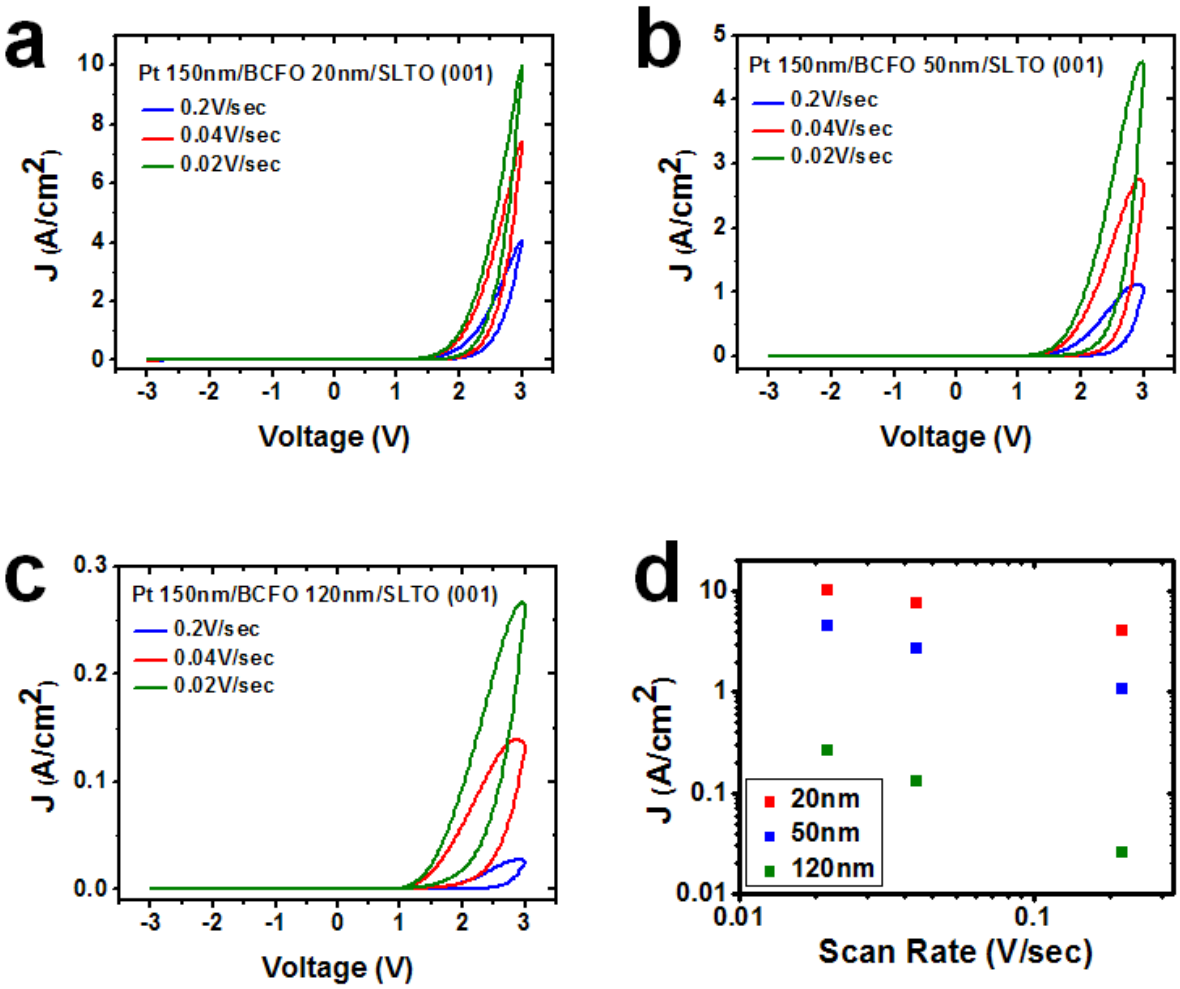

Figure 3.9: Effect of voltage sweep rate on conduction.
a 20nm **b** 50nm **c** 120nm thickness BCFO and SLTO hetero-junctions with Pt top electrodes. The I-V measurements were done for each sample with varying the voltage sweeping rate, 0.2V/sec (blue line), 0.04V/sec (red line), 0.02V/sec (green line). **d** The current density read at 3V as a function of sweeping rate for different thickness of BCFO samples.

$$2[V_O^{\bullet\bullet}] - [Ca_{Bi}^{'}] + [h^{\bullet}] - [e^{'}] = 0$$

where $[V_O^{\bullet\bullet}]$, $[Ca_{Bi}^{'}]$, $[h^{\bullet}]$, and $[e^{'}]$ indicate the concentration of oxygen vacancies, calcium ions, holes and electrons, respectively. Therefore, the changes of local oxygen vacancy concentrations by an applied electric field, modifies the electric properties of the junctions and the bulk material. This is very well matched with the results in chapter 2.

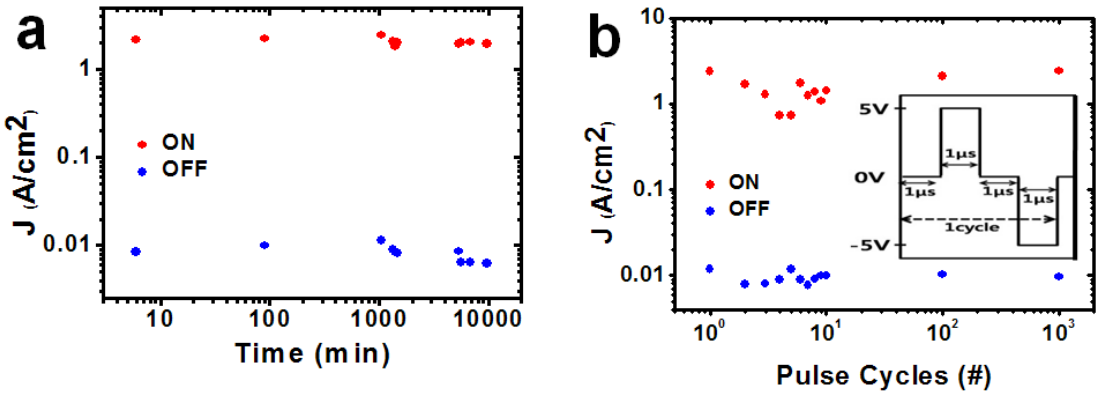

Figure 3.10: Characteristics of long time reliability.
a Retention time was measured after switching to the ON and OFF state at room temperature. The current density was read at 0.5V as a function of elapsed time. **b** Endurance of the device was performed by applying positive and negative pulses repeatedly. Inset: Schematic diagram of one pulse cycle.

Chapter 3.3 Robustness of the Device

The robustness of our devices was evaluated by analyzing data retention time and device endurance. The test results demonstrate the prospectively good memory device performance. As shown in Figure 3.10a, the current densities of ON and OFF states at 0.5V maintain almost the same value at least for a week. No significant changes of current density were observed at each state for the testing duration. Also, the endurance of the devices was tested by applying positive and negative pulses repeatedly (Figure 3.10b). The inset of Figure 3.10b schematically shows the wave form of a pulse cycle which consists of 1μs waiting at 0V, +5V pulse for 1μs, 1μs waiting at 0V, and -5V pulse for 1μs.

After the pulse cycles, the ON and OFF current was measured at 0.5V after applying +5V, 1μs and -5V, 1μs, respectively. Figure 3.10b shows the ON and OFF switching persists up to 10^3 cycles. The devices undergo breakdown or degradation with higher current flows (10^2~10^3 times higher than those of ON state) and reduced ON/OFF ratio (below 10) after ~10^3 cycles. The device thus performs not as good as current nonvolatile Flash memory devices in endurance characteristic (~10^6 cycles) but the endurance of the device strongly depends on the whole waveform of a pulse cycle. An enhancement of endurance characteristic was observed as the waiting time between a positive and a negative pulse was increased. Therefore, it is necessary to understand the degradation mechanism of this device to improve its endurance characteristics.

Chapter 3.4 Conclusions

Pt/BCFO/SLTO hetero-junctions show nonvolatile resistance transitions with a good

rectifying characteristic at their low resistance state. This is very critical to realize random access memory devices with simple cross point cell structure. The switching mechanism is elucidated by junction property modification ascribed to the change of local oxygen vacancy concentration.

Chapter 4 Memory Device Application II: Optical Memory Device with a Ca-Doped $BiFeO_3$

In this chapter, the unique optical characteristics of a Ca doped BFO for a potential optical memory device application is introduced. The visual shade changes in BCFO with applied electric fields can generate two different bit information states which can be read by optical measurements. The planar electrode structures with poling BCFO films are used to observe the shade changes through the optical microscope with monochromatic light sources. Detailed absorption measurements, transmission electron microscopy, and c-AFM method for a local area poling were used to investigate the origin of this optical characteristics.

Chapter 4.1 Introduction to Optical Memory Devices

Optical memory devices usually indicate devices that can write or read bit information optically. A Compact disc (CD) or a digital video disc (DVD) is the most famous and familiar optical memory device. Basically, there are three types of optical storage, read-only, write-once and reversible [84]. Read-only devices are typically used for publishing applications requiring dissemination of large amounts of data, since the data can be replicated on a disk at low cost. CD-ROM (Compact disc-Read Only Memory) is a representative read-only memory. Write-once media (e.g. CD-R; Compact Disc-Recordable) are used in applications that have large backup or archiving requirements. Reversible media (e.g. CD-RW; Compact Disc-ReWritable) is typically used in applications that need large amounts of temporary storage, and can take advantage of removable media.

The optical setup for CD-ROM in the reading operation is based on the interference of the light reflected from a series of tiny indentations known as "pits" and the land (areas between pits). The discs are fabricated such that the light reflected from the land has traveled half a wavelength more than that from the pits and therefore destructively interferes producing no reflection from the pits. The standard design for optical systems incorporates a laser diode operating at an appropriate wavelength for reading a CD-ROM [84, 85]. CD-Rs use an additional photosensitive dye which is coated on a blank CD-ROM. The write laser changes the color of the dye to allow the read laser to see the difference. On the other hand, CD-RW uses a metallic alloy (AgInSbTe) which is amenable to a phase change (polycrystalline ↔ amorphous) by laser heating [86, 87]. The change of reflectivity between these two phases makes bit information.

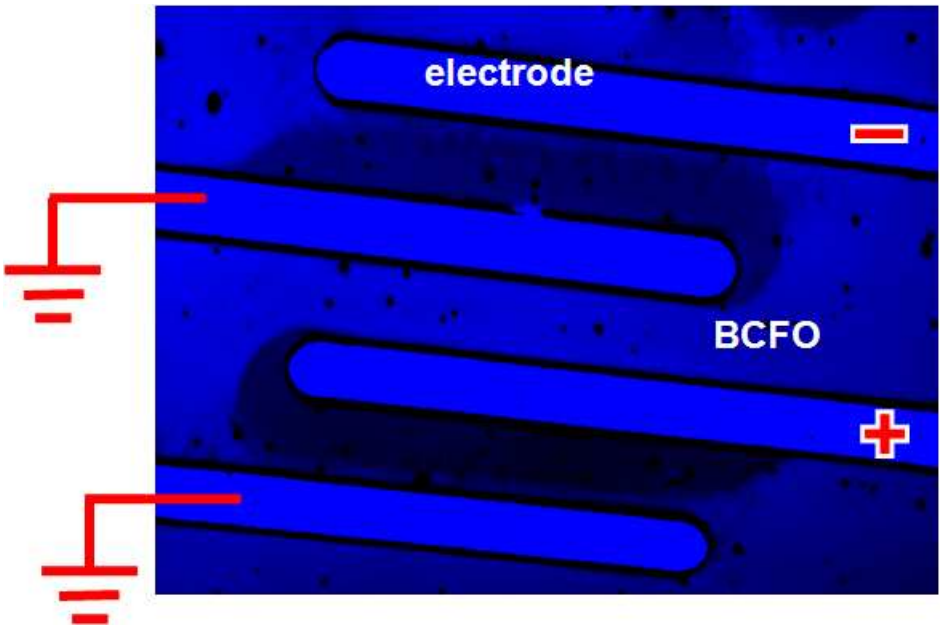

Figure 4.1: Poled areas between in-plane electrodes showing optical contrast.

Other types of optical memory devices such as magneto-optical disc storage [88], holographic storage [89-91], and 3D-bit optical data storage [92, 93] have been proposed and developed to increase memory capability. In the following chapter, the electric-field-driven optical memory effect of BCFO is discussed in detail for potential memory device applications.

Chapter 4.2 Electric-Field-Driven Change of Optical Characteristics in BCFO

Chapter 4.2.1 Electro-Optic Effect in BCFO

The electro-optic memory devices which can electrically write and optically read bit information have been proposed by using transition metals, ferroelectric oxides, or chalcogenide alloys [94-99]. This type of device utilizes the change of optical properties such as refractivity, reflectivity, and absorptiveness by electric pulses for storing bit information states.

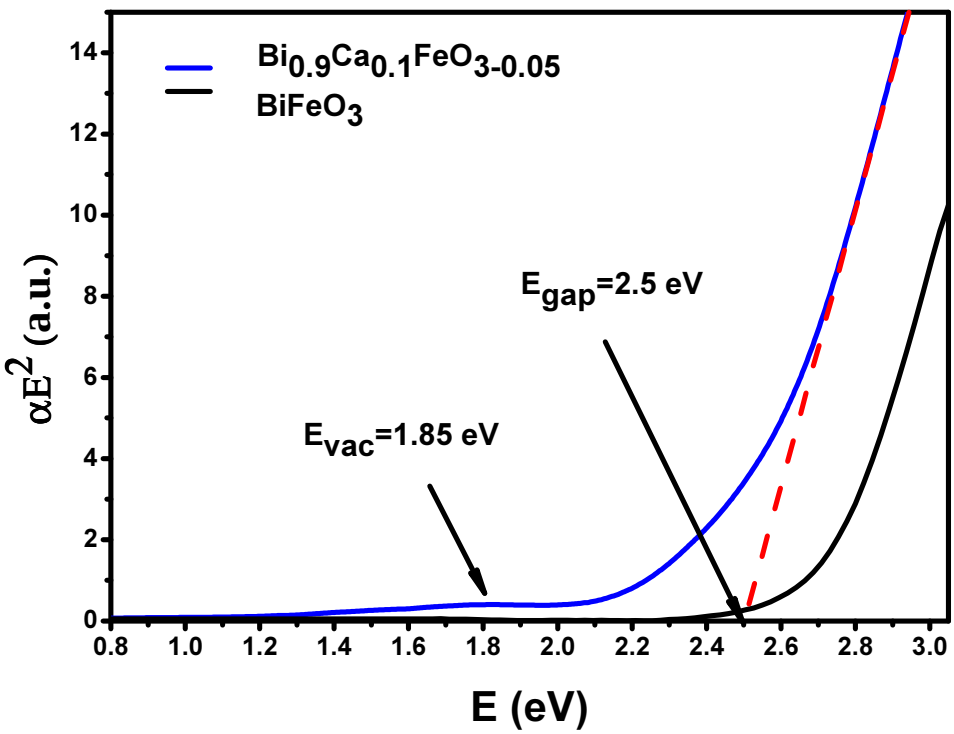

Figure 4.2: Optical absorption measurements for pure BFO and BCFO thin films. Optical bandgap E_g=2.5 eV of BCFO (10% Ca doping) evaluated from absorption measurement.

This interesting property was observed when the planar electrode structures were undergoing the poling process by optical microscope. Figure 4.1 shows that dark shades appear in p-type regions of the BCFO thin film. The image was taken with an optical microscope at room temperature using a monochromatic light source with a wavelength of 688 nm. The planar electrode structure and the poling processe for this figure are described in Figure 2.18. The dark shade area covering the space between two electrodes over ~90% corresponds to the highly conductive region from the c-AFM studies (see Figure 2.19 in chapter 2). The current profiles with c-AFM measurements (Figure 2.19b) are well matched to this dark shade distribution. The dark shades disappear after annealing at 250 °C for 1 hour in air. This is due to an increase in diffusivity of the oxygen vacancies allowing them to spread throughout the material back to their equilibrium.

These experimental observations imply that the phenomena of the appearance and the disappearance of dark shades are related to the oxygen vacancy distribution which is driving force for the resistive switching of a BCFO. Therefore, the shade effect is also another experimental evidence supporting the established resistive switching mechanism of BCFO.

Chapter 4.2.2 Optical Band Gap for BCFO

Macroscopic optical absorption measurements were performed for BFO and BCFO thin films. A plot of αE^2 *vs*. photon energy (E) and the linear extrapolation to $\alpha E^2 = 0$ indicates a direct gap at 2.5eV for $Bi_{0.9}Ca_{0.1}FeO_{3-\delta}$ (Figure 4.2a). This value is in slightly lower than that obtained for pure $BiFeO_3$ from optical measurements [100]. An additional absorption band originating from oxygen vacancies is observed around E_{vac}=1.85 eV.

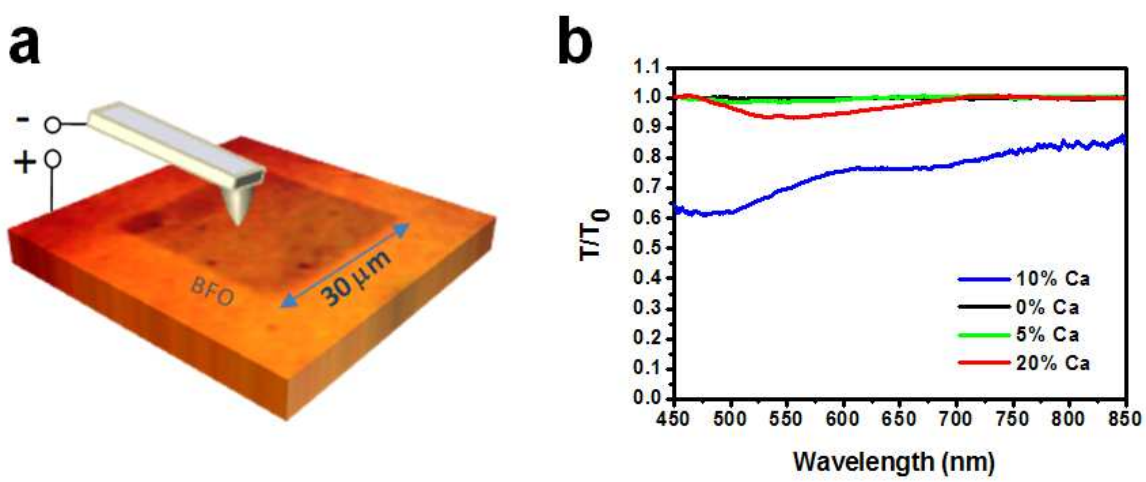

Figure 4.3: a Schematic diagram of c-AFM poling of the sample at -12V, and optical microscope image of a 30 μm^2 poled region in a 100 nm thick film. **b** Transmission change versus wavelength for different Ca doping levels.

Chapter 4.2.3 Dependence of Ca doping ratio on the Shade Effect

In order to investigate the origin of the electro-optic effect, local optical absorption measurements were performed for BCFO thin films with different Ca doping ratio before and after poling. BCFO thin films of 100 nm thickness were grown epitaxially on STO substrates via the PLD method with and without SRO bottom electrodes. A home-built optical setup was used for the measurements. A white light source (tungsten lamp) and a VIS-NIR spectrometer (Ocean-Optics USB400) for local optical absorption spectroscopy were used. Objective lenses were utilized to obtain a beam spot size of less than 20 μm when focused onto the sample. Micrometer-sized regions of the Ca-doped BFO thin films were poled using the c-AFM. Several 30μm×30μm boxes were poled with a bias of -12V and tip velocity of 3μm/sec while the current of the region was monitored. Poling was stopped when the current reached ~1μA. A CCD camera attached to the aforementioned optical setup was sufficient in finding the poled boxes to align for absorption spectroscopy. The spectra were analyzed at various spots outside the written boxes and compared to that of inside the box.

Figure 4.3a the visible change of the sample surface as seen through a microscope after c-AFM poling. This method produced rather consistent results, and visible spectra data was acquired. Furthermore, annealing the samples at 150 °C for 4 h caused the boxes to visibly disappear completely as observed in the planar electrode structure. The shading effect is quantified by the transmission changes of BCFO thin films. Figure 4.3b shows the transmission changes of BCFO thin films with various Ca concentrations after poling of the material as a function of wavelength. The reference spectrum is taken to be the transmittance of the region of the BCFO film outside of the electrically poled box. The minimum transmission for 10% Ca doping occurs at 2.55eV (485 nm), which is approximately the band gap, E_g, of BCFO. The change in visible transmittance spectra at this wavelength is 40%. Additionally, there is a small minimum at about 670 nm (1.85eV), which is associated with oxygen vacancies in the sample.

Interestingly, BCFO thin films with 10% Ca concentration show much larger shading effect than that of BCFO films with 20% Ca concentration. Considering that the shading effect is related to oxygen vacancies and their distribution, it is intuitively expected the opposite to be the case. I will discuss this deviation in the following chapter.

Chapter 4.3 Origin of the Shading Effect

Chapter 4.3.1 Effect of the Oxygen Vacancy Ordering

It is obvious that appearance of the dark shade is strongly related to the conduction modulation in BCFO. The dark shade distribution in planar electrode structures and the shading effect with respect to the Ca doping ratio coincide with the local current profiles (in Figure 2.19) and the largest conduction modulation for 10% Ca doping (in Figure 2.8c), respectively. Considering high carrier density in the dark shade area (p-type region), a surface scattering by charged particles might be a reason for such a shade appearance. However, the image in Figure 4.1 was obtained in reflective mode of the optical microscope; thus the shade results from real absorption.

If only the absolute amount of oxygen vacancies present determined the effect, it is readily expected that the shading effect can be increased as the calcium concentration is increased.

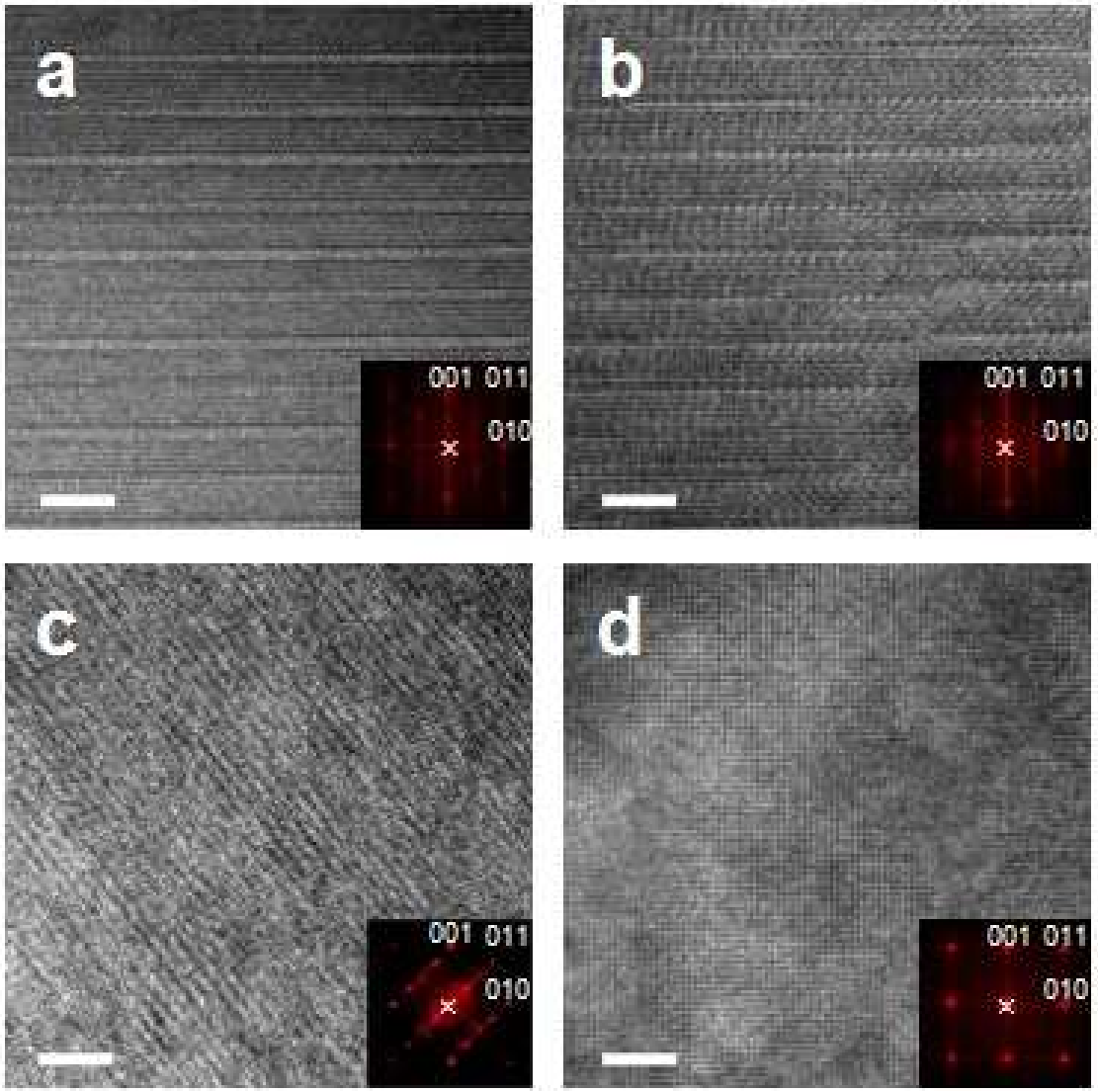

Figure 4.4: TEM characterization of the oxygen vacancy ordering in Ca-doped BFO.
a TEM image for as-grown state of 20% Ca-doped BFO. **b** TEM image after poling of 20% Ca-doped BFO. **c** TEM image for as-grown state of 10% Ca-doped BFO. **d** TEM image after poling of 10% Ca-doped BFO. Scale bars are 5 nm, insets show local diffraction patterns.

However, as the conduction modulation in Figure 2.7d, the 10% calcium-doped BFO shows larger absorption changes than that of 20% calcium-doped one (Figure 4.3b). This means that there must be some microscopic difference in both samples that leads to the observed behavior.

In order to gain some more insight, high resolution transmission electron microscopy studies are performed for both 10 and 20% Ca-doped BFO samples in the as-grown and poled states.

The results are seen in Figure 4.4. Figure 4.4a shows the as-grown state of a sample containing 20% Ca. The oxygen vacancy order parallel to the sample surface with a period of 8 unit cells is seen. An image of the c-AFM poled state after application of -12V can be seen in Figure 4.4b. The application of an electric field does not yield changes in the oxygen vacancy ordering. The results for the same type of measurements for a sample containing 10% Ca are shown in Figure 4.4c and d. The as-grown state shows an oxygen vacancy ordering with a period of 2 to 3 unit cells under an angle of 45° to the sample surface. After the application of a bias of -12V in the c-AFM poling the oxygen vacancy ordering is completely melted. In this area the overall vacancy concentration is lowered after poling, whereby the area becomes p-type as aforementioned in Chapter 2 [101].

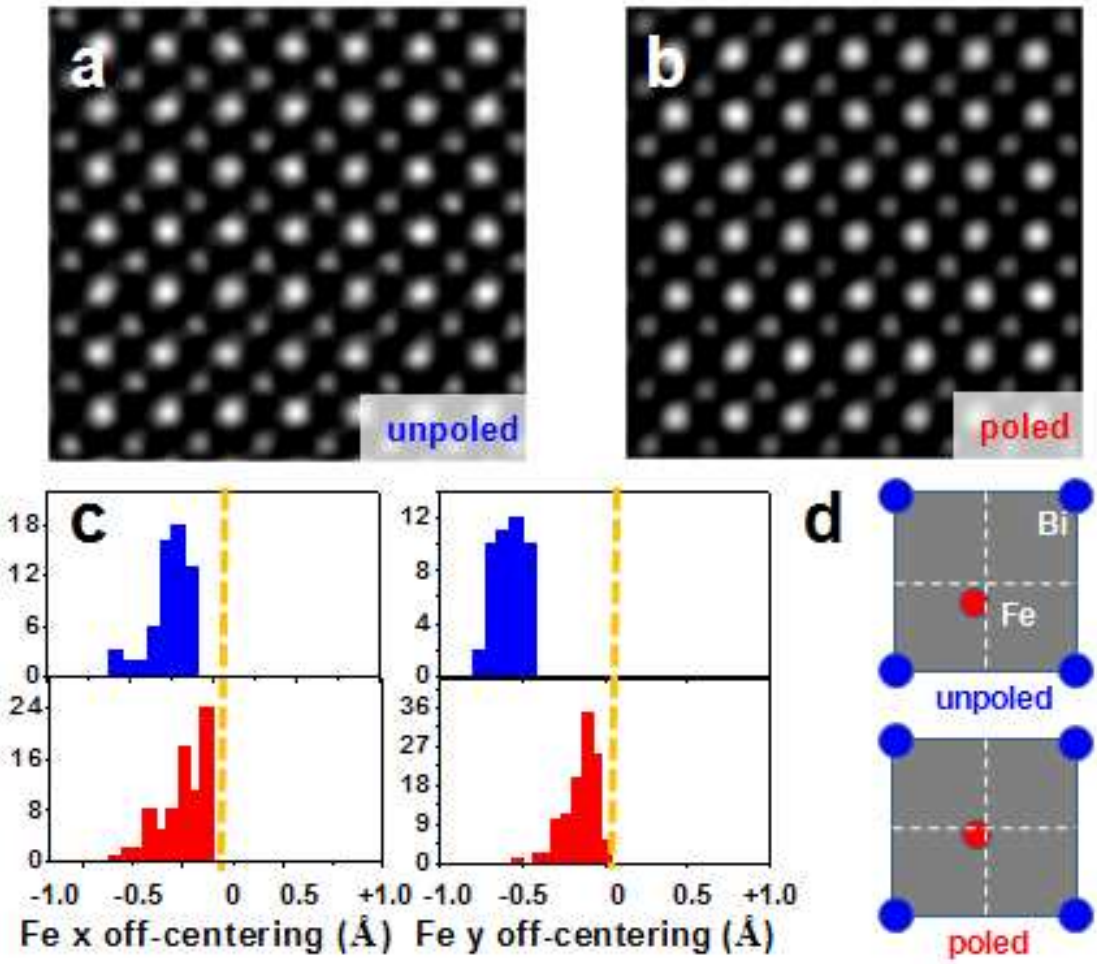

Figure 4.5: a, **b** High resolution TEM showing ion positions for poled and unpoled state for Ca 10%, **c** Histogram analysis of Fe ion position, **d** Schematic diagrams of Fe ion displacement using data of **c**.

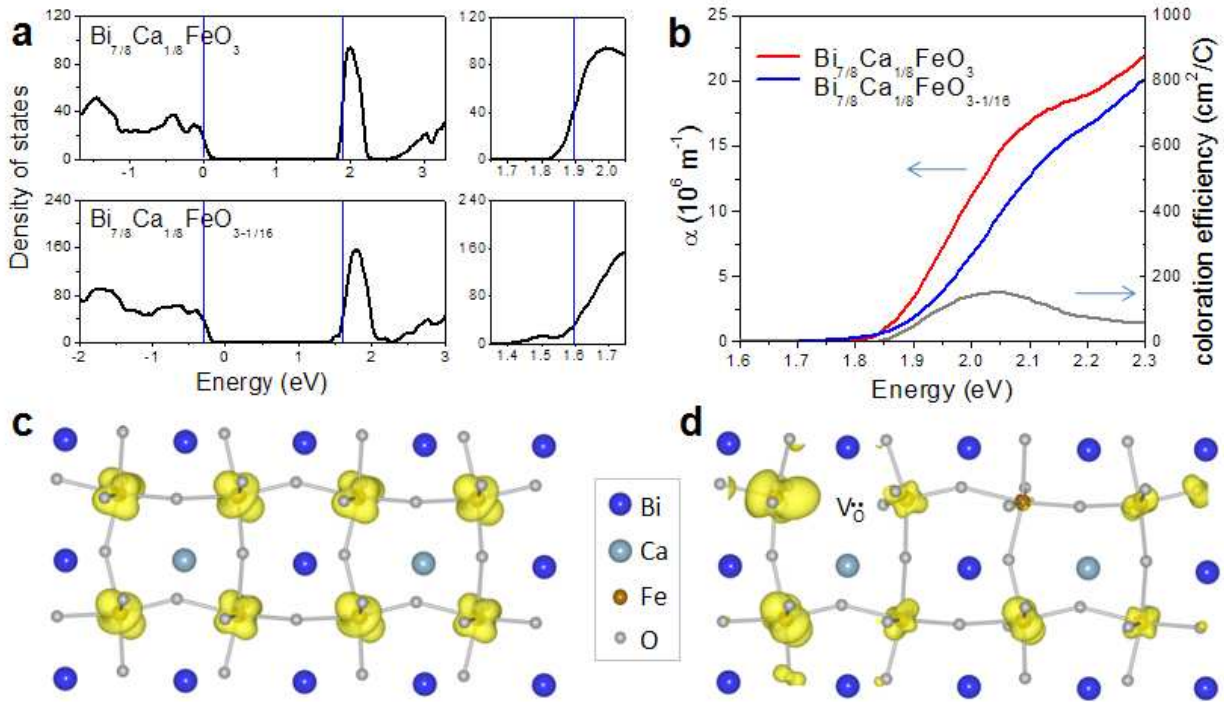

Figure 4.6: a Calculated electronic density-of-states near the band gap. **b** Optical absorption coefficients of $BiFeO_3$ as a function of photon energy. The calculations are performed using GGA+U method with U=4 eV and J=1 eV, for undoped $BiFeO_3$ (BFO), $BiFeO_3$ with calcium doping $Bi_{7/8}Ca_{1/8}FeO_3$, and $BiFeO_3$ with calcium doping and oxygen vacancy compensation $Ca_{1/8}Bi_{7/8}FeO_{3-1/16}$. **c, d** Isosurface electron density of the lowest lying conduction band states in uncompensated $Bi_{7/8}Ca_{1/8}FeO_3$ and in oxygen vacancy compensated $Ca_{1/8}Bi_{7/8}FeO_{3-1/16}$, respectively.

Considering that the oxygen vacancy redistribution by electric poling is the key factor for the resistive switching and the shading effect, these electrical and optical characteristics are dominantly influenced by the ionic conduction of oxygen vacancies. The ionic conduction of oxygen vacancies can be affected by the oxygen vacancy ordering. It has been reported that an abrupt change in the ionic conductivity at the order-disorder transition [102]. Because of the preferential conduction planes or directions in the oxide with ordered vacancies, the frequency prefactor in the oxygen ion diffusion coefficient must be smaller in the oxide with ordered vacancies than in the oxide with the random distribution of vacancies. Therefore, the ordered vacancies are indeed less favorable for ionic conduction [103]. In case of the BCFO, the ordered vacancy structure is maintained after poling for the 20% Ca-doped BFO, while the oxygen vacancy ordering is completely melted for the 10% Ca-doped BFO. The oxygen vacancy ordering reduces the ionic conduction of oxygen vacancies of 20% Ca-doped BFO, resulting in smaller shading effect than 10% Ca-doped BFO with disordered oxygen vacancies. Besides this

optical behavior, the larger conduction modulation in 10% Ca-doped BFO thin films than in 20% one can be understood by the difference of ionic conductivity of ordered and disordered vacancy structure.

Chapter 4.3.2 Effect of polar order parameter

A close inspection of the individual ion positions for the poled and unpoled state by high-resolution TEM is presented in Figure 4.5a and 4.5b. From these images Fe ion position coordinates are extracted as shown in Figure 4.5c. Histogram plots show that the average Fe off-centering is reduced for the poled state as compared to the unpoled state. A schematic representation can be seen in Figure 4.5d. In addition, at high temperature the measured bandgap of BFO decreases as the deviation from the cubic structure decreases [104, 105]. Both studies indicate that the optical properties of undoped BFO are sensitive to the polar order parameter and the structural symmetry. For BCFO, the shading effect in the electrically poled state is accompanied by a relative shift of the Fe ion with respect to the unit cell center also indicating a change of the polar order parameter.

In order to understand the effects of calcium doping and oxygen vacancies on the optical properties of $BiFeO_3$, for both the compensated and p-type case, we have also performed first-principles density-functional theory (DFT) [106, 107] calculations using approaches previously used for $BiFeO_3$ [108-113]. After the structural and electronic ground states have been determined, the frequency dependent real part ε_1 and imaginary part ε_2 of the dielectric function are calculated [114]. The usual expression for the optical absorption coefficient $\alpha(\omega)$ is,

$$\alpha(\omega) = \frac{\omega}{nc_0}\varepsilon_2(\omega)$$

where ω is the energy of the absorbed photon, n is the refractive index, and c_0 is the speed of light in vacuum. The optical absorption coefficient $\alpha(\omega)$ can also be expressed in terms of the real and imaginary parts of the dielectric function,

$$\alpha(\omega) = \frac{\sqrt{2}\omega}{c_0}\left[\sqrt{\varepsilon_1^2 + \varepsilon_2^2} - \varepsilon_1\right]^{1/2}.$$

The calculated electronic density-of-states and optical absorption coefficients of both the uncompensated and the compensated Ca-doped $BiFeO_3$ are shown in Figure 4.6a and b. It is well known that DFT calculations underestimate the band gap for most materials, and incorporation of onsite Coulomb interaction with Hubbard U parameter improves the band gap value. It has also been shown that oxygen vacancies play a role in the optical properties of $BiFeO_3$ [113]. With the specific choice of onsite Coulomb interaction parameters (U=4 eV, J=1 eV), the optical band gap is calculated to be 1.95 eV for undoped $BiFeO_3$. Assuming 1/8 of Ca doping and complete compensation of holes by oxygen vacancies ($Ca_{1/8}Bi_{7/8}FeO_{3-1/16}$ in Figure 4.6a), the optical band gap is reduced by 0.1 eV from the undoped material. This result is consistent with the experimental observations, which show that Ca doping reduces the band gap of $BiFeO_3$ from 2.7 eV to 2.5 eV. Because of the complete charge compensation, the Fermi level lies in the band

gap. Ca-doped BFO without charge compensation from oxygen vacancies shows a much sharper rise in the density-of-states of the conduction band, which results in an enhanced optical absorption near the band edge ($Ca_{1/8}Bi_{7/8}FeO_3$ in Figure 4.6a). The difference between the compensated and the uncompensated Ca-doped BFO in the density-of-states of the conduction bands becomes apparent by looking at the electron density of the lowest conduction states, as shown in Figure 4.6c and d. The lowest conduction states in uncompensated Ca-doped BFO are mostly extended Fe 3d states, similar to undoped BFO. In contrast, the lowest conduction states in compensated Ca-doped BFO localize at Fe sites near the compensating oxygen vacancies.

The defect-like localized states in compensated BCFO correspond to the small shoulder at the conduction band edge in the electronic density-of-states, resulting in the reduced density-of-states of the extended conduction band states just above it (bottom panel in Figure 4.6a) and the lower optical absorption coefficient near the band edge. At 1.95 eV, the difference in calculated absorption coefficient is 3.4×10^6 m^{-1}, which is in very good agreement with the measured change of 4.8×10^6 m^{-1} at 480 nm.

Chapter 4.3.3 Mechanism of the shading effect

The theoretical calculations and the TEM characterization point to the following mechanism of the shading effect in 10% Ca-doped BFO. In the as-grown sample, oxygen vacancies compensate the Ca dopants and form ordered structures. Upon application of an electric field, the vacancy ordering is melted, and vacancy-rich (n-type) and poor (p-type) regions are formed due to the resulting redistribution of vacancies. The dark shade originates from the increased optical absorption at the band edge of the p-type region. In contrast, oxygen vacancy ordering in 20% Ca-doped BFO remains almost unchanged under an electric field, which is consistent with the small change in absorption. DFT calculations were carried out with supercells containing uniformly distributed Ca dopants and oxygen vacancies. The effects of extended oxygen vacancies such as vacancy clusters or planes of ordered vacancies observed in other transition metal oxides have not been explored theoretically in the current study because of the high computational demand. However, a recent study has shown that oxygen vacancy clustering in $SrTiO_3$ induces localized states at 0.6 eV below the conduction band minimum [115], while the single vacancy states are much closer to the conduction band minimum. The observed weak absorption peak at 1.85 eV in our measurements could therefore also originate from clustering of oxygen vacancies.

Chapter 4.4 Conclusions

$Bi_{0.9}Ca_{0.1}FeO_{3-\delta}$ (Ca 10%) exhibits large absorption changes upon application of external electric fields. The films show a 40% change in visible transmittance spectra of the BCFO thin films at 480 nm wavelength (2.55eV). The absorption change increases with increasing the calcium concentration (i.e. with increasing the oxygen vacancy concentration) but the BCFO thin films with ordered oxygen vacancies shows a smaller absorption change due to the restriction of vacancy conduction. The origin of the dark shade is accompanied by a structural transition as seen in a change of Fe ion displacement. Furthermore, the observation of strong absorption change, that is achieved solely by redistribution of oxygen vacancies within the material itself by melting the vacancy ordered state should motivate a search for similar control in other related

complex oxide systems. This large absorption changes with electric fields can be used for potential electro-optic memory devices.

Chapter 5 Summary of Findings and Suggestions for Future Investigations

Chapter 5.1 Summary of Findings

Chapter 5.1.1 Summary of Chapter 1

Chapter 1 served as an introduction to the main themes of this dissertation. This chapter gave an introduction to new memory devices emerging as the alternatives to current memory devices. I began by discussing the demands on new memory devices in point of issues of scaling and the replacement of the current multi-chip solution to the single-chip solution. This was followed by a brief overview of the new types of memory devices such as FRAM, PRAM, and MRAM. Device structures, operation mechanisms, and issues of these devices were presented. I then focused on the Resistance-change Random Access Memory (RRAM). Detailed discussions of the basic characteristics, materials, cell structures and resistive switching mechanisms were presented for RRAM as the most promising candidate for a future memory device. I ended this section by discussing the prospects of RRAM devices. A brief outline for the organization of the dissertation and a brief summary of the chapters were given at the end of this introduction chapter.

Chapter 5.1.2 Summary of Chapter 2

Chapter 2 focused on the growth and characterization of a Ca-doped $BiFeO_3$ (BCFO). In this chapter the effect of divalent-ion-calcium doping on multiferroic $BiFeO_3$ thin films was investigated and a phase diagram was built by varying the doping concentration and temperature. The investigation revealed that a ferroelectric-paraelectric boundary exists in $Bi_{1-x}Ca_xFeO_{3-\delta}$ at doping levels of x~1/8, stabilizing a pseudo-tetragonal phase that has a relatively smaller volume than that expected from conventional Vegard's law. I demonstrated the quasi-nonvolatile and reversible modulation of electric conduction, accompanying the modulation of the ferroelectric state in Ca-doped $BiFeO_3$ (BCFO) films, using an electric field as the control parameter. Application of electric field could control and manipulate this electronic conductor-insulator transition to the extent that a p-n junction could be created, erased and inverted in this material. The mechanism of resistive switching in BCFO was discussed based on the interplay of ionic and electronic conduction as a consequence of the naturally produced oxygen vacancies that act as donor impurities to compensate calcium acceptors and maintain a highly stable Fe^{3+} valence state. This conductor-insulator transition could be understood in terms of the charge balance and the local charge unbalance between oxygen vacancy donor impurities and the calcium acceptors. Through the calculation of the drift velocity of oxygen vacancies, I argued that application of an electric field could be a promising route to effectively ‘sweep’ oxygen vacancies to one side of the device without a dielectric breakdown. I also investigated the local electric conductivity of these films, applying electric field along the in-plane directions to prove the proposed switching mechanism by using a c-AFM method and the results were consistent with the switching mechanism.

Chapter 5.1.3 Summary of Chapter 3

This chapter aimed to build a memory device with BCFO thin films. I began by bring up the difficulty of random accessibility of RRAM devices. The unipolar current flow characteristics of these devices lead to errors during the reading process. Therefore, a good rectifying characteristic at their low resistance (ON) state is critical. In order to solve this problem I proposed the design concept for creating new RRAM device with BCFO. The design concept also focused on maintaining the simple cross-point cell structure and fabrication simplicity. Based on the characteristics of BCFO discussed in Chapter 2, I combined BCFO with an n-type semiconductor, La doped $SrTiO_3$ (SLTO) and demonstrated a reversible resistance switching in Ca-doped $BiFeO_3$ (BCFO)/ La doped $SrTiO_3$ (SLTO) hetero-junction with Pt electrode. The electrical measurements showed the *I-V* curves maintained a diode-like shape even after transition from the high resistance (OFF) state to the low resistance (ON) state. The ON/OFF and the forward and reverse conduction ratios were larger than 10^2 and 10^3, respectively. By fitting the *I-V* data to possible transport models commonly found in oxides I determined that the conduction was dominantly controlled by interface-limited conduction, not bulk-limited conduction. In addition, the investigation of the electrode dependence and the effect of the voltage sweep rate revealed that the resistance switching was attributed to the metal/BCFO junction with keeping the rectifying behavior by BCFO/SLTO hetero-junction. The switching mechanism was elucidated by the modification of junction property with the effect of the local oxygen vacancy concentration changes. This result shed the light on using BFO for RRAM applications.

Chapter 5.1.4 Summary of Chapter 4

In this chapter the unique optical characteristics of a Ca-doped BFO (BCFO) for a potential optical memory device application was introduced. The visual shade changes in BCFO with applied electric fields generated two different bit information states which can be read by optical measurements. The planar electrode structures with poling BCFO films were used to observe the shade changes through the optical microscope with monochromatic light sources. Detailed absorption measurements, transmission electron microscopy, and c-AFM method for a local area poling were used to investigate the origin of this optical characteristics. $Bi_{0.9}Ca_{0.1}FeO_{3-\delta}$ (Ca 10%) exhibited large absorption changes upon application of external electric fields. I observed that the films showed a 40% change in visible transmittance spectra of the BCFO thin films at 480 nm wavelength (2.55eV). The absorption change increased with increasing the calcium concentration but the BCFO thin films with ordered oxygen vacancies showed a smaller absorption change due to the restriction of vacancy conduction. The origin of the dark shade was accompanied by a structural transition as seen in a change of Fe ion displacement. I argued that the strong absorption change was achieved solely by redistribution of oxygen vacancies within the material itself by melting the vacancy ordered state. This large absorption changes with electric fields can be used for potential electro-optic memory devices.

Chapter 5.1.5 Summary of Appendices

Appendix A covers the determination of the cell size of memory devices. **Appendix B**

introduces pulsed laser deposition (PLD) technique used for the film growth throughout this dissertation. Finally, **Appendix C** focuses on scanning probe microscopy, especially piezoresponse force microscopy (PFM), and how this can be used to probe ferroelectric state in materials.

5.2 Suggestions for Future Works

Although many great ideas and findings have been presented by this work, I suggest here a few important studies that should be undertaken. These include:

1. Further investigation of the dynamics of oxygen vacancy in oxides. I proved that the generation and redistribution of oxygen vacancies in BCFO was underlying cause for the observed conduction modulation behavior. However, there is still no direct experimental evidence of oxygen vacancy movement in BCFO films. Therefore, the efforts to find the direct evidence of the oxygen vacancy movement and quantify local concentration of oxygen vacancies should be very important topics to design actual devices and expect the performance of these kinds of devices.

2. Investigation of the influence of conductive state transitions on corresponding magnetic order. BFO is a well known multiferroic material at room temperature. Although I tried to observe magnetic response changes with respect to the conduction modulation, it was very difficult to find any changes mainly due to a very small transition area compared to a whole film. Groundbreaking ideas are needed to study this effect. This correlation is important not only for academic reasons but also for practical applications. Information which can be written and read magnetically and electrically can increase the degree of freedom for device design and possibly open a new device scheme.

3. Investigations of further doping in complex oxide systems. Many interesting materials phenomena such as the emergence of high-T_c superconductivity in the cuprates and colossal magnetoresistance in the mangnites arise out of a doping-driven competition between energetically similar ground states. In addition, appropriate doping of multiferroic materials could enhance both the magnetic and ferroelectric order of the material.

4. Further investigations of oxide hetero-junctions. Since the colossal magnetoresistance in manganites was observed, much attention has been focused on the fabrication of all-oxide perovskite structures and devices. The p-n junction has been widely used in semiconductor technology and the behavior of carriers is so well established for conventional semiconductors. However, it is believed that the band theory for p-n junctions would be difficult to apply to transition metal oxides due to the strong Coulomb repulsion among electrons [116]. Therefore, a theoretical and experimental progress for the oxide hetero-junction is necessary to build up all-oxide hetero-junction devices.

5. Investigation of the degradation mechanism of RRAM devices. Understanding the

degradation mechanism is critical as much as establishing the resistive switching mechanism of RRAM to commercialize this kind of device. The breakthrough of the robustness of RRAM is leaning on this study.

Appendix A – Memory Cell Size

In most cases, the memory cell size is given in units of f^2, where f is the minimum half pitch size of devices representing usually the metal line width or the design rule. For an example, unit cells of a DRAM consist of one transistor and one capacitor. As shown in Figure A.1a, the width of word lines (M1) and bit lines (M2) is $1f$; so the capacitor size is $6f^2$ ($3f \times 2f$, the blue rectangle box) and the whole cell size is $12f^2$ ($4f \times 3f$, the rectangle box drawn by a red dashed line) with including the space between capacitors. The cell size is determined by the size of a capacitor because capacitors which are much larger than a transistor occupy most area of unit cells. The current DRAMs are 6~8 f^2 in a cell size due to progresses of capacitor structures from 2D (planar type capacitors) to 3D (bar, trench or cylinder type capacitors) and developments of high-k dielectric materials [117-119]. On the other hand, NAND Flash memory devices are 4 f^2 in cell sizes because one transistor, itself, constitutes a memory cell. As NAND Flash memory devices, the cell size of RRAMs is also $4f^2$ with their simple cross-point cell configuration (Figure A.1b). The cell size, 4 f^2, is the physical minimum size but the latest Flash memory can store multi-bits in single unit cell; so the actual cell size can be less than 4 f^2.

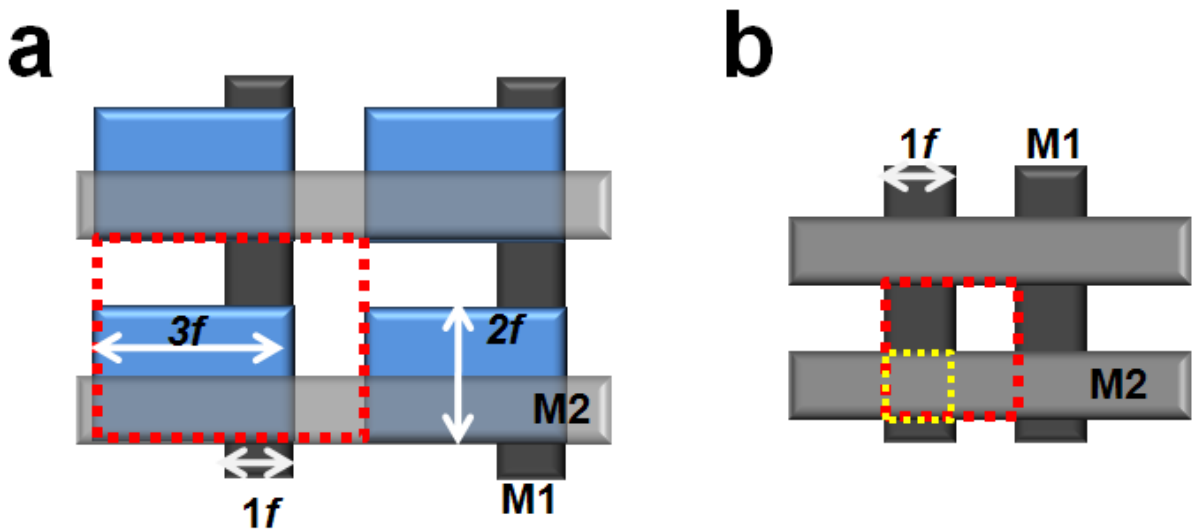

Figure A.1: Schematic diagram of 2×2 cell array a DRAM cell configuration. b Simple cross-point cell configuration. Red rectangle boxes (drawn by dashed line), blue boxes and the yellow box (drawn by dashed line) represent the unit cell area, capacitors in DRAM and active area of RRAM, respectively. The 'f' indicates the minimum half pitch. M1 and M2 are metal lines.

Appendix B – Pulsed Laser Deposition

Pulsed laser deposition (PLD) is a very simple thin film growth technique. PLD was first used by Smith and Turner [120] in 1965 for the preparation of semiconductors and dielectric thin films and was established due to the work of Dijkkamp and coworkers [121] on high-temperature superconductors in 1987. PLD emerged as an attractive technique for growth of thin films due to its important advantages: (1) the stoichiometric transfer of a complex composition from target to film and film crystallization at lower substrate temperature respect to other techniques due to the high energy of species in the laser plasma; (2) single step process, synthesis and deposition; (3) possibility of "in-situ" heterostructure deposition using a multi-target system, etc.

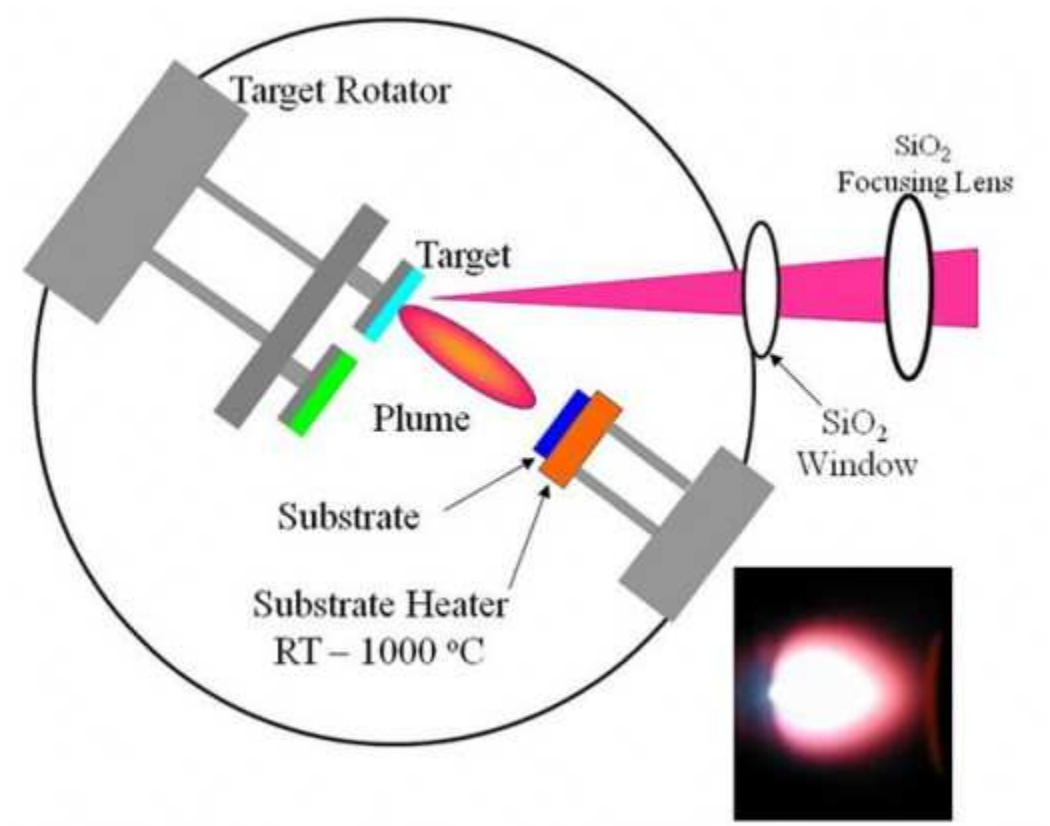

Figure A.2: Schematic diagram of a standard pulsed laser deposition system. The actual picture of the plasma plume is also shown [122].

With PLD method, thin films are grown by the ablation of one or more targets illuminated by a focused pulsed-laser beam. The system consists of a vacuum chamber equipped with pump, a target holder and rotator, and substrate heater. In a vacuum chamber, targets are struck at an angle of 45° by a pulsed and focused laser beam. The atoms and ions ablated from the target in a plasma plume are deposited on substrates. Mostly, the substrates are attached with the surface parallel to the target surface. In order to obtain different kinds of thin films, the films growth can be carried out in ultrahigh vacuum or reactive gas atmosphere, like that for oxides to fully oxygenate films. Temperature, oxygen partial pressure and laser energy density are important parameters [123, 124].

The laser used in this dissertation is a KrF excimer laser with wavelength 248nm. Depositions were completed at repetition rates between 1~20 Hz with energy densities around 2 Jcm^{-2}. Laser energies were measured using a Phir and Gentec-eo pyroelectric detector.

Appendix C – Piezoresponse Force Microscope

Piezoresponse force microscopy (PFM) is a branch of scanning probe microscopy (SPM). PFM is allows imaging and manipulation of polar materials on the nanoscale using a sharp conductive probe that scans the surface. Basic operation is based on the detection of surface deformation due to the reverse piezoelectric effect induced by the ac voltage applied to the tip.

The typical experimental setup for PFM includes a commercial microscope with conducting tip complemented with additional function generator and several lock-in amplifiers (Figure A.3). An ac modulation with an optional dc offset bias is applied to the conductive tip, which is in contact with the sample surface, and the piezoresponse of the sample is measured from the deflection of the cantilever. Once the cantilever is moved, the reflected laser beam tracks both vertical and horizontal displacements of the material reflecting piezoelectric deformations.

For the stress-free ferroelectric material homogeneously polarized in z-direction, the vertical displacement under applied voltage can be expressed by

$$\Delta z = d_{33}V + \frac{Q_{333}}{t}V^2$$

where V is the applied voltage, t is the sample thickness, d_{33} and Q_{333} are piezoelectric and electrostrictive coefficient, respectively.

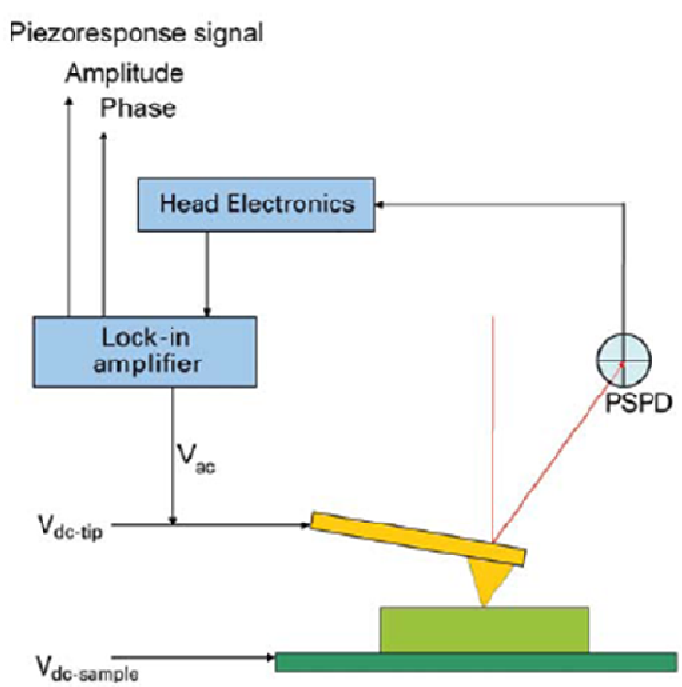

Figure A.3: Piezoresponse force microscopy experimental setup.

Under the external voltage $V_{tip} = V_{dc} + V_{ac}\cos\omega t$ the surface displacement is detected as the first harmonic component of the tip deflection. The phase of the electromechanical response of the surface yields information on the polarization direction below the tip [125].

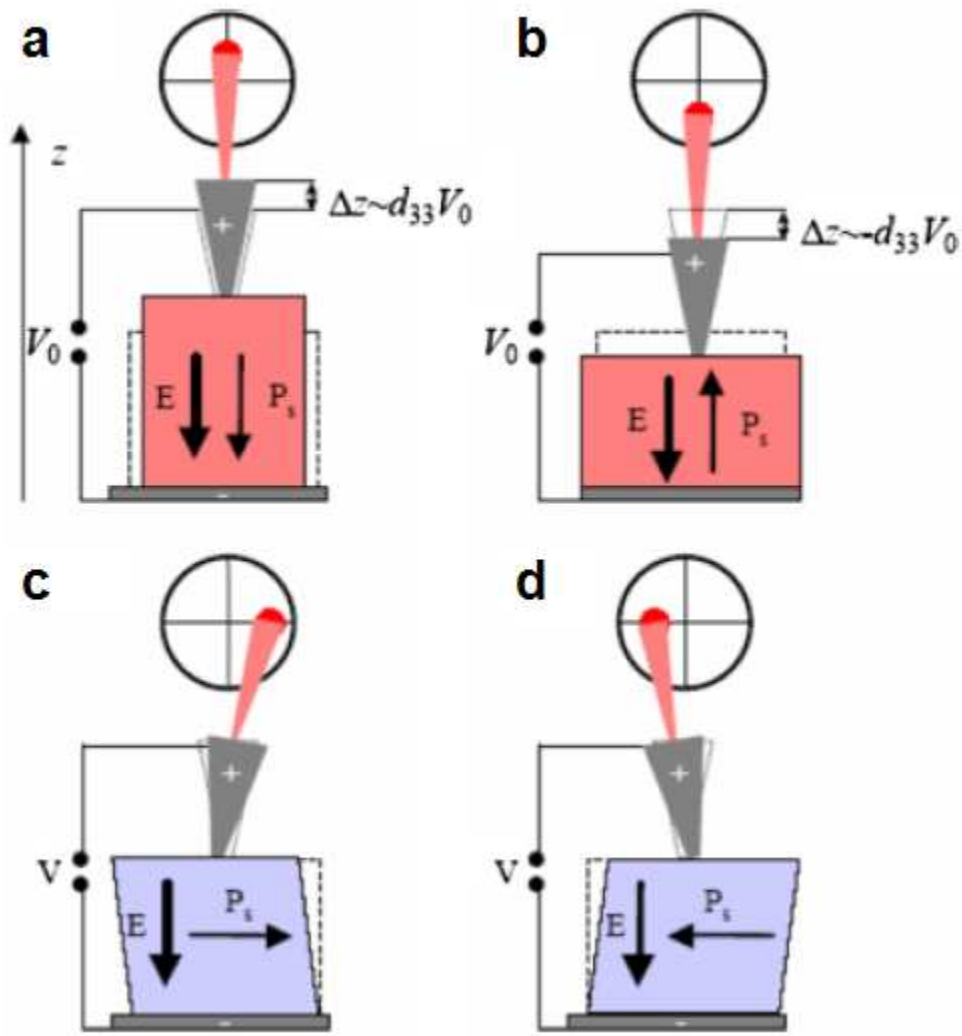

Figure A.4: Piezoelectric effect in a ferroelectric investigated by PFM. **a, b** Electric field aligned parallel or anti-parallel to the spontaneous polarization results in a vertical displacement of the cantilever. **c, d** Electric field applied perpendicular to the polarization results in a shear deformation. This causes a torsional displacement of the cantilever causing lateral deflection of laser beam [125].

As shown in Figure A.4, when an electric field is applied parallel to the polarization, the material expands and the surface oscillations are in phase with the tip voltage (Figure A.4a). For anti-parallel electric field, the material shrinks and the response is 180° out of phase (Figure A.4b). In addition, when the polarization is parallel to the sample surface, the voltage applied to the tip results in an in-plane surface displacement (Figure A.4c, d). It is then translated via friction into the cantilever torsion detected by conventional SPM methods.

References

1. ITRS, *Roadmap 2010 Update Overview* **2010**, 24.
2. K. Kim, *et al*., Proc. *24th Int. Conf. on Microelect*. **2004**, 1, 377.
3. S. Y. Lee, et al., Proc. *Int. Conf. on Circuit Design and Tech*. **2004**, 45.
4. S. Tehrani, *et al*., *J. Nanosci. and Nonotech*. **2007**, 7, 1, 117.
5. J. Slaughter, *Ann. Rev. Mater. Research*. **2009**, 39, 1, 277.
6. M. Miyake, *et al*., *J. Appl. Phys*. **2008**, 064112.
7. J. F. Scott, *et al.*, *Ferroelectrics* **2006**, 336, 1, 237.
8. Y. Fujisaki, *Jpn. J. Appl. Phys*. **2010**, 49, 100001.
9. L. O. Chua, *IEEE Trans. Circuit Theory* **1971**, 18, 507.
10. A. Sawa, *Mater. Today* **2008**, 11, 28.
11. J. J. Yang, *et al*., *Nature Nanotech*. **2008**, 3, 429.
12. R. Waser, *et al*., *Adv. Mater*. **2009**, 21, 2632.
13. S. Q. Liu, *et al.*, *Appl. Phys. Lett.* **2000**, 76, 2749.
14. A. Beck, *et al.*, *Appl. Phys. Lett.* **2000**, 77, 139.
15. Y. Watanabe, *et al.*, *Appl. Phys. Lett.* **2001**, 78, 3738.
16. J. F. Gibbons, *et al.*, *Solid-State Electron.* **1964**, 7, 785.
17. B. J. Choi, *et al.*, *J. Appl. Phys.* **2005**, 98, 033715.
18. A. Chen, *et al.*, *Tech. Dig. IEDM* **2005**, 746.
19. R. Waser, *et al*., *Nature Mater*. **2007**, 6, 833.
20. R. Merkle, *et al*., *Angew. Chem. Int. Ed.* **2008**, 47, 3874.
21. T. Ishihara, *et al*., *Perovskite Oxide for Solid Oxide Fuel Cells, Springer* **2009**, 46.
22. C. -C. Lin, *et al*., *IEEE.* **2006**, 27, 725
23. H. Inoue, *et al*., *Phys. Rev. B.* **2008**, 77, 035105.
24. A. Beck, *et al*., *Appl. Phys. Lett.* **2000**, 77, 139.
25. J. Rodriguez, *et al*., *Appl. Phys. Lett.* **2003**, 83, 4595.
26. P. Levy, *et al*., *Phys. Rev. B.* **2002**, 65, R140401.
27. T. Fujii, *et al*., *Appl. Phys. Lett.* **2005**, 86, 012107.
28. I. Stolichnov, *et al*., *J. Appl. Phys.* **1998**, 84, 3216.
29. M. J. Rozenberg, *et al*., *Phys. Rev. Lett.* **2004**, 92, 178302-1.
30. G.-S. Park, *et al*., *Appl. Phys. Lett.* **2007**, 91, 222103.
31. K. Szot, *et al*., *Nature Mater*. **2006**, 5, 312.
32. V. M. Fridkin, *Ferroelectric semiconductors, Consultants Bureau, New York*, **1980**.
33. J. G. Bednorz, *et al*., *Z. Phys. B* **1986**, 64, 189.
34. P. W. Anderson, *Science* **1987**, 235, 1196.
35. S. Jin, *et al*., *Science* **1994**, 264, 413.
36. V. A. Khomchenko, *et al*., *J. Phys. D: Appl. Phys*. **2008**, 41, 102003.
37. J. Wang, *et al*., *Science* **2003**, 299, 1719.
38. S. V. Kiselev, *et al*., *Sov. Phys. Dokl* **1963**, 7, 742
39. J. R. Teague, *et al*., *Solid State Commun*. **1970**, 8, 1073.
40. J. M. Moreau, *et al*., *J. Phys. Chem. Solids* **1971**, 32, 1315.
41. T. Zhao, *et al*., *Nature Mater*. **2006**, 5, 823.
42. P. Fischer, *et al*., *J. Phys. Solid State Phys.* **1980**, 13**,** 1931.
43. R. F. Klie, *et al*., *J. Electron Microscopy* **2002**, 51, S59.
44. A. I. Becerro, *et al*., *Phys. Chem. Chem. Phys*. **2000**, 2, 3933.

45. J. –C. Grenier, *et al*., *Sturct. Bond*. **1981**, 47, 1.
46. H. Yamamura, *et al., Nippon Kagaku Kaishi* **1972**, 2, 343.
47. V. A. Khomchenko, *et al., J. Magnetism and Magnetic Mater.* **2009**, 321, 1692.
48. F. Zavaliche, *et al., Appl. Phys. Lett.* **2005**, 87, 182912.
49. K. Uchida, *et al., Phys. Rev. B* **2003**, 68, 174107.
50. A. Sawa, *Mater. Today* **2008**, 11, 28.
51. P. W. M. Blom, *et al., Phys. Rev. Lett*. **1994**, 73, 2107.
52. R. Mogilevsky, *et al., Phys. Rev. B* **1994**, 49, 6420
53. V. Vashook, *et al., Ionics* **2001**, 7, 59
54. R. Merkle, *et al., Angew. Chem. Int. Ed*. **2008**, 47, 3874
55. D. B. Strukov, *et al., Appl. Phys. A* **2009**, 94, 515.
56. N. Cabrera, *et al., Rep. Prog. Phys*. **1948**, 12, 163.
57. S. Murugavel, *et al., J. Non-Cryst. Solids* **2005**, 351, 2819.
58. R. Waser, et al., *J. Am. Ceram. Soc*. **1990**, 73, 1645.
59. Z. Cheng, *et al., Phys. Rev. B* **2008**, 77, 092101.
60. S. O. Kasap, *"Principles of electronic Materials and Devices" 3rd Ed,* McGraw-Hill, NY, **2006**, 593.
61. R. Landauer, *et al., Phys. Rev. B* **1972**, 5, 1189.
62. J. C. Slater, *et al., Phys. Rev*. **1950**, 78, 748.
63. I. Bunget, *et al., "Physics of Solid Dielectrics"* Elsevier, **1984**.
64. K. Szot, *et al., Nature Mater*. **2006**, 5, 312.
65. J. P. Vihmalo, *et al., Sold-State Elec*. **2005**, 49, 1714.
66. S. Lai, *IEDM* **2008**, 1.
67. S.Y. Lee, *et al., IEEE Int. Conf. on Integrated Circuit Design and Tech*. **2004**, 45
68. K. Kim, *et al.*, Proc. *24th Int. Conf. on Microelect*. **2004**, 1, 377.
69. A. Sawa, *Materials Today* **2008**, 11, 28.
70. J. J. Yang, *et al., Nature Nanotech*. **2008**, 3, 429.
71. R. waser, *et al., Adv. Mater*. **2009**, 21, 2632.
72. J. C. Scott, *Science* **2004**, 304, 62.
73. M.-J Lee, *et al., IEDM Tech. Dig.* **2007**, 771.
74. C.-H. Yang, *et al., Nature Mater*. **2009**, 8, 485.
75. G X. S. Xu, *et al.*, Phys. Rev. B 2009, 79, 134425.
76. H. Yang, *et al., Appl. Phys. Lett.* **2008**, 92, 102113.
77. S. J. Clark, *et al., Appl. Phys. Lett.* **2007**, 90, 132903.
78. X Chen, *et al., Appl. Phys. A.* **2010**, 100, 987.
79. S. Asanuma, *et al., Phys. Rev. B* **2009**, 80, 235113.
80. G. W. Pabst, *et al., Appl. Phys. Lett.* **2007**, 90, 072902.
81. P. Han, *et al., Appl. Phys. Lett.* **2007**, 91, 182102.
82. D. B. Strukov, *et al., Nature* **2008**, 453, 80.
83. J. Maier, *Angew. Chem. Int. Ed. Engl.* **1993**, 32, 313.
84. D. Day, *et al., Topics in Appl. Phys*. **2003**, 86, 1.
85. J. Carriere, *et al., Progress in Optics* **2000**, 41, 97.
86. M. Chen, *et al., Appl. Phys. Lett.* **1986**, 49, 502.
87. M. Mansuripur, *et al., Proc. IEEE* **1997**, 85, 1780.
88. M. Nansuripur, *"The physical Principles of Magneto-optical Recording"* London, Cambridge Univ. Press, **1995**.

89. L. D'Auria, *et al.*, *Appl. Opt*. **1974**, 13, 808
90. H. J. Coufal, *et al.*, *"Holographic Data Storage"* Springer-Verlag, **2000**.
91. G. W. Burr, et al., *Appl. Opt*. **1999**, 38, 6779.
92. D. A. Parthenopolous, *et al.*, *Science* **1989**, 245, 848.
93. W. Denk, *et al.*, *Science* **1990**, 248, 73.
94. T. R. Ogden, *et al.*, *Mater. Lett*. **1985**, 3, 127.
95. G. M. Guro, *et al.*, *Sov. J. Quant. Electron*. **1974**, 4, 24.
96. H. Coy, *et al.*, *J. Appl. Phys*. **2010**, 108, 113115.
97. G. H. Haertling, *Ferroelectrics* **1987**, 75, 25.
98. E. Mytilineou, *J. Non-Crys. Solids* **2006**, 352, 1991.
99. S. R. Ovshinsky, *Jap. J. Appl. Phys*. **2004**, 43, 4695.
100. X. S. Xu *et al.*, *Phys. Rev. B* **2009**, 79, 134425.
101. C.-H. Yang, *et al*., Nature Mater. **2009**, 8, 485.
102. A. I. Becerro, *et al.*, *Phys. Chem. Chem. Phys*. **2002**, 2, 3933.
103. R. F. Klie, *et al.*, *J. Elec. Microscopy* **2002**, 51, s59.
104. R. Palai, *et al*., *Phys. Rev. B* **2008**, 77, 014110.
105. G. Catalan, *et al.*, *Adv. Mater*. **2009**, 21, 1.
106. P. Hohenberg, *et al.*, *Phys. Rev*. **1964**, 136, B864.
107. W. Kohn, *et al.*, *Phys. Rev*. **1965**, 140, A1133.
108. P. E. Blöchl, *Phys. Rev. B* **1994**, 50, 17953.
109. G. Kresse, *et al.*, *Phys. Rev. B* **1996**, 54, 11169.
110. J. P. Perdew, *et al.*, *Phys. Rev. Lett*. **1996**, **77**, 3865.
111. V. I. Anisimov, *et al.*, *J. Phys.: Condens. Matter* **1997**, 9, 767.
112. C. Ederer, *et al.*, *Phys. Rev. B* **2005**, 71, 224103.
113. S. Yu, *et al.*, *Appl. Phys. Lett*. **2009**, 95, 231906.
114. M. Gajdos, *et al*., *Phys. Rev. B* **2006**, 73, 045112.
115. D. D. Cuong, *et al*., *Phys. Rev. Lett*. **2007**, 98, 115503.
116. H. Tanaka, *et al*., *Phys. Rev. Lett*. **2002**, 88, 027204-1.
117. A. Nitayama, *et al*., *Electron Devices Meeting, IEDM* **1998**, 355.
118. H. Sunami, *IEDM* **1985**, 694.
119. J. F. Scott, *Annu. Rev. Mater. Sci*. **1998**, 28, 79.
120. H. M. Smith, *et al*., *Appl. Opt*. **1965**, 4, 147.
121. D. Dijkkamp, *et al*., *Appl. Phys. Lett*. **1987**, 51, 619.
122. The picture comes from the website of 'National Aeronautics and Space Administration' (http://rt.grc.nasa.gov/main/rlc/pulsed-laser-deposition-laboratory/).
123. H. M. Christen, *et al*., *J. Phys.:Condens. Matter* **2008**, 20, 264005.
124. T. J. Zhu, *et al*., *Appl. Phys. A* **2005**, 81, 701.
125. N. Balke, *et al*., *J. Am. Ceram. Soc*. **2009**, 92, 1629.